Formability and Failure of Automotive Sheet Material AA5754

Formability and Failure of Automotive Sheet Material AA5754

By

Diana Zdravecky, B. Eng.

A Thesis

Submitted to the School of Graduate Studies

In Partial Fulfillment of the Requirements

for the Degree

Masters of Engineering

McMaster University

© Copyright by Diana Zdravecky, 2007

Master of Applied Science (2007)
(Materials Science and Engineering)

McMaster University
Hamilton, Ontario

TITLE: Formability and Failure of Automotive Sheet Material AA5754

AUTHOR: Diana Zdravecky

SUPERVISOR: Professor David S. Wilkinson and Professor Mukesh Jain

NUMBER OF PAGES: xvi, 147

ABSTRACT

The production of aluminum sheet material can follow two distinct processing routes: the conventional semi-continuous process referred to as direct-chill (or DC) casting and, more recently, the continuous casting process (CC). The variation in processing routes can affect the alloy's microstructure, specifically in terms of particle size distribution and the concentration of alloying elements in solid solution, which can alter the materials mechanical properties. Therefore, the formability and fracture behaviour of AA5754 automotive sheet material in the O-temper, produced via two different processing routes, CC and DC casting, has been investigated by the use of the forming limit diagram (FLD).

An in-plane forming test, developed by Marciniak (1973) was used to determine the intrinsic forming limits of the two materials, while full-field strain mapping based on digital image correlation analysis was used to follow the inhomogeneous plastic flow behaviour. As a result, PLC deformation bands were observed and their influence as geometric imperfections to initiate premature failure was shown to be dependent on the strain path. In addition, post-necking and fracture observations were used to understand the influence of microstructural variations and inhomogeneities on the total ductility of AA5754, in terms of the two processing routes.

ACKNOWLEDGEMENT

I wish to express my gratitude to both my supervisors Dr. David Wilkinson and Dr. Mukesh Jain for their expertise, guidance and most importantly patience and understanding throughout the course of this thesis.

I would like to thank all the staff in the Materials Science and Engineering department and the McMaster Manufacturing Research Institute, most importantly Dr. Mike Bruhis and Dr. Yuriy Ososkov for the considerable amount of time and assistance they provided to the research project.

In addition to the technical support I received, I would like to thank all my family and friends for their constant love, help and encouragement throughout the last few years. Most importantly, I would like to thank everyone who has made my stay at McMaster University amazing, especially Florent and all my fellow graduate students in A206.

In conclusion, I recognize that this research would not have been possible without the financial assistance of the Natural Science and Engineering Research Council, General Motors of Canada and McMaster University for their generous support.

TABLE OF CONTENTS

Abstract iii

Acknowledgement iv

Table of Contents v

List of Figures viii

List of Tables xv

1 INTRODUCTION 1

2 LITERATURE REVIEW 3

2.1 Aspects of Formability 3
2.1.1 Overview 3
2.1.2 Forming Limit Diagram 4
2.1.3 Limits of Formability 7
2.1.4 Experimental Techniques to Develop FLDs 12
2.1.5 Determination of Forming Limits from Experimental Techniques 16

2.2 Factors that Influence Formability and FLDs 17
2.2.1 Material Properties 17
2.2.2 Mechanical Testing Techniques 21

2.3 Aluminum Alloy 5754 25
2.3.1 Processing Methods 26
2.3.2 Mechanical Properties 27
2.3.3 Microstructure 30

2.4 Shear Localization and Failure 32

2.5 Summary 36

3 EXPERIMENTAL METHODS 37

3.1 Materials 37

3.2 Standard Tensile Specimens 37

3.3 Formability Testing 38
3.3.1 Marciniak Test Sample Geometry 40
3.3.2 Marciniak Test Driver Geometry 41

3.4 Argus Strain Measurement System 42
3.4.1 Sample Preparation 43
3.4.2 Test Conditions 44
3.4.3 Data Analysis 45

3.5 ARAMIS Strain Measurement System 46
3.5.1 Sample Preparation 46
3.5.2 Test Conditions 47
3.5.3 Data Analysis 49

3.6 Optimization of Test Conditions 53
3.6.1 Determination of Driver material 53
3.6.2 Determination of Punch Profile 54
3.6.3 Determination of the Driver Geometry 56

3.7 Forming Limits Evaluation 58

3.8 Metallography 63
3.8.1 Sample Preparation 63
3.8.2 Heat Treatment and Etching for Shear Bands 65

3.9 Fracture Strain Measurements 65

4 EXPERIMENTAL RESULTS 68

4.1 Material Characteristics and Mechanical Properties 68
4.1.1 Optical Metallography 68
4.1.2 Uniaxial Tensile Test of Standard Sheet Samples 70
4.1.3 Fracture Behaviour of Uniaxial Tensile Test Samples 71

4.2 Evaluation of Forming Limits 73
4.2.1 Load versus Displacement Data 73
4.2.2 Forming Limit Diagram 75

4.3 Examination of Material Deformation Behaviour 76
4.3.1 Specimen Geometries for Left-Hand Side of FLD 77
4.3.2 Specimen Geometries for Right-Hand Side of FLD 84

4.4 Microstructural Analysis of Fracture Behaviour 88
4.4.1 Specimen Geometries for Left-Hand Side of FLD 89
4.4.2 Specimen Geometries for Right-Hand Side of FLD 94

5 DISCUSSION 104

5.1 Influence of Material Characteristics on the Uniaxial Tensile Mechanical Properties of CC5754 and DC5754 104
5.1.1 Grain Size 105
5.1.2 Composition and Work-Hardening Behaviour 106

5.2 Analysis of Forming Limits 112
5.2.1 Overview 112
5.2.2 Influence of Material Properties on the FLC 113

5.3 Influence of the Deformation Behaviour on Strain Localization 116
5.3.1 Spatial Features of Deformation Bands 116
5.3.2 Failure Mechanism 120

5.4 Post-Necking and Fracture Behaviour 123

5.5 Evaluation of Test Technique 125
5.5.1 Digital Image Correlation Technique 125
5.5.2 Design and Optimization of Specimen and Driver Geometries 126

6 CONCLUSIONS 131

REFERENCES 133

APPENDIX 139

A – Forming Limits Evaluation **139**

B – Surface Marking Observations **146**

LIST OF FIGURES

Figure 2.1	Representation of forming limit diagram showing idealized modes of deformation given by the strain path, forming limit and fracture limit.	6
Figure 2.2	(a) Development of a diffuse neck and (b) a localized neck in sheet metal forming for drawing conditions (LHS of FLD). Adapted from Hosford and Caddell (1993).	8
Figure 2.3	Schematic of a groove in a sheet under biaxial tension (Hosford and Caddell, 1993).	10
Figure 2.4	Gradual change in strain path within the groove (B) with increasing strain (Marciniak, Duncan and Hu, 2002).	11
Figure 2.5	Hemispherical punch set-up for out-of-plane testing proposed by Hecker for obtaining FLDs (Raghavan, 1995).	12
Figure 2.6	Deformed out-of-plane test specimen geometries producing eight strain paths.	13
Figure 2.7	In-plane test setup proposed by Tadros and Mellor (1977) for obtaining FLDs showing punch geometry.	14
Figure 2.8	Strain paths of driver and test specimen under stretching conditions for in-plane testing.	15
Figure 2.9	Influence of strain-hardening and strain rate sensitive on the forming limit curve.	18
Figure 2.10	The level of FLDs from out-of-plane test for different materials based on the work hardening index and strain rate sensitivity (Ghosh, 1977).	19
Figure 2.11	Maximum attainable strain in the uniform region of a perfect and imperfect tensile specimen (Hosford and Caddell, 1993).	20
Figure 2.12	(a) Punch profile during stretching for out-of-plane deformation and (b) the resulting distribution of strain along the punch profile under friction and frictionless conditions (Marciniak, Duncan and Hu, 2002).	22

Figure 2.13 Influence of punch curvature on stretching limits (hot rolled, AKDQ steel, 1.83 mm thick). Adapted from Charpentier (1975). 23

Figure 2.14 Comparison of in-plane and out-of-plane FLDs for aluminum 3105 (Moshksar, 2003). 24

Figure 2.15 Flow diagram for the production of coiled aluminum sheet by DC and CC casting routes with numbers indicating typical metal thickness in mm (Azari, 2000). 27

Figure 2.16 Correlation between tensile yield strength, elongation and magnesium content for commercial 5000 series aluminum alloys (Hamilton and Ghosh, 1988). 28

Figure 2.17 Microstructure of AA 5754 (0.21% Fe) showing particle distribution and banding. Pictures taken by Jidong Kang (2004). 31

Figure 2.18 Volume fraction of stringer and total particles of CC and DC5754 sheet material with similar chemical composition (Kang et al., 2006). 32

Figure 2.19 Through-thickness sections of AA5754 after punch stretching showing variations is fracture profile 33

Figure 2.20 Localized shear fracture after strain localization in the form of a macroscopic shear band. 34

Figure 2.21 Variation of effective plastic strain with iron content (Spencer, 2002). 35

Figure 3.1 ASTM Standard subsize specimen dimensions for tensile testing. 38

Figure 3.2 Marciniak test method setup for formability testing showing punch and sample setup (specimen positioned above driver for digital image analysis) (Bruhis, 2005). 39

Figure 3.3 Marciniak punch designs produced by Mike Bruhis, 2006 (dimensions in inches). 39

Figure 3.4 Specimen geometries for left-hand side of FLD showing the clamping ring and rolling-direction of the material (dimensions in inches). Drawings produced by Situ Quan and Mike Bruhis, 2004. 41

Figure 3.5 Specimen geometries for right-hand side of FLD (Quan and Bruhis, 2004). 41

Figure 3.6 Driver geometries for right-hand side specimens. Adapted from Quan and Bruhis, 2004. 42

Figure 3.7 Electrochemically etched dot patterns for ARGUS Analysis. 44

Figure 3.8 Example of ARGUS system set-up and specimen with calibration markers for analysis. 44

Figure 3.9 Example of ARGUS results showing defined section and the true major and minor strain plot across the section. 45

Figure 3.10 True major and minor strain plot from ARGUS system on undeformed specimen. 46

Figure 3.11 Regular fine mist ink pattern applied to AA5754 specimens for ARAMIS testing. 47

Figure 3.12 ARAMIS system set-up with Marciniak punch showing camera separation distance (d) and angle (α). 48

Figure 3.13 Calibration object for ARAMIS system showing the given arrangement of white points. 49

Figure 3.14 Example of ARAMIS system results used for forming limits evaluation. 50

Figure 3.15 Example of ARAMIS system results used for deformation band strain evaluation. 51

Figure 3.16 Plot of local true strain as a function of global true strain for 1 inch width geometry. The point of maximum strain carried in the deformation band is shown through graphical extrapolation. 52

Figure 3.17 True major and minor strain plot of driver material selection for DC5754 7 inch geometry sample showing sample and driver strain paths. 54

Figure 3.18	(a) Failure along punch profile and (b) strain distribution across 7 inch width specimen.	55
Figure 3.19	Failure initiated by fracture in driver material prior to fracture in the test specimen.	55
Figure 3.20	Successfully test specimen fractured along the stretching region with no failure in the deformed driver blank.	56
Figure 3.21	Forming limit results for 4 inch, 5 inch and 7inch width specimens for various washer geometries – DC material.	57
Figure 3.22	Forming limit results for 4 inch, 5 inch and 7inch width specimens for various washer geometries – CC material.	57
Figure 3.23	4 inch width specimen strain map showing localization and prominent shear band.	60
Figure 3.24	True major and minor strain plot showing 4^{th} order polynomial interpolation.	60
Figure 3.25	True major strain profile for specimen in Figure 3.23 and 3.24 showing the various fitted polynomial curves for forming limit evaluation.	61
Figure 3.26	True major and minor strain plot showing 4^{th} order polynomial interpolation.	62
Figure 3.27	Various specimen width geometries showing sectioning for fracture strain measurements.	64
Figure 3.28	Revealed through thickness showing shear bands from heat treatment and etching technique on necked specimen using NDI contrast.	65
Figure 3.29	Modified image of aligned fractured halves for minimum cross-sectional thickness measurements.	66
Figure 4.1	Microstructure and grain sizes for (a) CC5754 and (b) DC5754.	69
Figure 4.2	True stress-strain curves for CC and DC5754 – Rolling direction.	70
Figure 4.3	Through-thickness sections of CC tensile sample showing shear localization failure and shear band formation.	72

Figure 4.4	Through-thickness sections of DC tensile sample showing shear localization failure and shear band formation.	72
Figure 4.5	Punch load versus punch displacement data for CC5754.	74
Figure 4.6	Punch load versus punch displacement data for DC5754.	74
Figure 4.7	In-plane forming limit curve for CC5754 and DC5754 material.	76
Figure 4.8	Strain maps for 0.5 inch (θ = 59-62°) and 2 inch (θ = 65-67°) specimens showing type B PLC band deformation behaviour and band inclination angles.	78
Figure 4.9	Strain map showing symmetrical PLC bands propagating along specimen gauge length.	79
Figure 4.10	CC5754-2 inch width test specimen showing characteristic surface marking associated with PLC deformation bands.	80
Figure 4.11	Plot of local true strain as function of global true strain for 0.5 inch width geometry.	81
Figure 4.12	Plot of local true strain as function of global true strain for 1 inch width geometry.	82
Figure 4.13	Plot of local true strain as function of global true strain for 2 inch width geometry.	82
Figure 4.14	Strain maps for tested specimens showing deformation behaviour.	84
Figure 4.15	4 inch width test specimens showing characteristic surface marking associated with PLC deformation bands.	85
Figure 4.16	Plot of local true strain as function of global true strain for 4 inch width geometry.	86
Figure 4.17	Plot of local true strain as function of global true strain for 5 inch width geometry.	87
Figure 4.18	Plot of local true strain as function of global true strain for 7 inch width geometry.	87

Figure 4.19 Through-thickness sections of (a) CC5754 and (b) DC5754 showing strain localization (left) and the fracture profile (right) for 0.5 inch width geometry specimens. 90

Figure 4.20 Through-thickness sections of (a) CC5754 and (b) DC5754 showing strain localization (left) and the fracture profile (right) for 1 inch width geometry specimens. 91

Figure 4.21 Through-thickness sections of (a) CC5754 and (b) DC5754 showing strain localization (left) and the fracture profile (right) for 2 inch width geometry specimens. 92

Figure 4.22 Sectioning of specimens for fracture and necking strain measurements. 94

Figure 4.23 Through-thickness sections of CC5754 showing shear banding and propagation of damage leading to fracture for 4 inch width geometry. 95

Figure 4.24 Through-thickness sections of DC5754 showing shear banding and propagation of damage leading to fracture for 4 inch width geometry. 96

Figure 4.25 Through-thickness sections of CC5754 showing shear banding and propagation of damage leading to fracture for 5 inch width geometry. 97

Figure 4.26 Through-thickness sections of DC5754 showing shear banding and propagation of damage leading to fracture for 5 inch width geometry. 98

Figure 4.27 Through-thickness sections of CC5754 showing shear banding and propagation of damage leading to fracture for 7 inch width geometry. 99

Figure 4.28 Through-thickness sections of DC5754 showing shear banding and propagation of damage leading to fracture for 7 inch width geometry. 100

Figure 4.29 CC5754 specimen strain paths showing necking and fracture strains. 103

Figure 4.30 DC5754 specimen strain paths showing necking and fracture strains. 103

Figure 5.1 Variation of yield stress with grain size in Al alloys O-temper. Material was DC cast to 1 mm gauge of thickness (Burger et al., 1995). 110

Figure 5.2 Plot of work hardening rate $d\sigma/d\varepsilon$ as a function of strain following the Voce Eqn. for uniaxial test specimens of CC5754 and DC5754. 111

Figure 5.3 Schematic view of failure region of a uniaxial sheet metal specimen (Morris et al., 1987). 112

Figure 5.4 Conditions for localized necking on the LHS of the FLD according to Hill's theory with a material obeying the Holloman Eqn. 113

Figure 5.5 Instantaneous strain hardening exponent (n′) variation with strain for Al-Mg6.8 alloy sheet (Romhanji et al., 1998). Data taken at various angles to the rolling direction. 114

Figure 5.6 Gradual change in strain path within the imperfection with increasing strain for 0.5 inch, 1 inch and 2 inch geometries. 120

Figure 5.7 Strain map sequences for 1 inch and 2 inch width specimens showing symmetrical band formation and initiation of strain localization. 122

Figure 5.8 Strain localization in CC5754 specimen showing characteristic surface marking associated with the PLC effect. 122

Figure 5.9 Strain map sequence for 4 inch width specimen showing deformation bands and failure. 124

Figure 5.10 Schematic of a localized neck showing the location of shear zones which initiate shear banding (Timothy, 1989). 125

Figure 5.11 ARAMIS system set-up showing variation in measuring volume needed to accommodate deformation process. 126

Figure 5.12 Comparison of specimen geometries for left-hand side of FLD. Drawings produced by Situ Quan and Mike Bruhis, 2004. 127

Figure 5.13 True major and minor strain plot showing 4^{th} order polynomial interpolation. 128

LIST OF TABLES

Table 2.1	Summary of the main characteristics which influence formability testing based on deformation technique	25
Table 3.1	Chemical Composition of Alloy (wt %)	37
Table 3.2	Parameter settings for electrochemical etching	43
Table 3.3	Determined hole diameters for each specimen geometries	58
Table 3.4	Effect of polynomial fitting order on forming limits evaluation using the Bragard criterion	62
Table 3.5	Effect of facet size of forming limits evaluation using the Bragard criterion	63
Table 3.6	Grinding and Polishing Sequence for AA5754	64
Table 4.1	Tensile properties for CC and DC 5754	71
Table 4.2	Maximum punch load and punch displacement data for CC5754 specimens	75
Table 4.3	Inclination angle of the deformation bands with respect to the tensile axis	77
Table 4.4	True global strain at the alteration of inclination angle of PLC bands	79
Table 4.5	Maximum strain carried in PLC bands according to the local and global true strain plots	83
Table 4.6	Global true strain at the onset of PLC band development in CC5754 and DC5754	83
Table 4.7	Maximum strain carried in the deformation bands according to the local and global true strain plots	86
Table 4.8	Global true strain at the onset of PLC band development in CC5754 and DC5754	88

Table 4.9 Summary of failure mechanism and strain values determined from optical micrographs for LHS samples 93

Table 4.10 Summary of failure mechanism and strain values determined from optical micrographs for RHS samples 102

Table 5.1 Comparison of the predicted inclination angles of the deformation bands with measured values for specimen geometries on the LHS of the FLD 117

To produce the product, the CC processing route is favoured over the conventional DC route for economic reasons. It is well known in industry though, that CC products usually have an inferior formability and larger mechanical anisotropy than DC products (Cheng, 2001). This is largely attributed to the variations in microstructural characteristics that arise due to the difference in solidification rate between CC casting and DC casting.

Therefore, the main objective of this study was to evaluate and compare the formability and fracture behaviour of CC and DC cast AA5754 automotive sheet material by the use of the forming limit diagram. The forming and fracture limits were experimentally determined using the in-plane test methodology developed by Marciniak (1973) to identify the forming limit and fracture strains of the sheet materials under a variety of strain paths. The deformation and failure behaviour of the materials was then examined as a function of strain path. This was accomplished by digital image correlation techniques which provide in-situ strain measurements and deformation analysis throughout the testing process followed by metallography and optical microscopy techniques to determine the failure mechanism under different in-plane stretching conditions. From these results, insight has been gained into understanding the effect that microstructural differences has on the formability and failure behaviour of CC and DC cast AA5754.

Chapter 2
Literature Review

This chapter will review the relevant literature related to sheet metal formability in this study. It will first provide a detailed background on the concept of formability and the use of the forming limit diagram. It will then examine the various aspects that influence formability such as material properties and the testing techniques. The following section will pertain to the materials used in this study, CC and DC cast AA5754. Finally, factors which distinguish the two materials, specifically in terms of the materials processing paths and their relation to the various aspects of formability will be reviewed.

2.1 Aspects of Formability

2.1.1 Overview

Sheet formability can be defined as the relative ease with which a sheet metal can be shaped through plastic deformation. It includes a wide range of shaping processes such as deep drawing, stretch forming and bending, which are used in the fabrication of manufactured goods such as cans, automotive panels and domestic appliance casings. Due to the extensive use of sheet forming in various applications, testing techniques have been developed to assess and predict the formability of sheet materials. The main objective of formability testing is to develop a detailed description of the behaviour of the

material being formed by the various shaping processes and to identify the limitations of materials and processes.

2.1.2 Forming Limit Diagram

Failure in sheet metal forming processes is usually characterized by the development of a sharp localized neck in the thickness direction, visible on the surface of the sheet metal. One formability representation that has proven to be a valuable tool in sheet metal forming is the forming limit diagram (or FLD). It is used to represent the maximum amount of plastic deformation a material can sustain prior to the onset of necking for a wide range of loading conditions typical of forming operations.

The term forming limit diagram (FLD) was first introduced by Keeler and Backofen (1963) who investigated the failure of biaxial stretched sheets of steel, copper, brass and aluminum over solid punches. They found that localized necking could be described by plotting a map of the principal strains on the surface of the sheet metal that were measured adjacent to the failure site through means of electrochemically etched grids. The plot represented the coordinates of the limiting strains that caused local necking in biaxial stretching. Goodwin (1968) further extended the experimental techniques set forth by Keeler to include limiting strains less than zero (so called minor-strain region). The combined result was the development of the forming limit diagram or Keeler-Goodwin diagram. FLDs are used to represent the relationship between the major and minor principal strain space on the surface of the sheet material, and most importantly, indicate the limiting strains that a sheet metal can sustain before failure in the forming operation.

An FLD has two sides, the left-hand side (LHS) that represents drawing conditions and the right-hand side (RHS) that represents stretching conditions (Figure 2.1). The relationship between major and minor strains is represented by the strain path. Different strain paths are achieved by varying the ratio (Eqn. 2.1) between the major (ε_1) and minor principal strains (ε_2) which are assumed to be linearly proportional. This linear proportional strain path is often expressed as a strain ratio in the following form:

$$\beta = \frac{\varepsilon_2}{\varepsilon_1} \tag{2.1}$$

where ε_2 (minor) and ε_1 (major) are the two principal strain components on the surface of the sheet.

The LHS of the FLD consists of negative strain ratios, which are represented by positive major strains (ε_1) and negative minor strains (ε_2). The strain paths that can be achieved on the LHS of the FLD range from simple uniaxial tension ($\varepsilon_2 = -\frac{1}{2}\varepsilon_1$ or $\beta = -\frac{1}{2}$) to plane strain ($\varepsilon_2 = 0$ or $\beta = 0$) conditions. The RHS of the FLD is defined by positive major (ε_1) and minor (ε_2) strains, covering strain paths from plane strain to balanced biaxial tension ($\varepsilon_2 = \varepsilon_1$ or $\beta = 1$) conditions. An example of a FLD can be seen in Figure 2.1. Under proportional loading, various strain paths are shown in regards to the major and minor strain conditions (stretching versus drawing). For each strain path, a limit strain (ε_1 and ε_2 value) is reached that corresponds to the onset of necking. A locus of limit strains from a range of strain paths results in a "V" shaped and is referred

to as the forming limit curve or FLC. A strain state in a part below the FLC is considered safe from a forming perspective.

The fracture limit, represented on the diagram, is the strain at which the material finally separates. The strain path also has a pronounced effect on the fracture limit of the material, the line of decreasing slope in Figure 2.1. Fracture limit of most ductile materials continuously decreases as the strain path is changed from simple tension to biaxial tension. The fracture limit consists of the necking strain from FLC and the strain resulting from the growth of a neck into fracture. The neck growth typically occurs under a plane strain state (vertical strain path, as shown in Figure 2.1). Therefore, the amount of plastic deformation that is attainable after localized necking (i.e, past FLC) changes with the strain path.

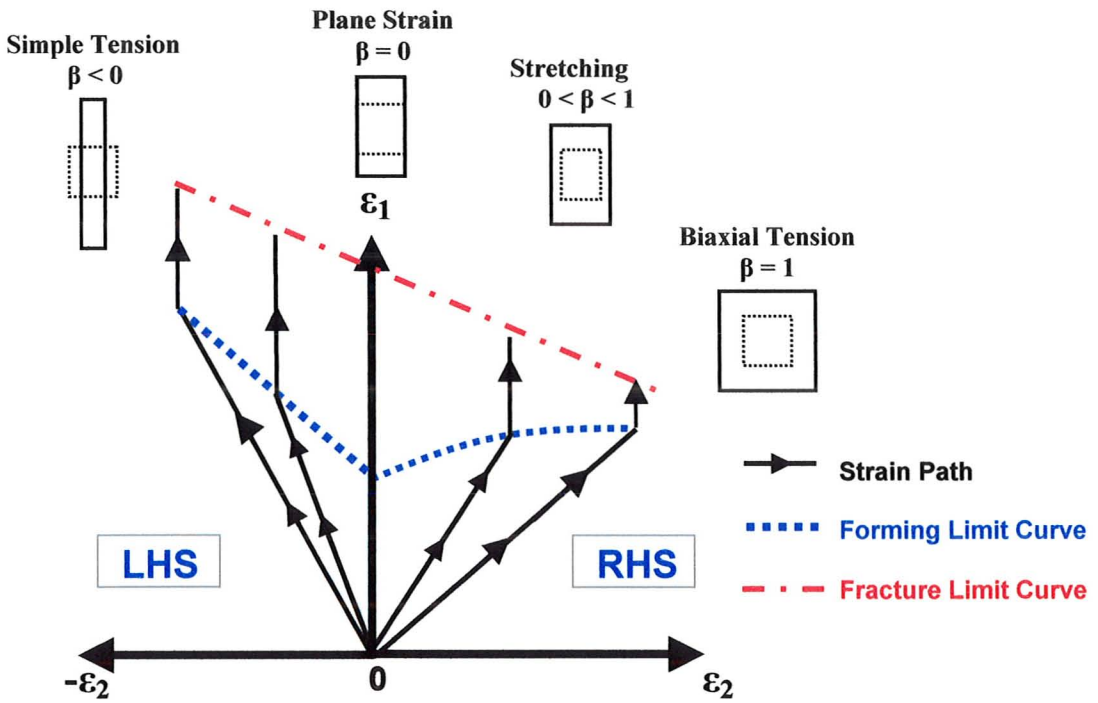

Figure 2.1: Representation of forming limit diagram showing idealized modes of deformation given by the strain path, forming limit and fracture limit.

A complex automotive part during stamping will experience strain paths on both side of the FLD. Therefore, a significant amount of information about materials behaviour under a variety of stress and strain conditions can be characterized by using an FLD. FLDs are especially useful when problems arise during die tryout for a new automotive part or for an existing part that is produced with a new sheet material.

2.1.3 Limits of Formability

The amount of useful deformation in sheet metal forming operations is usually limited by the onset of localization rather than fracture for ductile materials. Several theoretical analyses have been carried out to explain the shape of the forming limit curve and to predict the limit strains. Under strain conditions where the minor strain (ε_2) is negative and up to plane strain conditions, the process of strain localization can be described by the criterion set forth by Hill (1952), which states that localized necking can only occur along a direction of zero extension. Considering a specimen following a strain path in uniaxial tension, the onset of plastic instability is initiated by a form of strain localization corresponding to the maximum in the load-extension curve. Using the assumption that the strain-hardening behaviour is expressed by the Hollomon equation, instability occurs when the strain is equal to the strain hardening index, n (derived from Considère Criterion (1885)). This is accompanied by a reduction in the width and thickness direction of the sample referred to as a diffuse neck (Figure 2.2(a)).

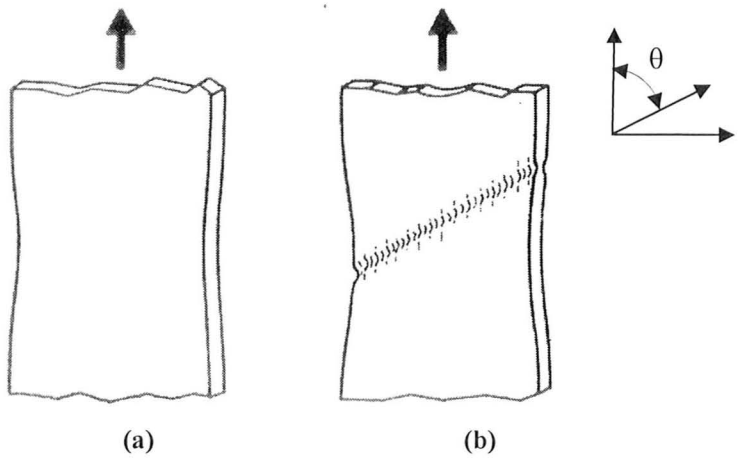

Figure 2.2: (a) Development of a diffuse neck and (b) a localized neck in sheet metal forming for drawing conditions (LHS of FLD). Adapted from Hosford and Caddell (1993).

After diffuse necking, the rate of specimen thinning is greater than the rate of strain hardening and deformation is unstable. Instability in the specimen in the form of an imperfection, for example machining defects or microstructural inhomogeneities, results in regions where the stress is higher than elsewhere in the material. This causes deformation to become more localized, leading to the formation of a macroscopic localized neck (Figure 2.2(b)). When this occurs, the rest of the material unloads elastically and plastic deformation continues in the localized neck region only under conditions of plane strain tension until fracture occurs. The width of the localized neck is on the order of the sheet thickness and is oriented at a specific angle to the loading direction as described in Eqn. 2.2 (Hill, 1952).

$$\tan\theta = \frac{1}{\sqrt{-\beta}} \tag{2.2}$$

Eqn. 2.2 is valid for $\beta < 0$ (left side of FLD) since θ has no real value for $\beta > 0$.

The critical strain at which localized necking occurs is described by the following equation.

$$\varepsilon_1^* = \frac{n}{1+\beta} \tag{2.3}$$

The above expressions are based on the assumption of isotropic behaviour of the sheet material and show a dependency on the strain ratio (β), as given by the strain path. If the sheet material displays anisotropic behaviour, the orientation of the localized neck will change according to Eqn. 2.4, where R is defined as the ratio of width strain to thickness strain.

$$\tan\theta = \sqrt{(R+1)/R} \tag{2.4}$$

The above equations show reasonable agreement with experimental data. Any differences found are attributed to additional strain gradients which are present as a result of bending and friction conditions between the punch and sheet material during the forming process.

When a sheet is deformed under stretching conditions so that both principal strains are positive (ε_1 and $\varepsilon_2 > 0$), there exists no line of zero extension in the sheet plane. According to Eqn. 2.2, a plane of zero extension exists only when the strain ratio is negative. This means the description of localized necking given by Hill cannot be used to predict the onset of failure on the RHS of the FLD. In practice, for many formable materials fracture is preceded by local necking during biaxial sheet deformation (Keeler, 1968). To predict the limiting strains under stretching conditions, Marciniak and Kuczynski (1967) introduced the first and most widely accepted theoretical approach

based on the imperfection analysis. The theory postulates that local necking originates from the pre-existence of an initial weakness or inhomogeneity present in the sheet, lying parallel to the ε_2 direction which is a source of subsequent strain concentration. The inhomogeneity was initially considered to be in the form of a groove resulting in a thickness variation in the sheet. This is shown in Figure 2.3 where t_b represents the thickness in the groove, the weak region where the neck originates, and t_a the thickness in the uniform region.

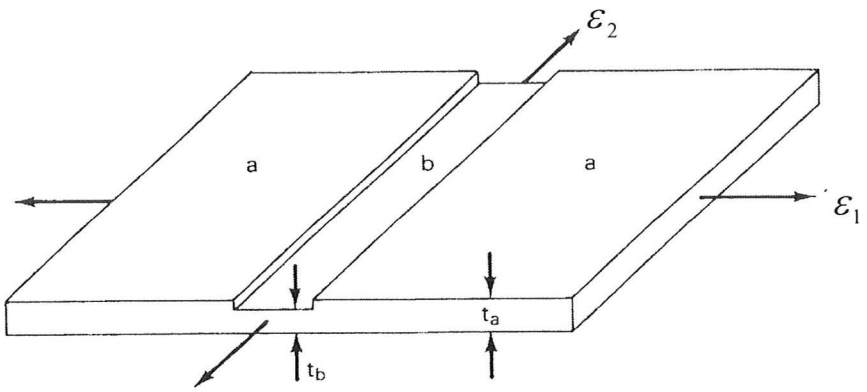

Figure 2.3: Schematic of a groove in a sheet under biaxial tension (Hosford and Caddell, 1993).

The M-K analysis predicts the effects of the applied strain-state on the forming limit strains as a function of the effective severity of the material imperfection as described by an inhomogeneity factor, f_0 (Eqn. 2.5). In a perfect material, f_0 = 1. Materials with larger imperfections (smaller t_b) will have lower f_0 values. A lower f_0 value results in lower forming limit strains from the M-K analysis.

$$f_0 = \frac{t_b}{t_a} \tag{2.5}$$

Considering a sheet specimen deforming under stretching conditions, the material in the initial grooved region does not deform in the same manner as the material outside of it due to geometrical constraints. This is shown graphically in Figure 2.4 on a major and minor strain plot. The strain in the grooved region B will drift and increase at a higher rate with respect to the material in region A which continues along a proportional strain path. Eventually, the grooved region will reach a state of plane strain ($\varepsilon_{2A}^{*} = \varepsilon_{2B}^{*}$). When this occurs, the strain parallel to the groove and in region A will cease while the grooved region will continue straining under plane strain state until failure. This method is often used to explain failure on the RHS of the FLD but it has shown to be inconsistent with experimental data. This is due to the lack of clarity of the nature of the inhomogeneities in the sheet material, which are not always in the form of a thickness variation and in some cases, more than one inhomogeneity has been identified.

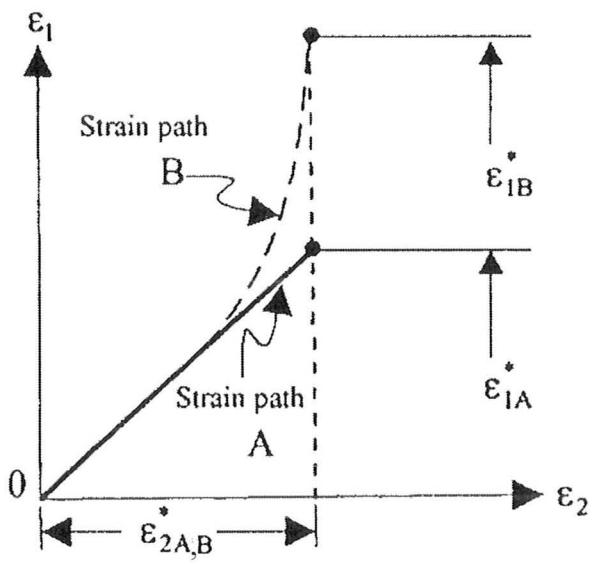

Figure 2.4: Gradual change in strain path within the groove (B) with increasing strain (Marciniak, Duncan and Hu, 2002).

2.1.4 Experimental Techniques to Determine FLDs

The assessment of a material's ability to meet formability requirements can be facilitated by a variety of mechanical tests which are used to simulate some aspect of a forming operation (Rysk, 1986). Two experimental techniques have been adapted for obtaining data to be plotted on an FLD which are capable of evaluating a variety of strain paths ranging from simple tension to balanced biaxial tension, while utilizing one piece of test equipment. The most commonly used technique in industry to assess sheet metal formability is the out-of-plane deformation technique developed by Hecker (1975). The basic technique involves stretching sheet specimens, clamped at the edge between two dies, over a rigid hemispherical punch until failure. The experimental test setup can be seen in Figure 2.5 where the punch is being moved downwards to carry out the dome stretching process.

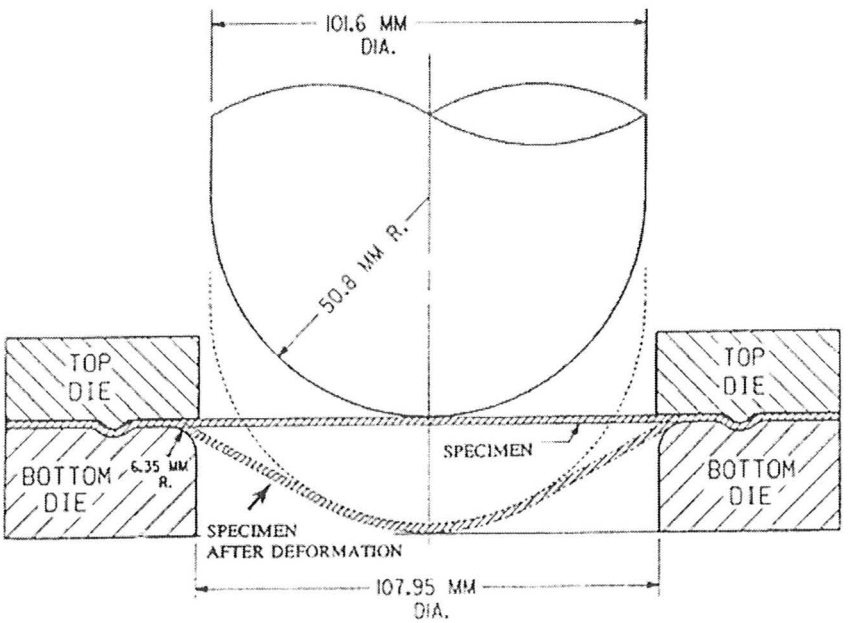

Figure 2.5: Hemispherical punch set-up for out-of-plane testing proposed by Hecker for obtaining FLDs (Raghavan, 1995).

The variation in strain path is controlled by the specimen's geometrical width. As the specimen's width changes, the lateral constraint (ε_2) which controls the amount of material allowed to be drawn into the die cavity in the width direction also changes (Raghavan, 1994). The sample geometries for the LHS of the FLD (negative strain ratios) can be seen in Figure 2.6(a). Specimens with larger widths shift the strain path from uniaxial tension towards plane strain conditions. To generate failures under stretching conditions, larger width specimens are used with the addition of lubrication between the sheet and punch (Figure 2.6(b)). The specimens take on the curvature of the punch after deformation and failure occurs at specific locations on the specimen which are dictated by the tooling geometry, the strain path and friction conditions.

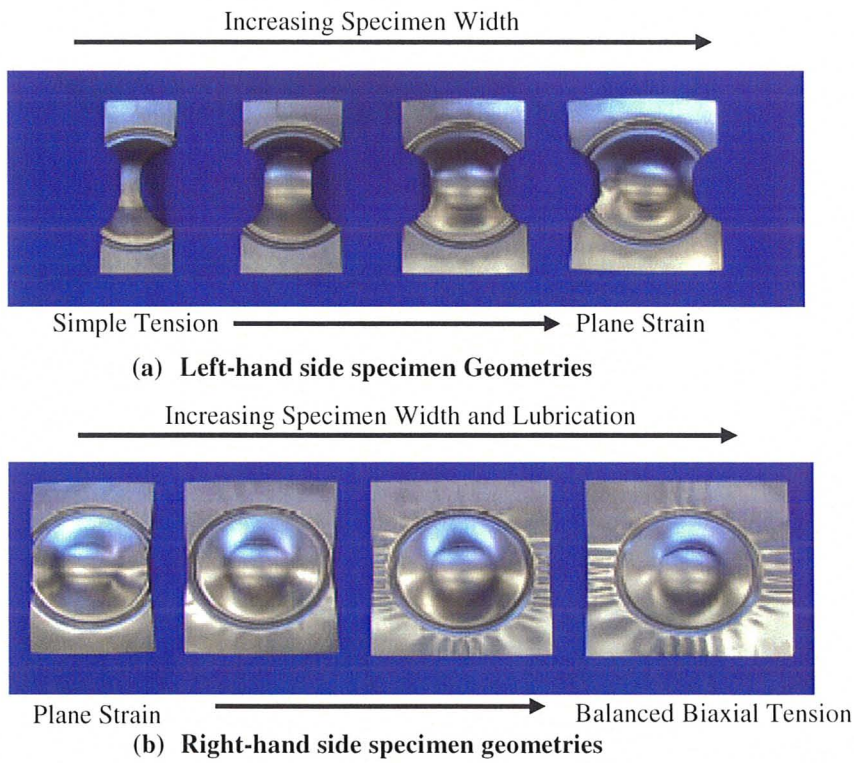

Figure 2.6: Deformed out-of-plane test specimen geometries producing eight strain paths.

The second experimental technique, first introduced by Marciniak and Kuczynski (1973), involves the in-plane deformation of sheet specimens by use of a flat punch (Figure 2.7). The test utilizes a pair of sheet materials, a test blank and a so-called driver blank made of a more formable material and with a hole at its centre, during the stretching test. The stretching is carried out by a flat-headed circular punch. This type of formability testing was first designed to simulate strain paths under stretching conditions (RHS of the FLD) but was later extended to include the LHS of the FLD.

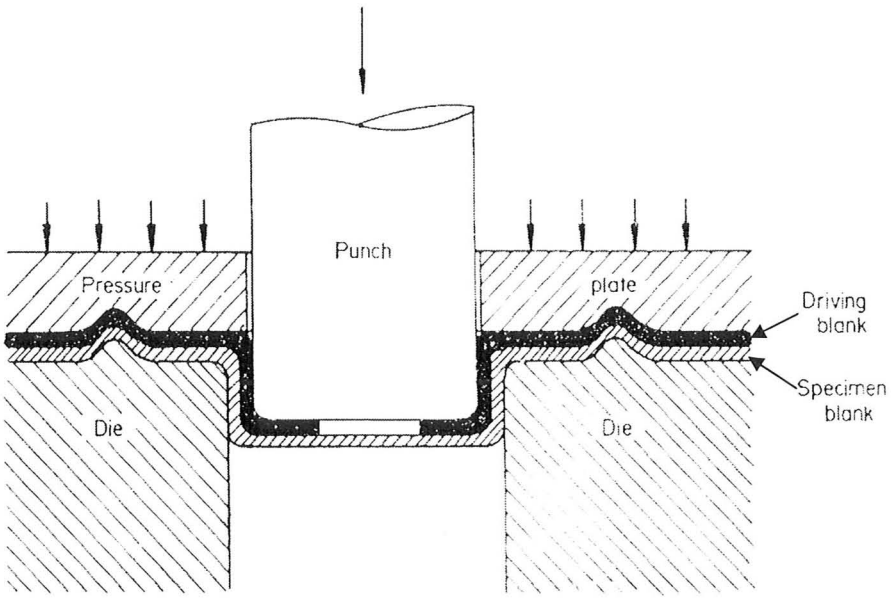

Figure 2.7: In-plane test setup proposed by Tadros and Mellor (1977) for obtaining FLDs showing punch geometry.

If no driver blank was used, the specimen would fail along the rounded edge of the punch profile due to high frictional forces which prevent the material from flowing over the punch radius. To reduce the frictional forces around the punch profile and facilitate stretching in the flat–bottom section of the punch, a driver blank is used between

the punch and test specimen. The driver blank, which easily expands due to the addition of the central hole, can flow over the punch radius with a reduced applied force. As the punch moves further and deforms the driver blank, the specimen is stretched by the radial frictional forces that occur in the contact region between the driving blank and the specimen at the punch profile (Tadros, 1977). Therefore, the deformation of the specimen material is carried out by the driver blank where the largest strains are found in the central area of the specimen which remains flat and free from frictional forces.

The basic technique involves the deformation of the sheet specimen and the driver along two distinctive strain paths which can be seen in Figure 2.8. The sample specimen follows a strain path to the right of the FLD, under stretching conditions, while the driver blank follows a strain path to the left due to the stress state introduced by the central hole.

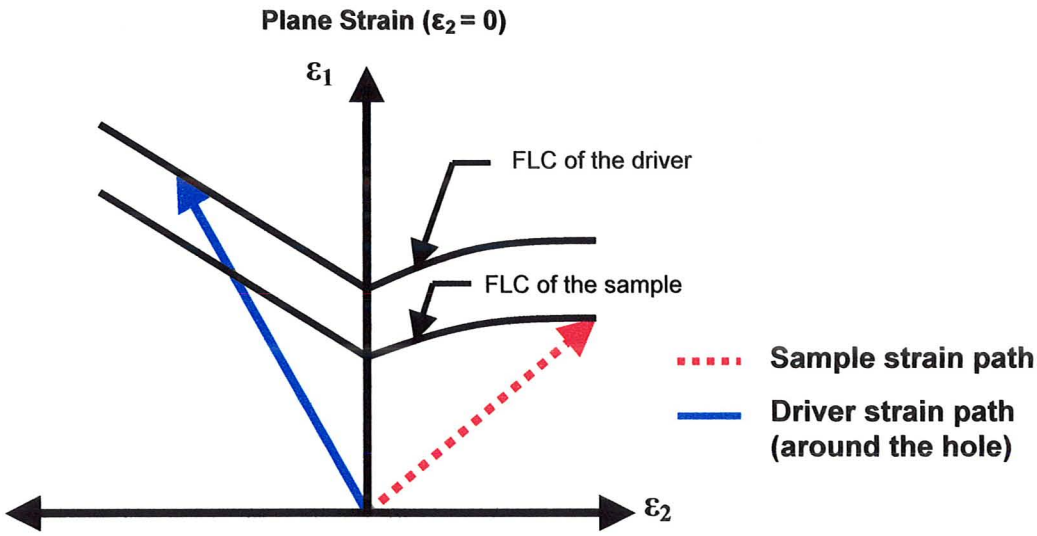

Figure 2.8: Strain paths of driver and test specimen under stretching conditions for in-plane testing.

The in-plane test method uses similar samples geometries as the out-of-plane technique, but no lubrication is used and failure can be achieved in a series of strain paths ranging from simple tension through plane strain to balanced biaxial tension. The success of the test though, relies heavily on the proper selection of the driver blank material and central hole diameters which must be determined experimentally by trial-and-error. For this reason, the in-plane technique is not as commonly used to assess sheet metal formability.

2.1.5 Determination of Forming Limits from Experimental Techniques

Data to be plotted on a FLD to obtain the locus of localized necking (FLC) can be obtained by a variety of methods. Traditionally, major and minor strains are obtained from specimens imprinted with a defined grid pattern, usually 2.5 x 2.5 mm or 5 x 5 mm in size. After deformation, the grids closest to the neck, on multiple specimens are analyzed for strains to construct the FLC. This method is often time consuming and has a low local resolution due to the size of the grid pattern. Therefore, a large amount of information is lost between strain measurements, especially in the vicinity of the neck region.

A new method has recently emerged to obtain strain measurements referred to as the digital image correlation (DIC) technique. This technique was principally developed by Sutton et al. (1983) and is based on the photogrammetry principle. It is a non-contact optical method which uses image recognition to analyze and compare digital images acquired from the surface of the sample for displacement and strain measurements (Halim, 2006). Data that is obtained from photogrammetry provides displacement

vectors, local strain values and contour differences of the deformed specimen with very high local resolutions, much greater than that achieved using the traditional grid patterns. The use of the DIC technique in sheet metal forming has improved the accuracy of the information being obtained for FLD development and the relative ease with which the data can be gathered. This method was utilized in the present work and is discussed further in Section 3.5.

2.2 Factors that Influence Formability and FLDs

Investigations in sheet metal forming have shown that the position and shape of the FLC depends on many factors. For this reason, the FLC is not a true material property (Charpentier, 1975). The important factors that influence FLDs are the intrinsic properties of the material itself and several other factors including the test specimen, test equipment and data analysis procedures (Charpentier, 1975; Jain et al, 1994).

2.2.1 Material Properties

Forming limits are highly dependent upon the bulk plastic properties of the material such as the strain hardening index (n) and the strain rate sensitivity (m). In addition, it is well known that on the microscopic scale, plastic deformation processes are highly non-uniform. Therefore, the FLC is also influenced by local variations in the microstructure such as inhomogeneities which cause strain concentrations.

A material's resistance to necking instability is promoted by high work hardening rates, which is associated with a high n-value. This can be deduced from Eqn. 2.3,

mentioned in Section 2.1.3, where the limit strains of a material are based on the strain ratio (β) and the work hardening index (n). Since the strain ratio remains fixed for a given strain path, n has a proportional influence on the limiting strains. Therefore, a material with a large n value will typically have higher limit strains.

The strain rate sensitivity also has a large effect on the FLC. If a material has a positive m value, it increases the strength of the material in the diffuse neck by causing the localized neck to develop more slowly. This allows for additional deformation which increases the materials limit strain. If a sheet metal has a negative m value, the growth of the neck will be accelerated by strain rate softening leading to rapid localization after the diffuse neck is formed. The m value has a similar effect on the FLC as the n value where higher limit strains can typically be achieved with a larger m value (Figure 2.9).

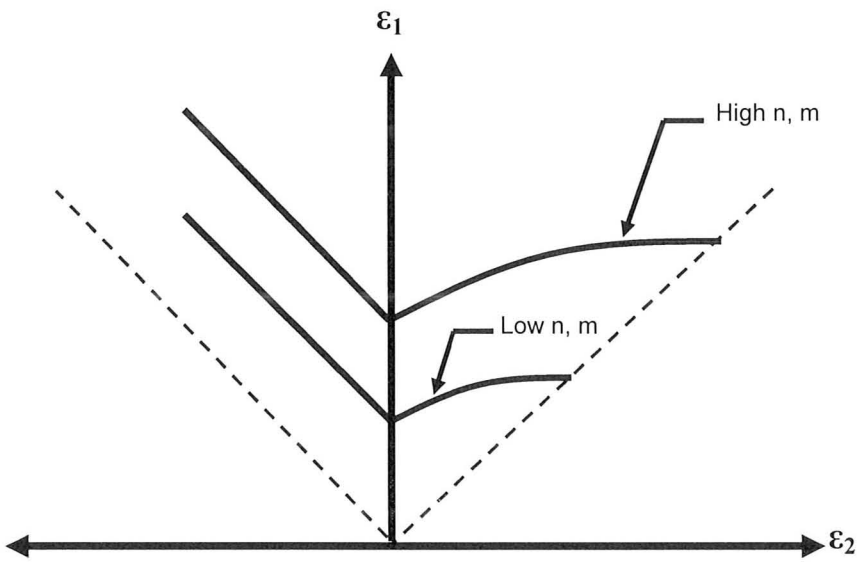

Figure 2.9: Influence of strain-hardening and strain rate sensitive on the forming limit curve.

The influence of n and m values of the FLC for selected materials can be seen in Figure 2.10. As the graph shows, the interplay of the two properties has a large effect on the materials FLC.

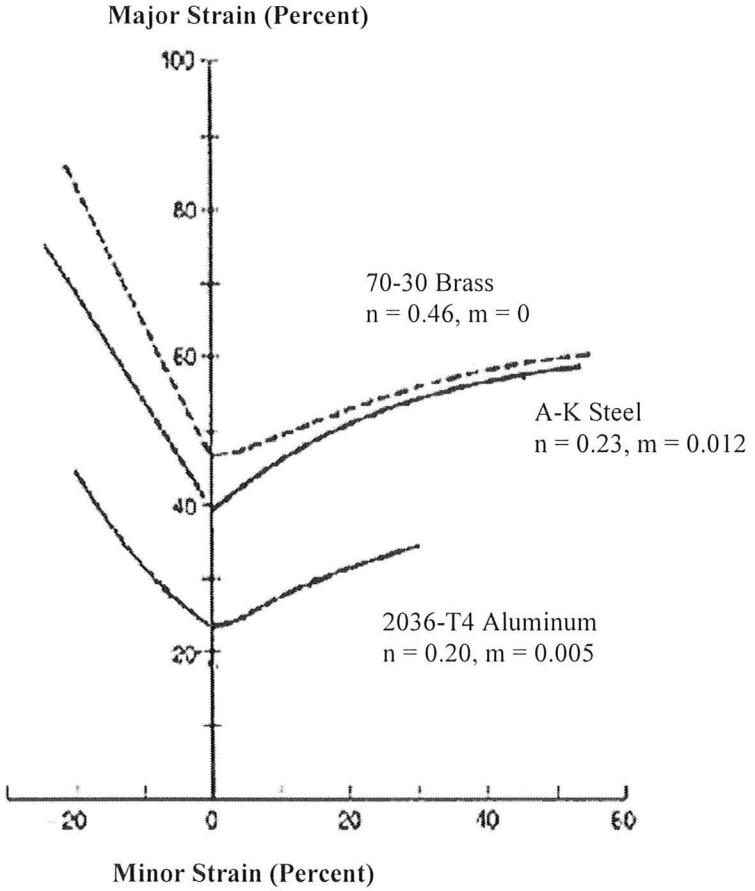

Figure 2.10: The level of FLDs from out-of-plane test for different materials based on the work hardening index and strain rate sensitivity (Ghosh, 1977).

Forming limits are also strongly influenced by local events and short-range variations in the form of inhomogeneities in the material as expressed by the inhomogeneity factor, f_0. Figure 2.11 shows the influence f_0 has on the maximum uniform strain that can be achieved in the M-K groove region for a power law material. A

small decrease in f_0 from 1 to 0.996 can reduce the maximum attainable strain from 0.25 to 0.208 (Hosford and Caddell, 1993). Therefore, knowledge of the events on the microstructure scale is used to understand the influence of material variables on sheet metal failure. This includes a thorough understanding of the nature of the inhomogeneities. Defects that can trigger early strain localization include a non-uniform distribution of impurities, different size and orientation of grains, porosity, varying texture and surface irregularities.

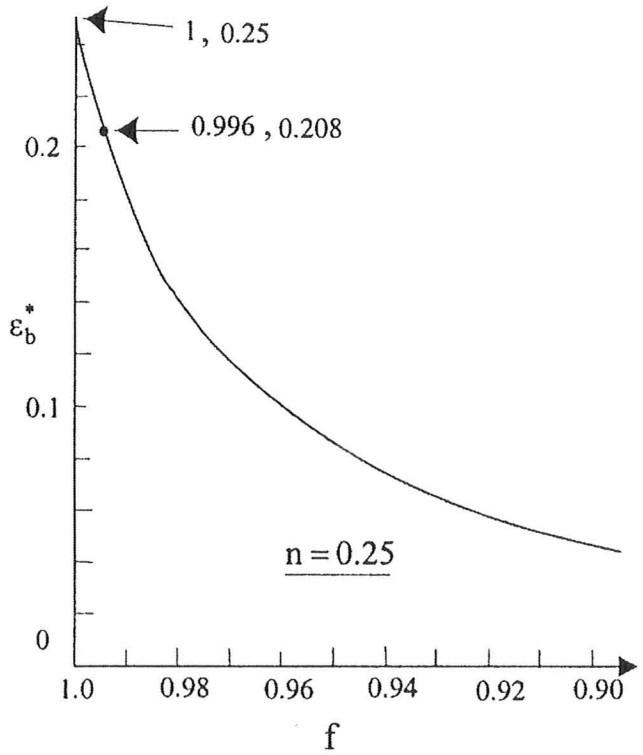

Figure 2.11: Maximum attainable strain in the uniform region of a perfect and imperfect tensile specimen (Hosford and Caddell, 1993).

2.2.2 Mechanical Testing Techniques

Sheet metal formability is a function of the materials properties, as described above, but it is also a function of the particular forming operation to which the material is subjected (Dover and Embury, 1986). The important variables that influence FLDs in terms of the testing technique are the friction, bending conditions and the tooling geometry.

In the out-of-plane testing technique, the sheet is constrained by friction once contact is made and tension in the sheet increases as the punch progresses. Figure 2.12 shows the variations in strain distribution occurring in out-of-plane testing from the pole of the punch to the clamped edge of the sheet. Under frictionless conditions, a state of plane strain exists near the clamped edge of the sheet to a state of approximately balanced biaxial tension near the pole. The pole, showing the largest strain distribution at position A, for the frictionless curve in Figure 2.12(b), ultimately becomes the site of strain localization and specimen failure.

In the presence of friction, large strain gradients can be seen along the punch profile. During deformation, the rate of straining near the pole decreases, causing the deformation region to shift away from the pole. This causes localization to progressively pass through different material elements in the sheet where, as a consequence, the deformation strain cannot concentrate on one imperfection in a continuous manner (Moshksar et al., 2003). In Figure 2.12(b) a peak in the strain distribution can be seen at point B between the pole and the clamped edge under the influence of friction. The

region of failure in the specimen is determined by such factors as the strain hardening and the anisotropy behaviour of the sheet metal (Moshkar et al., 2003).

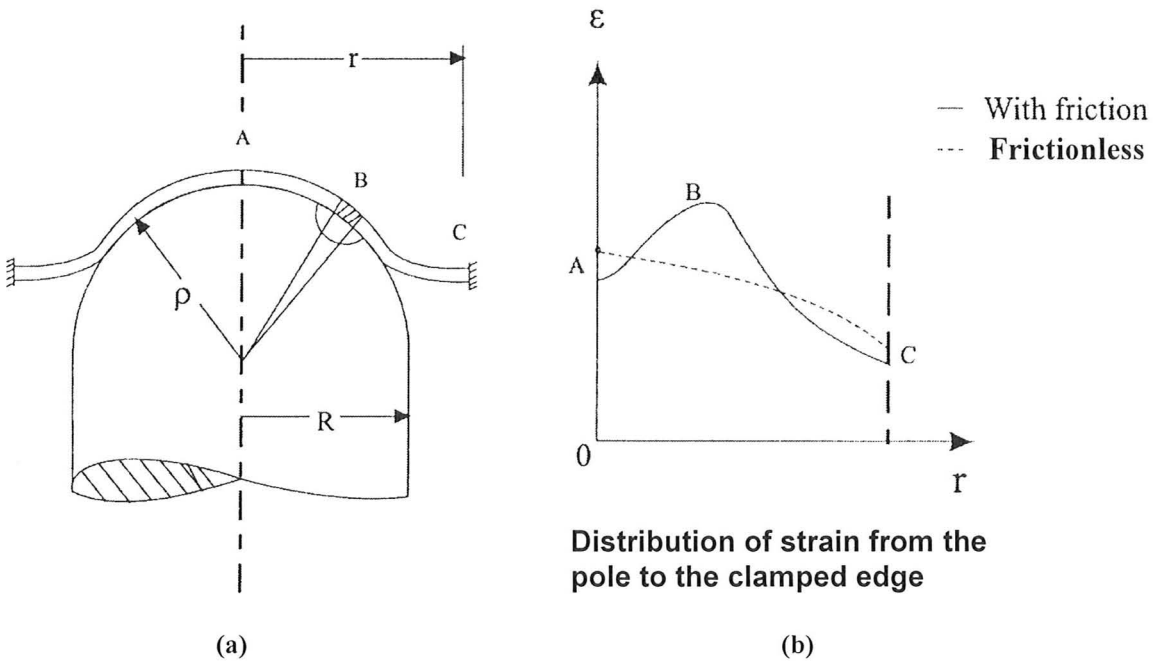

Figure 2.12: (a) Punch profile during stretching for out-of-plane deformation and (b) the resulting distribution of strain along the punch profile under friction and frictionless conditions (Marciniak, Duncan and Hu, 2002).

The influence of punch curvature on the FLC for out-of-plane testing was also investigated. Work by Charpentier (1975) had shown that in punch stretching, the forming limit strains increased with increasing punch curvature (1/R), at constant material thickness under strain paths ranging from plane strain to balanced biaxial tension (Figure 2.13). The increase in the FLC was attributed primarily to the increase in strain gradients as a result of the bending strains imposed on the sheet sample; the magnitude of which depends on the sheet thickness and the punch curvature.

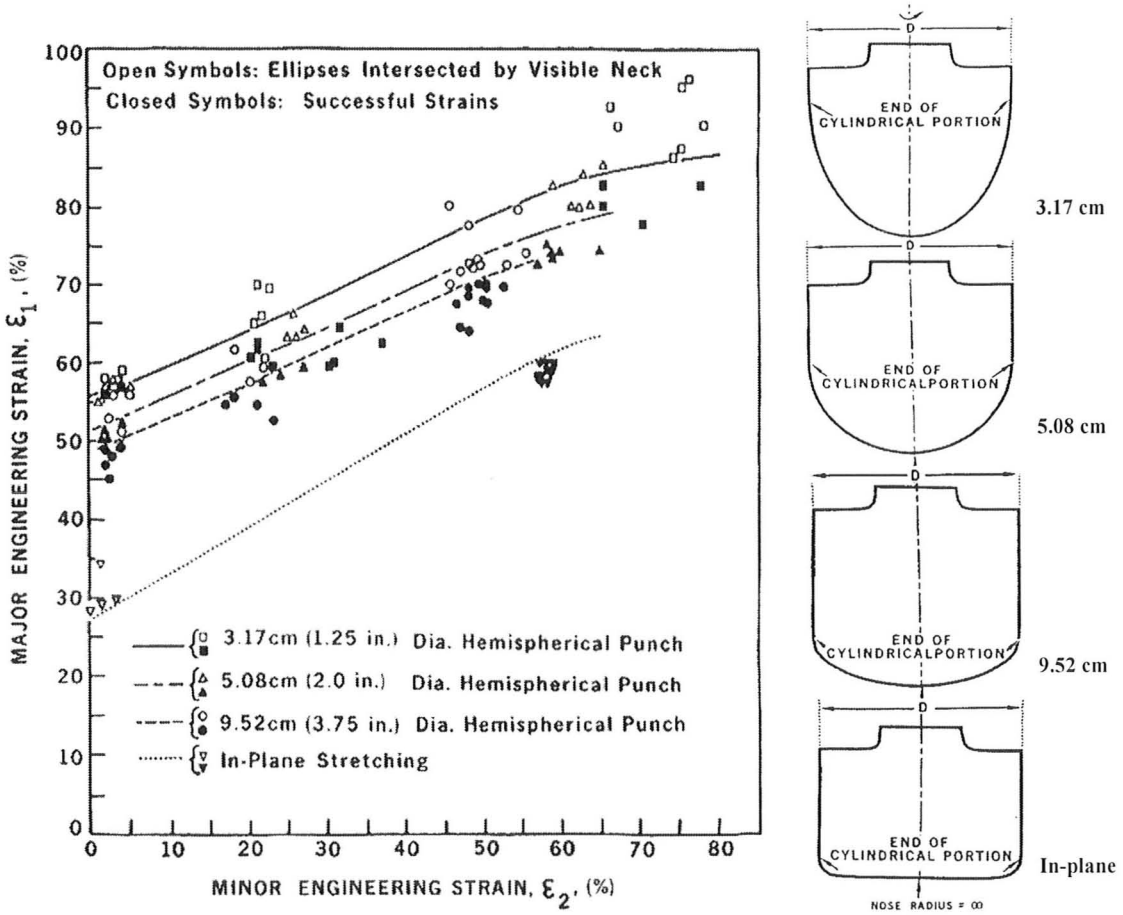

Figure 2.13: Influence of punch curvature on stretching limits (hot rolled, AKDQ steel, 1.83 mm thick). Adapted from Charpentier (1975).

For the in-plane testing technique, as described in Section 2.1.4, the influence of strain gradients, friction and punch curvature are removed. A comparison of the FLCs produced in Figure 2.13 and Figure 2.14 shows that the forming limits determined from in-plane testing is lower than that deduced from out-of-plane testing. This has shown to be consistent with the finding from several authors (Ghosh and Hecker, 1974; Charpentier, 1975; Raghavan, 1995; Moshksar, 2003). The reason for this has been attributed to the fact that when strain localization occurs, it can concentrate at specific

imperfection sites, where the minor strain (ε_2) can gradually approach plane strain conditions. As a result, failure can occur anywhere within the flat-bottom portion of the punch where deformation is uniform and free of the influences that constrain out-of-plane stretching. Ghosh and Hecker (1974) concluded that the presence of strain gradients modifies the instability criterion which applies for in-plane testing and delays the formation of local necking in out-of-plane testing. Therefore, in-plane testing provides a more accurate determination of intrinsic forming limits of the material.

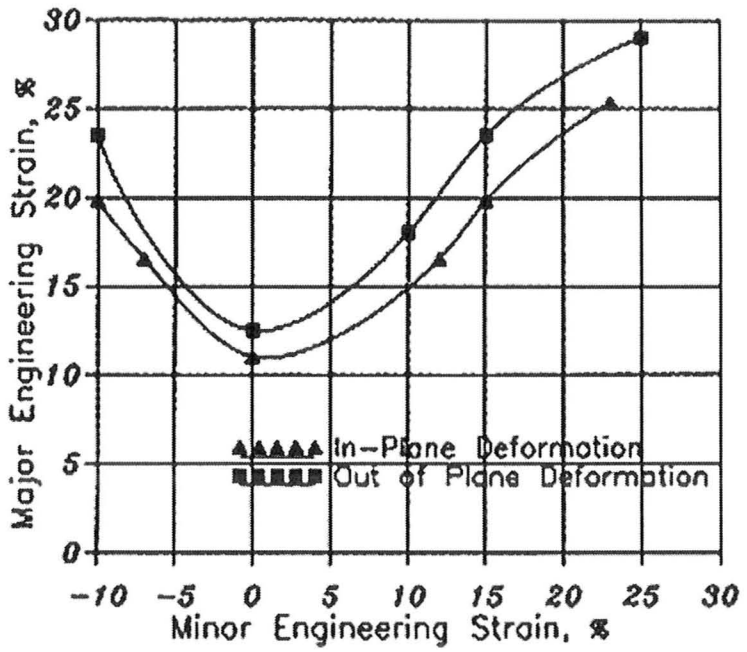

Figure 2.14: Comparison of in-plane and out-of-plane FLDs for aluminum 3105 (Moshksar, 2003).

Overall, in out-of-plane punch stretching, the sheet folds over the punch and is constrained by friction once contact is made (Morris et al., 1987). The location of the localized neck is mainly influenced by the geometry of the test and is relatively insensitive to inhomogeneities in the sheet (Morris et al., 1987). Factors such as friction

and bending strains have been shown to influence formability results by modifying the instability condition at which failure occurs. A summary of the main characteristics which influence the testing conditions has been summaries in Table 2.1.

Table 2.1: Summary of the main characteristics which influence formability testing based on deformation technique

Characteristic	*Out-of-Plane Technique*	*In-Plane Technique*
Deformation type	Constrained	Free
Imposed bending strains	Yes	No
Frictional effects	Yes	No
Sensitivity to inhomogeneities in the material	No	Yes

2.3 Aluminum Alloy 5754

The main objectives of this study is to determine the forming and fracture limits of AA5754 sheet material in the O-temper produced via two different processing routes, direct-chill (or DC) casting and continuous casting (CC). The microstructure of CC material is different from that of DC material. The change in the alloy's microstructure, specifically in terms of particle size distribution and the concentration of alloying elements in solid solution, have been shown to alter the material's mechanical properties (Azari, 2000). This has led to a significant research effort in the last decade to understand the influence of microstructural variations and inhomogeneities on the mechanical properties and formability of AA5754, most specifically in terms of the casting process.

2.3.1 Processing Methods

The production of AA5754 sheet metal can follow two distinct processing routes; the conventional semi-continuous process referred to as direct-chill (or DC) casting and more recently, the continuous casting process (CC). The concept of DC casting was first developed by W. T. Ennor (1942) and provided the basis for modern DC-casting technology, which was introduced by Alcoa during the 1950s. In DC casting, molten aluminum is poured from a furnace through a troughing system into a mold with a cross sectional shape of the desired ingot. Water jets built into the mold spray water onto the ingot to cool the liquid surface and solidify the metal. This process produces ingots with a thickness of 500-600mm. The ingots are subsequently scalped, homogenized and rolled via multistage hot and cold rolling processes to obtain the final desired sheet thickness.

The concept of continuous casting was first developed in the 19th century, but did not reach real commercial use until 1971 by Alcan (Azari, 2000). In CC casting, molten metal is deposited between two tensioned, thin steel belts which operate at a controlled speed. The belts are continuously cooled on the reverse side of the surface in contact with the metal. As the belts move, the liquid metal is cooled and drawn along while new metal is continuously fed into the casting cavity. The process results in a rapidly solidified sheet section with a constant thickness between 10-25mm. Subsequence rolling operations are greatly minimized to obtain the final sheet product, which results in much lower processing costs. The comparison between DC and CC processing routes can be seen in the flow diagram in Figure 2.15

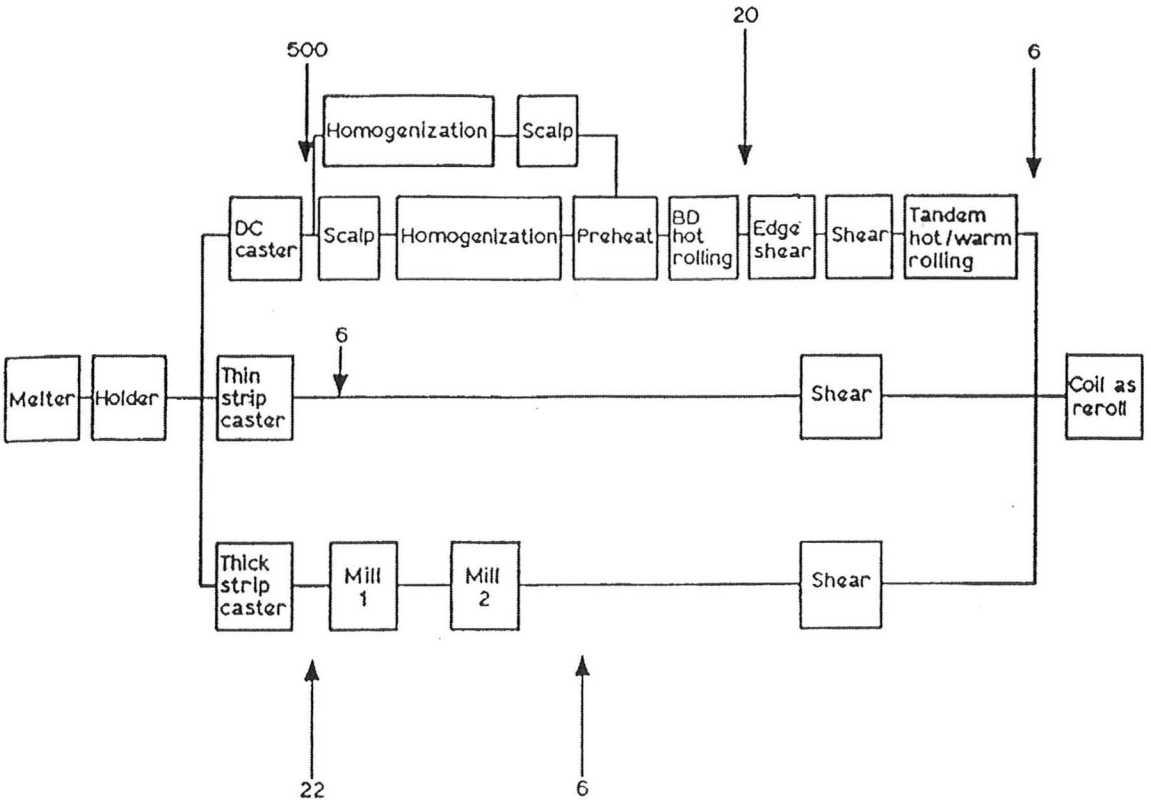

Figure 2.15: Flow diagram for the production of coiled aluminum sheet by DC and CC casting routes with numbers indicating typical metal thickness in mm (Azari, 2000).

The economic advantage of CC casting can easily be seen when compared with DC casting. DC casting requires a number of thermo-mechanical treatments steps before the final product can be achieved, while CC casting produces nearly a net-shape product.

2.3.2 Mechanical Properties

The main alloying element in 5000 series commercial quality aluminum alloys is Magnesium (Mg). Mg provides solid solution strengthening to the alloy which increases the materials lattice resistance to deformation when it is cold worked. Figure 2.16

illustrates the effect of magnesium in solid solution on the yield strength and tensile elongation of common Al-Mg alloys.

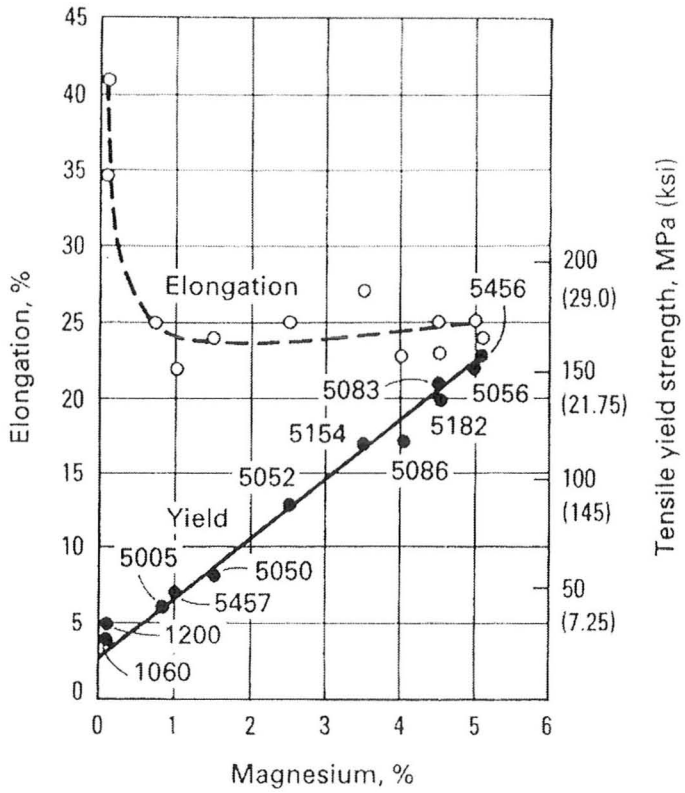

Figure 2.16: Correlation between tensile yield strength, elongation and magnesium content for commercial 5000 series aluminum alloys (Hamilton and Ghosh, 1988).

The graph indicates that as magnesium additions increase, the yield strength increases proportionally but the amount of tensile elongation is reduced significantly up to 1% Mg additions and then remains relatively constant. This is attributed to dynamic strain aging (or DSA) which is associated with materials that exhibit a negative strain rate sensitivity such as AA5754 (Cottrell, 1953; McCormick, 1971; Robinson, 1994). On the microscale, DSA refers to the presence of fast diffusing solute atoms in the Al matrix interacting with moving dislocations during deformation. This mechanism tends to

increase work hardening at low strains, where dislocations are pinned by solute atoms (Hamilton and Ghosh, 1988). At larger strains though, the dislocations move faster than the solute atoms can diffuse resulting in a lower flow stress and a higher dynamic recovery rate. Consequently, material softening occurs followed by a rapid localization of flow in the neck beyond maximum load, leading to catastrophic failure (Kocks et al., 1979).

Macroscopically, DSA is the physical origin of the deformation behaviour referred to as the Portevin-Le Chatelier (or PLC) effect which is a manifestation of deformation into narrow bands which repeatedly transverse the gauge length of the specimen (McCormick, 1987). The PLC effect reveals itself as strong oscillations on the stress-strain curve, referred to as serrated yielding and is characteristic of deformation during a specific regime of temperature, strain and strain rate. This type of behaviour is readily seen in Al-Mg alloys at strain rates between 10^{-6} - 10^{-2} /s and temperatures ranging from -80 to 80 °C (Robinson, 1994; Park, 2006).

The occurrence of serrated yielding resulting from a negative strain rate dependence of the flow stress and DSA has been associated with the reduced formability of aluminum alloys (McCormick, 1987; Kang, 2005). Measurements have shown that the strain at the onset of localized flow is invariably lower than that predicted by the Considère Criterion, thus limiting the amount of total strain (uniform and post uniform) that can be attained. Therefore, an understanding of deformation processes that are occurring, both macro and microscopically is essential in assessing the formability of AA5754.

2.3.3 Microstructure

The typical microstructure of 5000 series commercial quality aluminum alloys contains a large variety of second-phase particles, with a wide size distribution (Girard, 2002). These particles result from the main alloying element Mg and from impurity elements such as Iron (Fe) and Silicon (Si) that are ever present in aluminum alloys due to the use of recycled scrap metal to lower production costs. The size and distribution of these second-phase particles in the microstructure are influenced by the casting process and are found in the form of Mg_2Si, $Al_{12}(Fe,Mn)_3Si$, $Al_6(Fe,Mn)$ and Al_3Fe. Material produced from CC casting does not go through the same number of thermo-mechanical treatments steps before the final product is achieved. Processes like homogenization treatments and extensive mechanical working during rolling operations are typically used to break up the particle distribution networks that form during the casting process.

The microstructural differences in the nature and distribution of the second-phase particles between CC and DC cast alloys has been investigated by numerous authors (Sarkar et al., 2001; Cheng and Morris, 2001; Slamova et al., 2002; Janecek et al., 2003). It is generally concluded that material produced from the CC processing route has a higher concentration of alloying elements in solid solution, a finer and more numerous dispersal of second-phase particles and a smaller grain size than DC cast alloys which originates from the variation in solidification and cooling rates between the two processing routes.

These results were further investigated by Kang et al. (2006) who characterized the distribution and nature of the second-phase particles specifically in the microstructure

of as-received CC and DC cast AA5754. Particle banding referred to as stringers which are a series of two or more particles aligned in the same plane parallel to the deformation direction, were found in both materials (Kang et al., 2006). Stringers are undesirable in the microstructure since they influence the local mechanical behaviour of the material during deformation by causing the rapid accumulation of damage which accelerates the fracture process. Stringers may play a role in strain localization as well, but this is currently being investigated. Typical micrographs of CC and DC 5754 showing differences in particle distribution are presented in Figure 2.17.

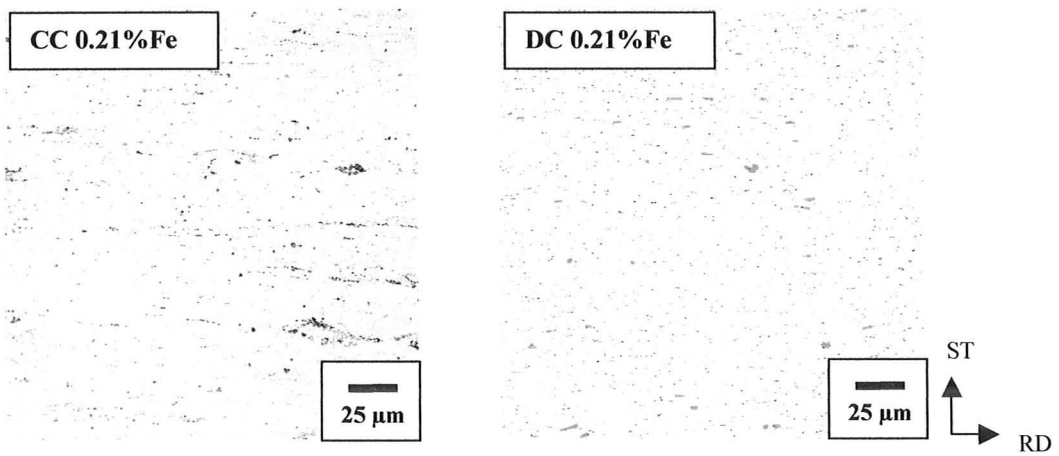

Figure 2.17: Microstructure of AA 5754 (0.21% Fe) showing particle distribution and banding. Pictures taken by Jidong Kang (2004).

Quantitative analysis of the microstructure by Kang et al. (2006) revealed that the CC material has a higher density of stringers than the DC material for the total volume fraction of particles yielded from sheet material with the same chemical composition (Figure 2.18). From the total volume fraction of second-phase particles found, nearly 50% are in stringer formation for the CC material in comparison to only 23% for DC

material. Furthermore, the nature of the stringers are different in the two materials. Stringers associated with the DC material consisted mainly of large Fe based particles while in the CC material the stringers consist of numerous aligned Mg_2Si particles of moderate size (Kang et al., 2006).

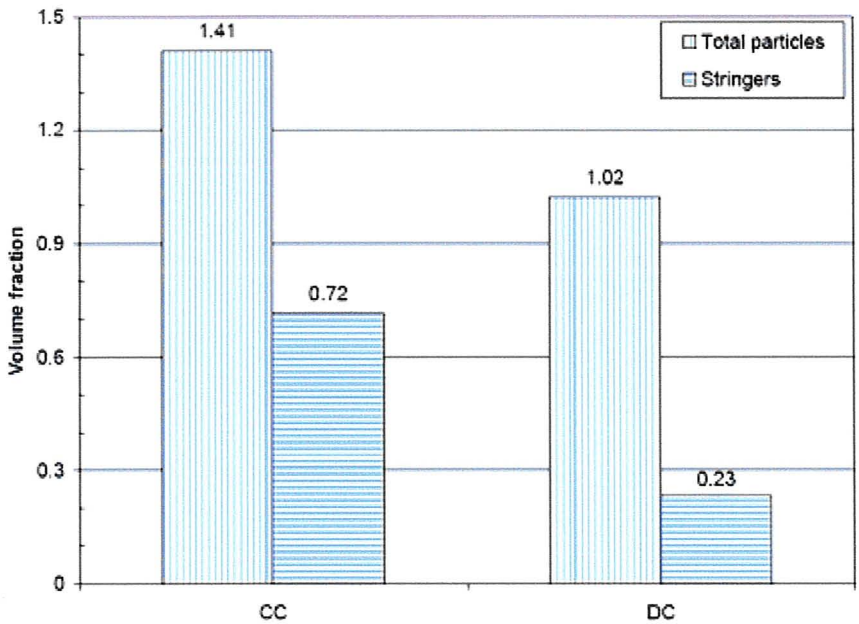

Figure 2.18: Volume fraction of stringer and total particles of CC and DC AA5754 sheet material with similar chemical composition (Kang et al., 2006).

2.4 Shear Localization and Failure

AA5754 sheet materials typically fail by the localization of plastic flow into bands of intense shearing, which accelerates ductile fracture. This type of failure, referred to as shear localization, develops under conditions of low work hardening, usually at large plastic strains and with plastic flow that is highly non-uniform as a result of dynamic strain aging. The shear localization mode of ductile failure occurs in a number of different situations, including the outer portion of cup and cone or double cup fractures

(Figure 2.19(a)) and the tensile fracture of sheet specimens by void sheeting (Figure 2.19(b)). These two fracture modes are readily observed in stretch forming operations.

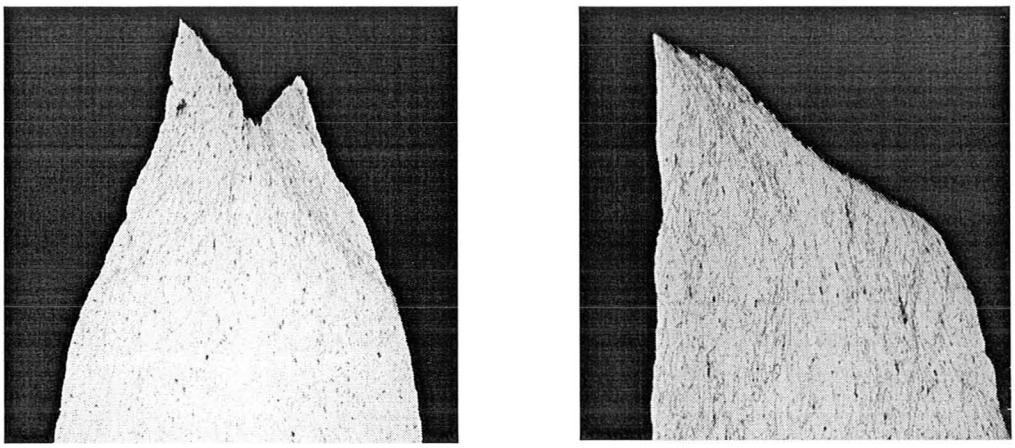

(a) Double-cup fracture profile **(b) Void sheeting fracture profile**

Figure 2.19: Through-thickness sections of AA5754 after punch stretching showing variations is fracture profile.

Fracture processes in which failure by shear localization occurs requires two events to occur. The first being the localization of plastic flow into intense shear deformation regions which penetrate across the polycrystalline material and second, the nucleation and extension of micro-voids around particles in the shear band (Kobel et al., 1986). According to Korbel et al.(1986) the shear localization process begins with the formation micro-bands which consist of accumulated dislocation substructures formed throughout the crystal. These micro-bands spread across the grain boundaries due to high local stress concentrations and become organized into macroscopic bands referred to as macroscopic shear bands. Plastic deformation then continues in the shear bands where

strain rates are orders of magnitude higher than that found in the undeformed portions of the materials.

The microstructure located in the planar regions of the shear band undergo collective shape change by simple shearing along a common plane and direction; both of which are noncrystallographic and are determined by macroscopic flow conditions (Bird et al., (1987). This is accompanied by the nucleation of voids at small inclusion or particles which rapidly coalesce due to instability leading to fracture along specific shear band systems. A schematic of the basic mode of shear localization failure can be seen in Figure 2.20.

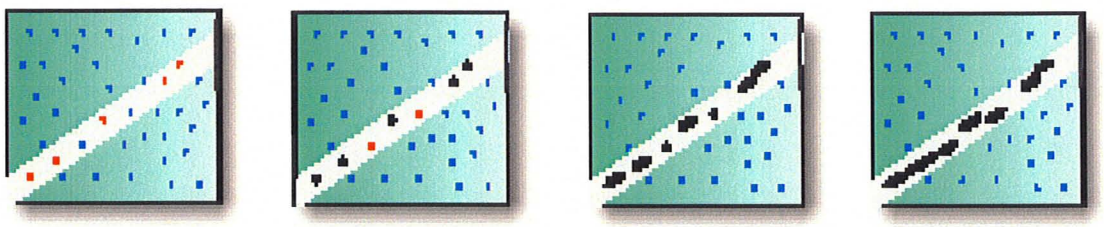

(a) Macroscopic shear band formation **(b) Void nucleation** **(c) Void growth** **(d) Coalescence of voids**

Figure 2.20: Localized shear fracture after strain localization in the form of a macroscopic shear band.

Studies have shown (French and Weinrick, 1976) that there is no evidence of void growth outside the shear band despite the fracture surfaces being covered with strongly-oriented parabolic dimples and that the process is highly dependent upon both the materials mechanical and microstructural properties. For example, second-phase particles have been shown to play a dominant role in the fracture mechanism of the Al-Mg alloys. A non-uniform distribution of particles, such as stringers, can accelerate shear

localization and fracture processes by promoting earlier plastic flow which reduces the overall ductility of the material.

For AA5754, the formation of Fe based second phase particles has been shown to be detrimental to the material's fracture behaviour as they promote the early formation of voids when subject to plastic strains (Spencer, 2002). Figure 2.21 illustrates the variation in fracture strain data with Fe content for standard tensile samples (tested parallel to the rolling direction) and plane strain samples (tested in both the rolling and transverse direction) in conventional DC cast 5754. As shown in Figure 2.21, as the Fe content in the material is increased, the total ductility is significantly decreased. Therefore, knowledge of the nature and spatial distribution of the various second-phase particles in the microstructure can provide insight into the local events that are occurring on the microscale that may influence strain localization and fracture in AA5754.

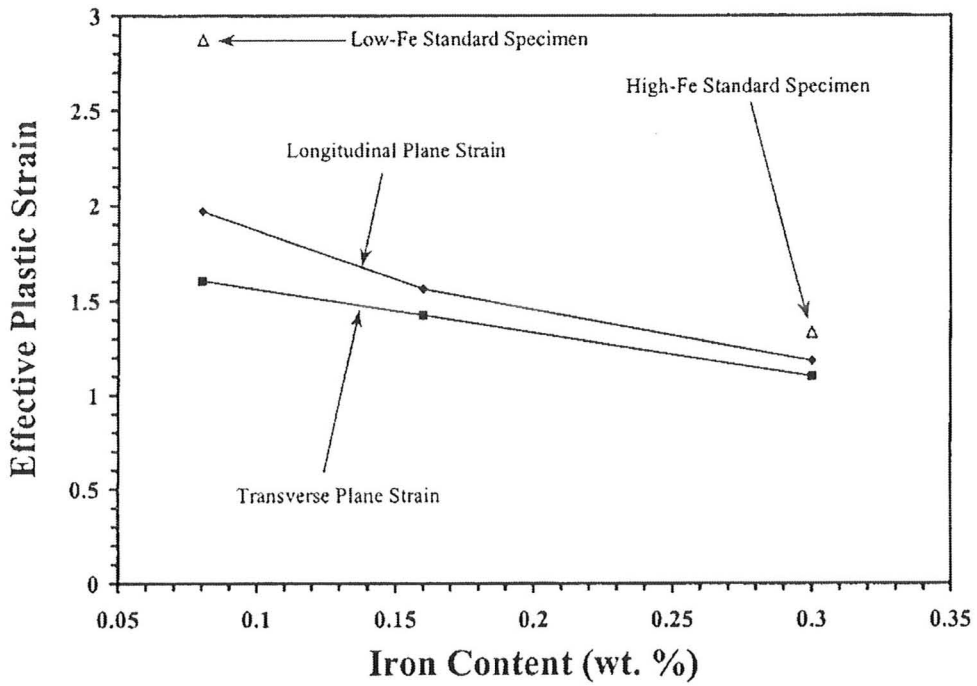

Figure 2.21: Variation of effective plastic strain with iron content (Spencer, 2002).

2.5 Summary

The main objective of the present work is to assess the formability and fracture characteristics of CC and DC cast AA5754 automotive sheet materials by use of the forming limit diagram. A testing technique must be utilized that can successfully differentiate the two materials. The in-plane test methodology developed by Marciniak (1973) was chosen for formability evaluation. This testing technique is sensitive to material inhomogeneities, leading to a more accurate determination of the intrinsic forming limits of the materials. The Marciniak (1973) test methodology was coupled together with digital image correlation (DIC) techniques to provide in-situ strain measurements and deformation analysis throughout the testing process.

A thorough understanding of the deformation behaviour under a variety of strain paths is needed to understand a material's formability. For the case of AA5754, no systematic work has been undertaken in this area. Typically, laboratory observations utilize only one strain path, such as uniaxial tension or plane strain specimens, to characterize the deformation behaviour. Therefore, a detailed analysis of the effect of specimen geometry on the deformation behaviour of CC and DC cast 5754 will be given along with its impact on strain localization and fracture.

Chapter 3

Experimental Procedures

3.1 Materials

AA5754 sheet materials in the O-temper and produced via two different process routes, direct-chill (or DC) casting and continuous casting (CC), were utilized in this study. The as-received materials were cold rolled to a 1 mm gauge thickness and annealed at 450°C for 2 hours to achieve the O-temper state. The chemical composition of both materials were similar, but most importantly, both materials contained the same iron content of 0.21 wt%. The specific composition of each material used is shown in Table 3.1.

Table 3.1: Chemical Composition of Alloy (wt %)

Material	*Al*	*Mg*	*Mn*	*Si*	*Fe*
Continuous Cast (CC) (provided by Alcan)	balance	3.42	0.23	0.05	0.21
Direct-chill (DC) (provided by GM)	balance	3.11	0.25	0.06	0.21

3.2 Standard Tensile Specimens

Uniaxial tension tests were performed at room temperature. All specimens were machined in the rolling direction according to ASTM standard E8M-04 as shown in Figure 3.1.

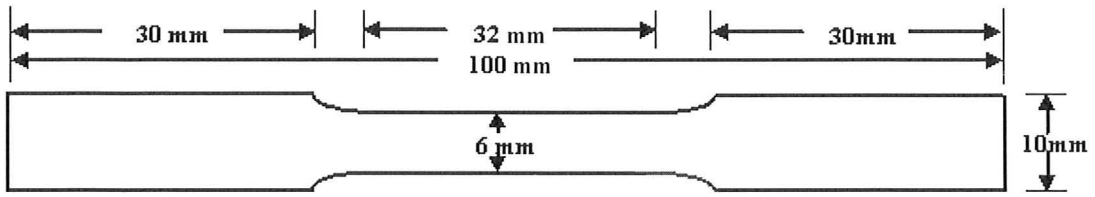

Figure 3.1: ASTM Standard subsize specimen dimensions for tensile testing.

To obtain the tensile properties of each material, all tests were performed using an Instron 5566 screw-driven tensile machine with a 10 kN load cell. All specimens were tested at the same crosshead velocity of 1 mm/min and plotted as true stress versus true strain curves. From this data the yield strength, tensile strength and uniform strain were determined. The strain hardening exponent was also determined using the Considère criterion. These results are reported in Chapter 4 (section 4.1).

3.3 Formability Testing

The forming limit diagram (FLD) for CC5754 and DC5754 were obtained using the Marciniak test method (1973). The tests were performed using a hydraulically driven Interlaken 150 Ton double action servo press. The Marciniak test tooling was designed at McMaster University by Dr. Mike Bruhis (Figure 3.2) Two Marciniak punches were designed for testing and can be seen in Figure 3.3. The first punch was machined from mild steel and had a draw radius of 0.250 inch. This punch was solely used for testing specimens that follow a strain path on the left-hand side of the FLD. It was determined from testing that a second punch would be needed for testing specimens that follow a strain path on the right-hand side of the FLD. The new punch design consisted of tool steel with a larger draw radius of 0.500 inch.

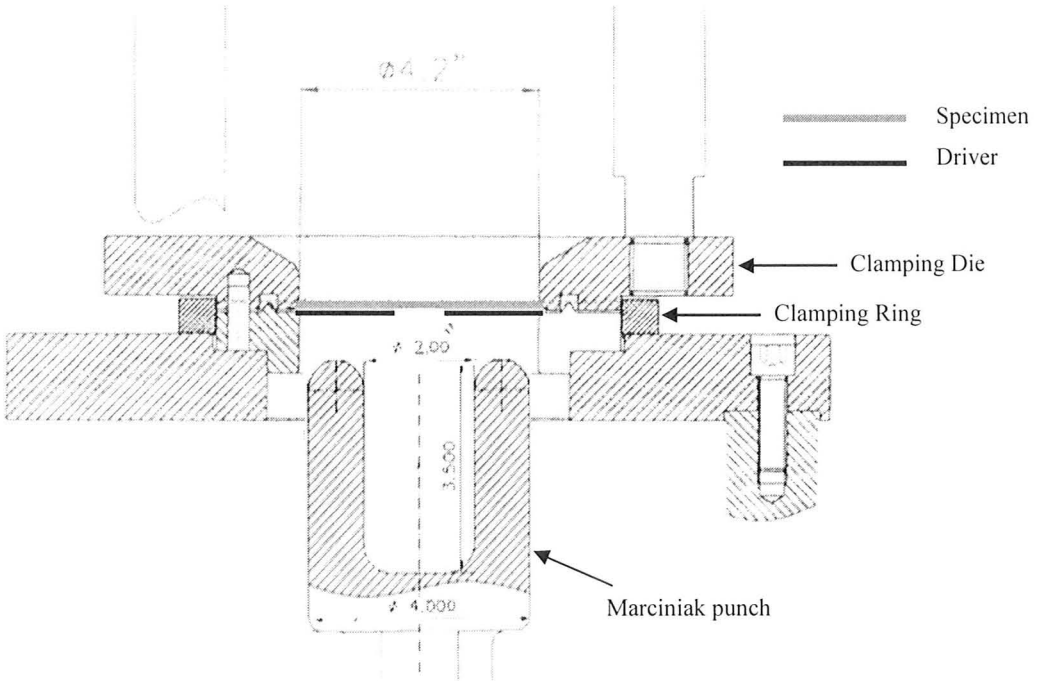

Figure 3.2: Marciniak test method setup for formability testing showing punch and sample setup (specimen positioned above driver for digital image analysis) (Bruhis, 2005).

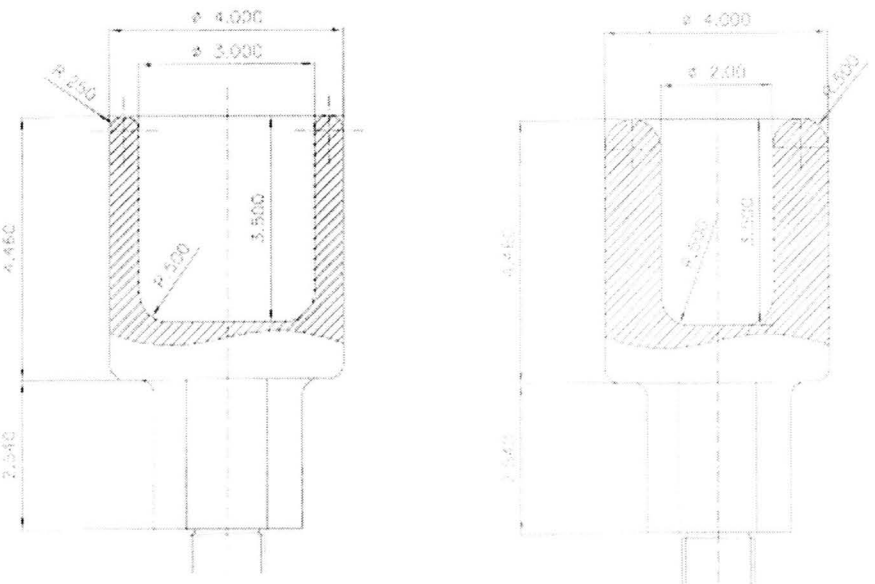

(a) Mild steel punch with 0.250 inch draw radii (b) Tool steel punch with 0.500 inch draw radii

Figure 3.3: Marciniak punch designs produced by Mike Bruhis, 2006 (dimensions in inches).

All samples were positioned squarely in the clamping dies with no lubricants used between the punch, driver or specimen. All testing was performed at a speed of 0.01 inches per second (15 mm/min) and a clamping load between 20,000-45,000 lbf (88,965-200,170 N) depending on specimen strain geometry. For samples tested on the left-hand side of the FLD (negative minor strain region) half the specimens were tested to fracture while the other half were tested up to the point of localized necking for damage analysis. All samples tested on the right-hand side of the FLD (positive minor strain region) were tested to fracture since the onset of necking could not be captured.

3.3.1 Marciniak Test Specimen Geometry

To obtain a range of strain paths for FLD construction, six specimen geometries were used to plot the FLDs. All specimens were prepared by machining and following the guidelines given in ASTM standard E2218-02 (standard test method for determining forming limit curves). Specimens which produce a strain path in the negative minor strain region are given in Figure 3.4 and have design widths of 0.5 inch (12.7 mm), 1 inch (25.4 mm) and 2 inch (50.8 mm). Specimens with larger widths shift the strain path towards the plain strain path. To produce a strain path in the positive minor strain region of the FLD, larger width specimens were used and can be seen in Figure 3.5. A specimen width of 4 inch (98 mm) produced a condition relatively close to plane-strain while for stretching conditions or biaxial tension a 5 inch (122.5 mm) and 7 inch (171.5 mm) width specimens were used.

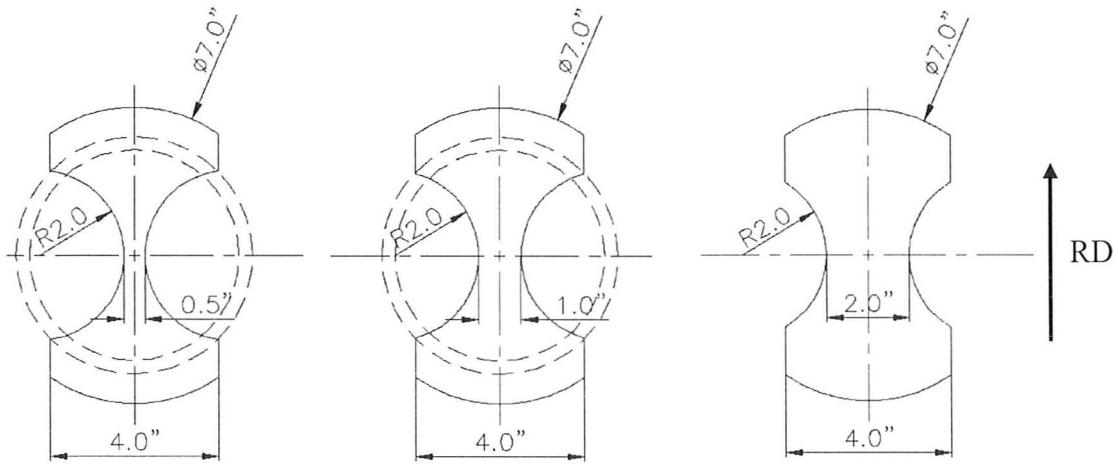

(a) 0.5 inch geometry (b) 1 inch geometry (c) 2 inch geometry

Figure 3.4: Specimen geometries for left-hand side of FLD showing the clamping ring and rolling-direction of the material (dimensions in inches). Drawings produced by Situ Quan and Mike Bruhis, 2004.

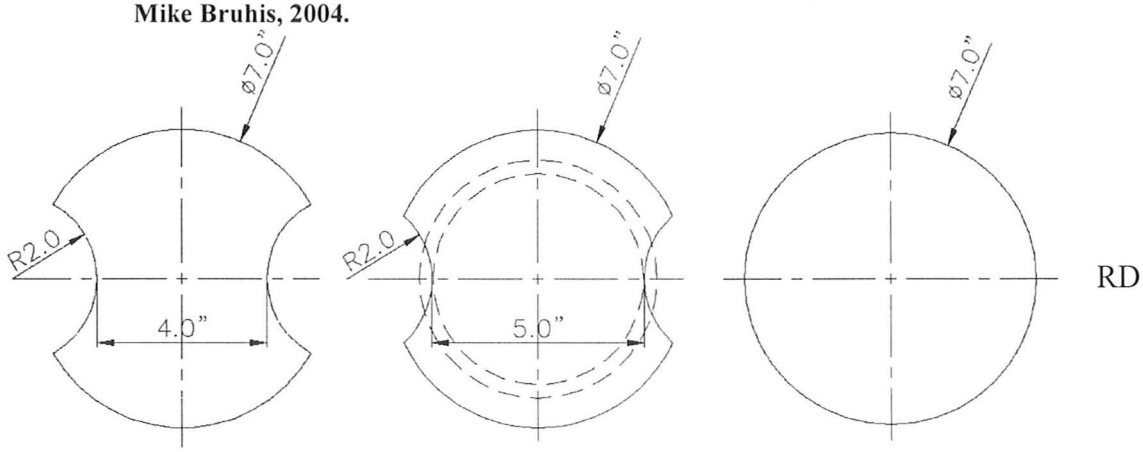

(a) 4 inch geometry (b) 5 inch geometry (c) 7 inch geometry

Figure 3.5: Specimen geometries for right-hand side of FLD (Quan and Bruhis, 2004).

3.3.2 Marciniak Test Driver Geometry

To produce a strain path on the right-hand side of the FLD using the Marciniak test method, a driver was utilized for the 4 inch, 5 inch and 7 inch width specimens. The driver and the test blank were tested as a pair with the driver blank placed on the punch side in the die prior to testing. The driver design was similar to the specimen geometry but with the addition of a central hole (Figure 3.6). The radius of the hole and the

material was determined by trial and error. For our testing purpose, the driver material was determined to be mild steel with a sheet thickness of 0.7 mm. All drivers were machined to ensure that the hole did not contain any burred edges which would influence the formability results by premature specimen failure.

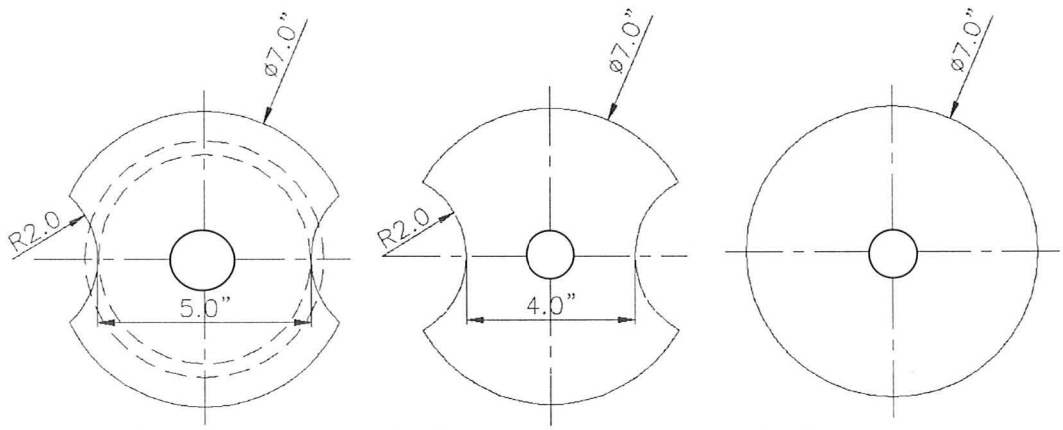

(a) 4 inch geometry **(b) 5 inch geometry** **(c) 7 in geometry**

Figure 3.6: Driver geometries for right-hand side specimens. Adapted from Quan and Bruhis, 2004.

3.4 ARGUS Strain Measurement System

In order to measure the surface strain on the deformed specimens, a commercial optical strain measurement system, ARGUS, was used (GOM, 2001). This system is based on the digital image correlation (or DIC) method and provides a full-field strain map of the deformation. The strain maps of the drivers were analyzed by this system. The system was also used as an alternative method for analyzing the specimen test results for verification of another on-line optical strain measurement system, ARAMIS (GOM, 2005). This system was utilized for test specimens only and is discussed further in section 3.5.

The ARGUS system consists of a high-resolution CCD camera with 16 mm lens, an adjustable camera tripod and a dedicated image processing and analysis software. ARGUS software uses the photogrammetric principle to define the 3D coordinates of each dot on the specimens surface (GOM, 2001). From this, the various strain components are calculated with a typical accuracy in the range of 0.5% as given by the manufacture GOM (2001).

3.4.1 Specimen Preparation

All test specimens and drivers were electrochemically etched prior to testing. The pattern etched onto the specimens consisted of dots with a diameter of 1 mm and separated by a distance of 2 mm (center-to-center) from each other (Figure 3.7). The pattern was applied using a grid stencil placed on the metal surface. An absorbing cotton pad was soaked with an electrolytic solution which was placed on top of the grid. Any exposed surface in contact with the solution became oxidized when current was passed through the sheet material which produced the dot pattern. The electrochemical etching conditions are shown in Table 3.2. During the forming process, the etched dot pattern is distorted as it deforms with the sheet. The change in separation distance between the dots is used by the ARGUS system to measure the strain distribution on the specimen.

Table 3.2: Parameter settings for electrochemical etching. Solutions provided by Automation Systems and Integration.

Material	*Electrolyte*	*Voltage Setting*	*Current (amps)*	*Time(s)*
Aluminum	SC-44	DC	15-20	30
Steel	53NC	AC	15-20	60

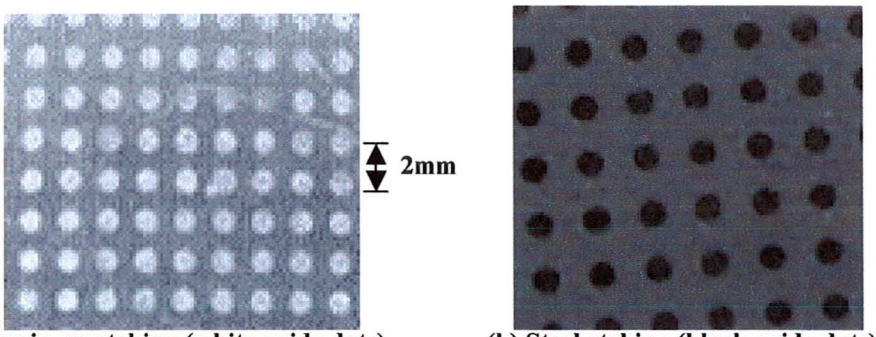

(a) Aluminum etching (white oxide dots) (b) Steel etching (black oxide dots)

Figure 3.7: Electrochemically etched dot patterns for ARGUS Analysis.

3.4.2 Test Conditions

The specimen was analyzed by placing calibration markers around the deformed specimen (Figure 3.8). Images were recorded from three different viewing directions. For each viewing direction approximately 5-10 pictures were taken. Altogether, a 360° view of the specimen was taken. Care was taken in the following areas: a level, mark-free surface was used for specimen analysis, the calibration markers were placed securely around the specimen and the camera was focused in all three viewing directions. This helped ensure an error-free process analysis.

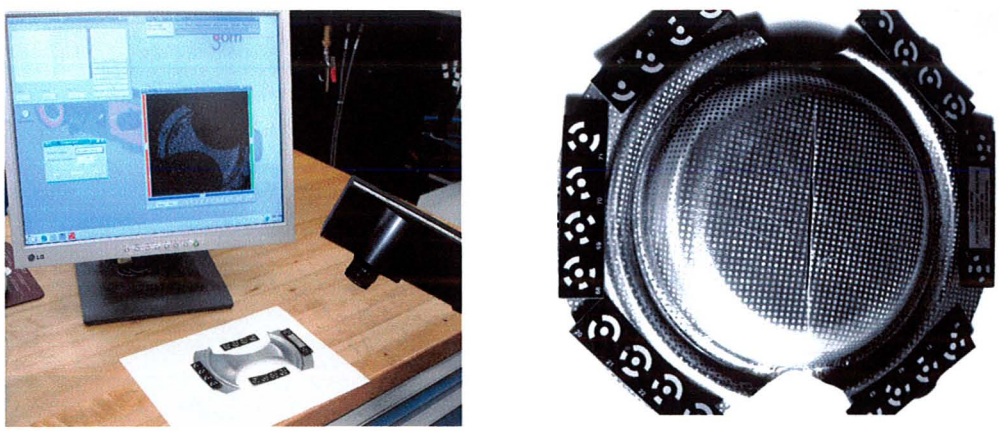

Figure 3.8: Example of ARGUS system test set-up and deformed specimen with calibration markers for analysis.

3.4.3 Data Analysis

Once the strain map was produced, a section along the gauge length at mid-width was taken across the localized neck region (or fracture) to obtain the distribution of major and minor strains (Figure 3.9). In some cases, calculation errors occurred with the system. This included the misidentification of a dot which results in a mesh not properly aligned therefore showing an artificial strain value or areas where the system was not able to identify the dots and no strain was calculated. In such cases, the section was redrawn to avoid these regions on the strain map.

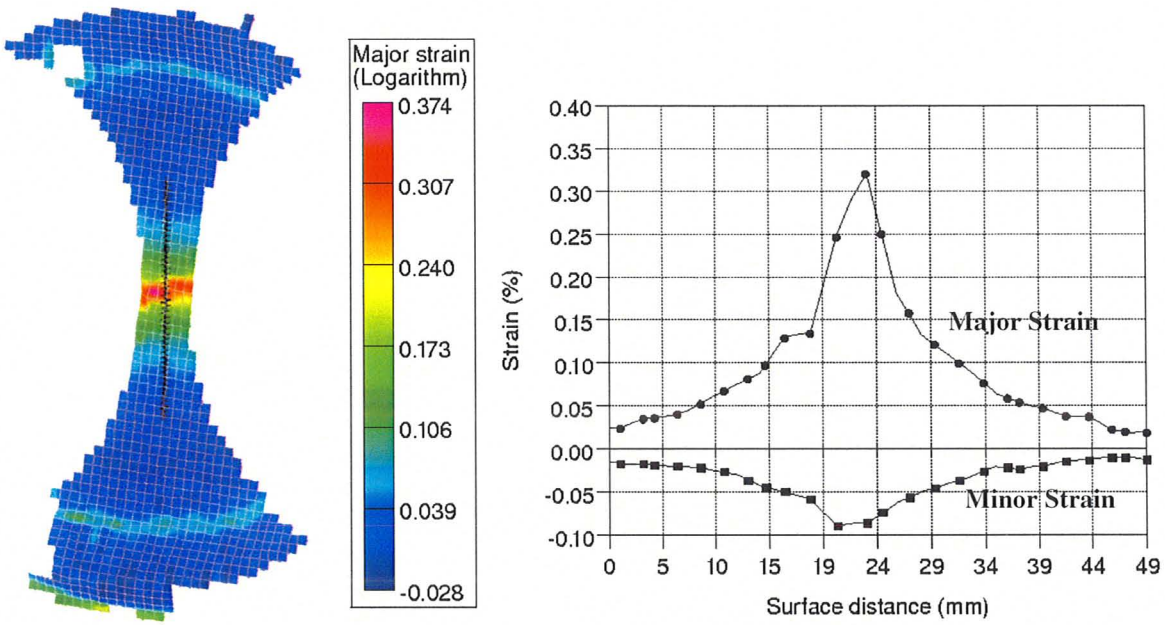

(a) Strain map for 0.5 inch geometry specimen **(b) True major and minor stain plot**

Figure 3.9: Example of ARGUS results showing defined section and the true major and minor strain plot across the section.

To assess the error in the system, calculations on an undeformed specimen were carried out. The exact test conditions were set-up as that for specimen analysis. The true

major and minor strain distribution across the specimen's surface (one section along the x-axis and one along the y-axis) can be seen in Figure 3.10. The maximum error in the true strain components was found to lie between ±0.025.

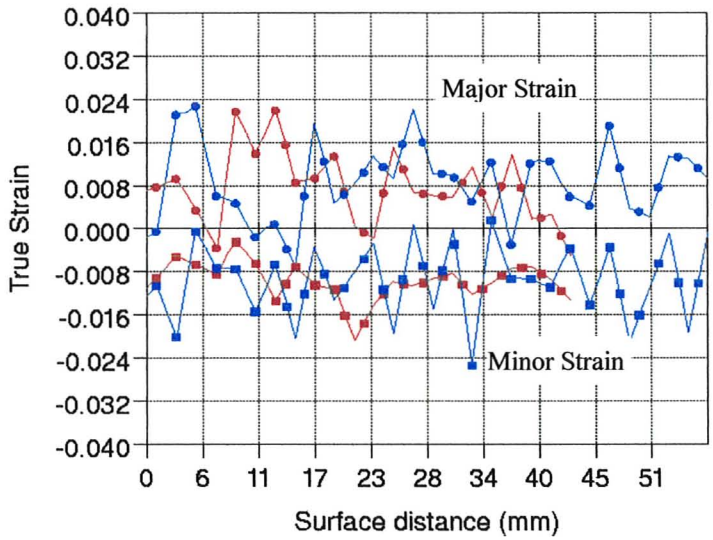

Figure 3.10: True major and minor strain plot from ARGUS system on undeformed specimen.

3.5 ARAMIS System

In-situ strain measurements were performed using the on-line ARAMIS system. This system produces deformation analysis and strain maps throughout the testing process. Therefore, complete deformation history of the specimen from beginning to fracture could be recorded.

3.5.1 Specimen Preparation

All test specimens (excluding the drivers) after electrochemical etching and prior to testing were prepared for ARAMIS based testing. This consisted of having a fine mist

black and white water-based ink sprayed onto the specimen surface using an Iwata Eclipse 0.5 mm nozzle airbrush gun.

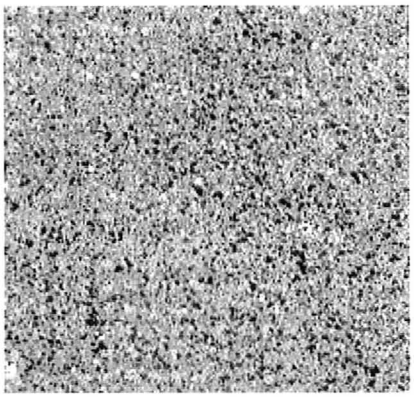

Figure 3.11: Regular fine mist ink pattern applied to AA5754 specimens for ARAMIS testing.

During the deformation process, the 3D coordinates of the surface of the specimen, according to the ink pattern, were mapped throughout the various stages using photogrammetric evaluation procedures (GOM, 2005). A high contrast random ink pattern was applied to the specimen surface, as shown in Figure 3.11, to ensure sufficient accuracy of the measured strains.

3.5.2 Test Conditions

The ARAMIS system consists of two CCD cameras (resolution of 1280 x 1024 pixels) each with a 16 mm lens, a camera mounting plate for the Interlaken press, a calibration sensor for 3D analysis, a controller for the external control of the image-data acquisition and evaluation software. A photograph of the process set-up can be seen in Figure 3.12.

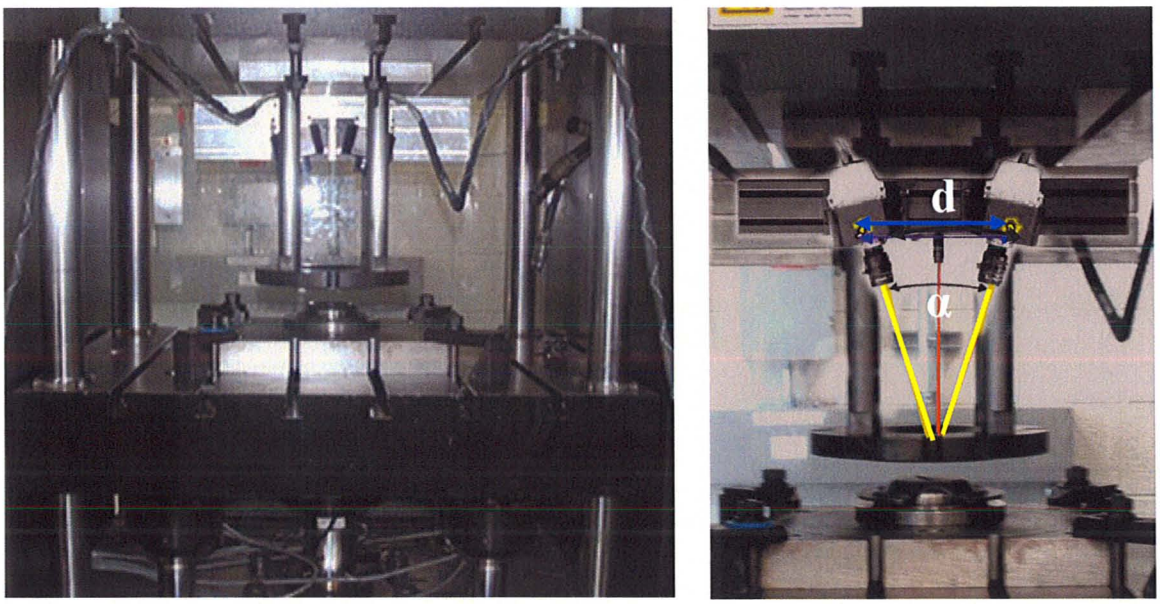

Figure 3.12: ARAMIS system set-up with Marciniak punch showing camera separation distance (d) and angle (α).

Prior to testing, the system was calibrated using a calibration object (Figure 3.13). The calibration object consisted of a given arrangement of white points which the system uses to define the measuring volume in 3D for the test process. To minimize measurement error, an appropriate measuring volume had to be used during testing. This means that the deformation process must occur within the defined measuring volume to ensure a strain measuring accuracy of 0.01% (GOM, 2005). For our purpose, the calibration object with a measuring volume of 35 x 28 x 28 mm^3 was used. The camera set-up and calibration procedure used were approximately the same each time testing was done and followed the ARAMIS user guide. The cameras were placed 12 cm apart on the mounting device which resulted in a camera angle between 25-30°.

To assess the accuracy of the calibration, a simple test provided by the system was performed. Three images were taken of the calibration object at various distances to the

camera. The calibration objects are defined by the separation distance between the large white dots in the x-axis as given in Figure 3.13. For the calibration object used in our tests, the measured distance was 21 mm. The system then computed the measured distance between the large white dots as measured from the calibration. The result obtained from the calibration test was 21.003 mm. This resulted in a measuring accuracy within 0.01% as given by the manufacturer of the system.

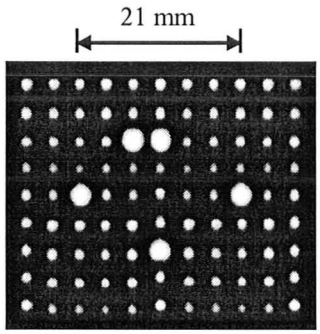

Figure 3.13: Calibration object for ARAMIS system showing the given arrangement of white points.

After the calibration was complete, a measurement "project" was created for each test in which the appropriate testing conditions are set-up (3D versus 2D analysis) and all the data recorded from the system was stored. All projects were created with an image recording rate of one image per second which determines the number of images the project will have. This rate was chosen since localized necking and failure can occur quickly in AA5754. A rate of one image per second or higher ensured that at least one image showing localization could be captured.

3.5.3 Data Analysis

Computations of the projects were done following the guidelines in the ARAMIS user manual. All projects were computed using a facet size of 15x13. For forming limit

analysis, a section was taken along the gauge length at mid-width near the centre of the specimen on the 3D strain map (Figure 3.14(a)). Data from the stages just prior and up to localized necking from the section were plotted to obtain the major and minor strain distributions (Figure 3.14(b)).

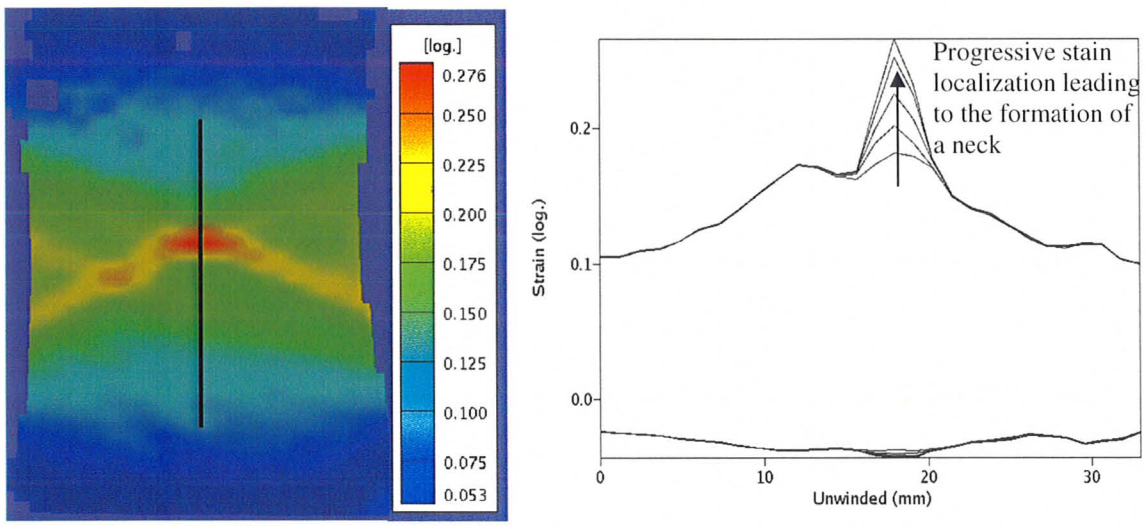

(a) ARAMIS strain map for 2 inch width specimen showing the section line used for receiving data at various punch displacements

(b) True major and minor strain plot of section line (black) showing multiple stages prior to fracture.

Figure 3.14: Example of ARAMIS system results used for forming limits evaluation.

Further processing of the specimen strain maps was performed to observe the local true strain as a function of the overall global true strain. The strain values were estimated by using DIC section strain plots from various stages of the deformation process. An example of this is shown in Figure 3.15, where (a) is a strain map captured at one stage of the deformation process and (b) is the corresponding true major strain plot for the shown section. From the plot in Figure 3.15 (b), the global strain was defined as the average strain along the specimen gauge length, excluding the strain values found in

deformation bands (red). The local strain was defined as the maximum strain found along the specimen gauge length, coinciding with deformation bands.

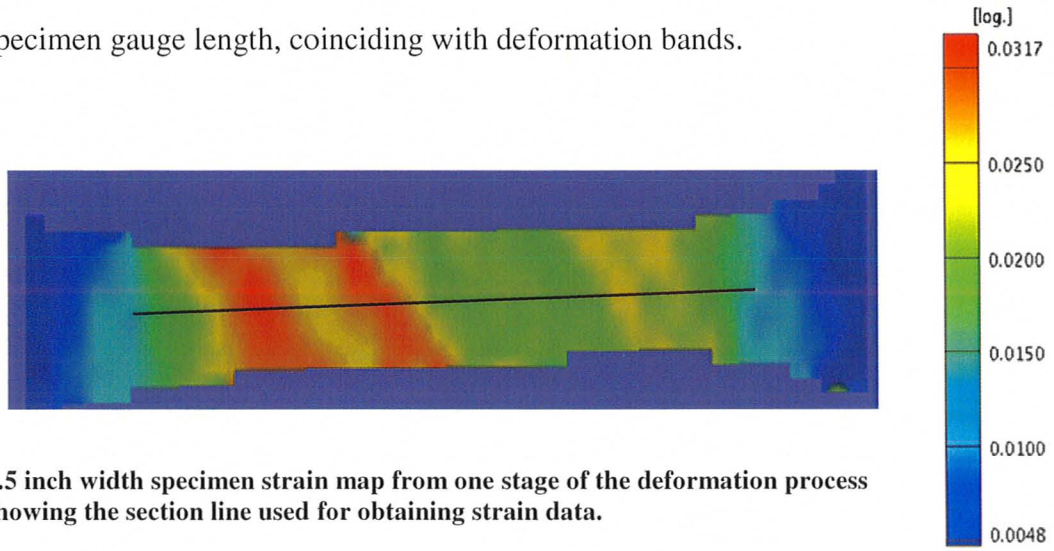

(a) 0.5 inch width specimen strain map from one stage of the deformation process showing the section line used for obtaining strain data.

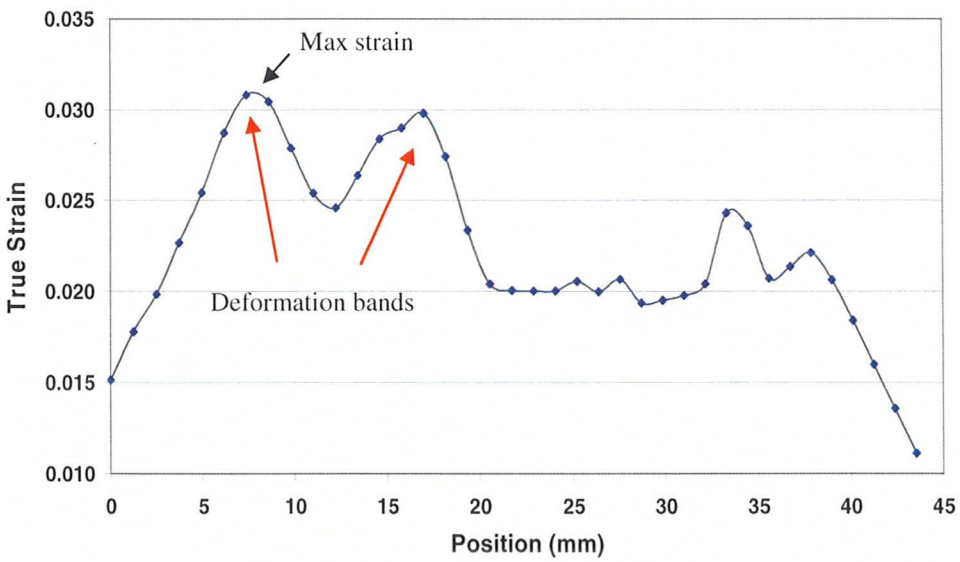

(b) Corresponding true major strain plot from the deformation stage shown in (a) from the section line.

Figure 3.15: Example of ARAMIS system results used for deformation band strain evaluation.

The local true strains were plotted against the global true strains for each material and specimen geometry, such as shown in Figure 3.16. According to the graph, the straight line represents homogenous plastic deformation where the local true strain equals

the global true strain. When the local strain begins to deviate from the global strain, the difference in value indicates of the amount of strain carried by the deformation bands, referred to as the band strain. This can be seen in the plot where the black arrows represent the increasing band strain with global strain. The plot was also used to estimate the maximum strain carried in the deformation bands prior to strain localization. This was carried out by extrapolating the two linear regions of the curve and finding the intersection point (Figure 3.16). This method again was used for both materials, for all the tested strain paths.

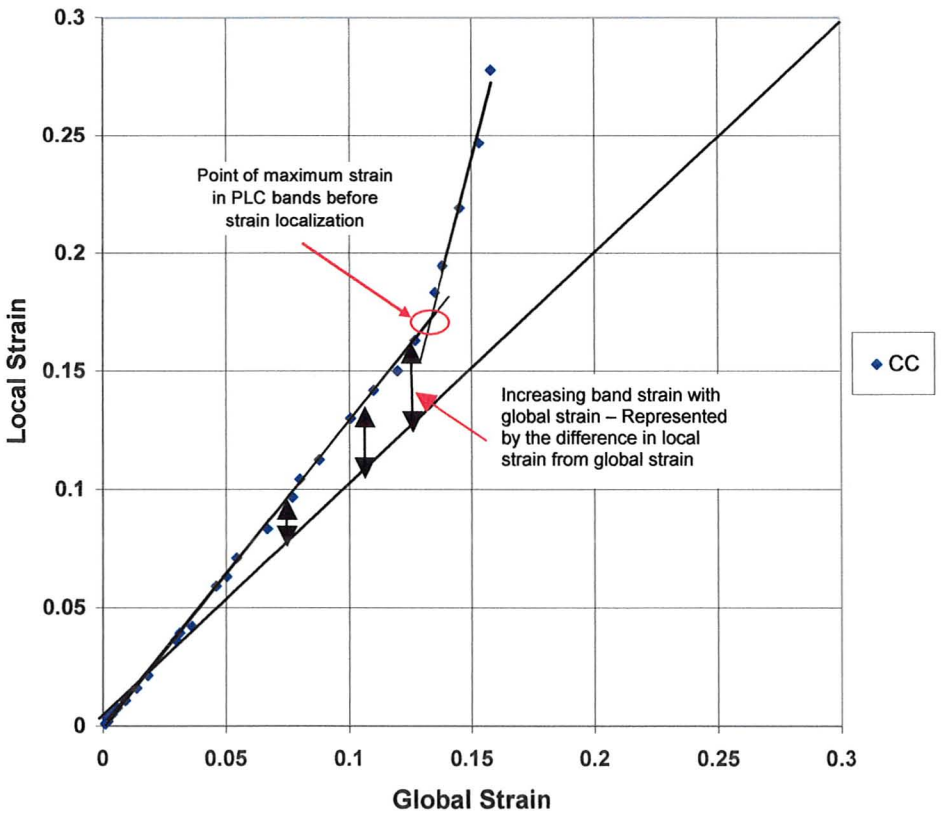

Figure 3.16: Plot of local true strain as a function of global true strain for 1 inch width geometry. The point of maximum strain carried in the deformation band is shown through graphical extrapolation.

3.6 Optimization of Test Conditions

The proper use of the Marciniak test method for FLD development relies on three critical parameters: (1) the driver blank material, (2) the friction conditions around punch profile and (3) the diameter of the driver hole. These parameters were investigated in this study to obtain optimal testing conditions for formability analysis of the 4 inch, 5 inch and 7 inch width specimens. Specimen geometries on the LHS of the FLD (0.5 inch, 1 inch and 2 inch) were not affected by these parameters.

3.6.1 Determination of Driver material

The first parameter to be evaluated was the proper selection of the driver material. The driver material selection was limited in sheet thickness due to the constraints of the clamping die and only sheet material less than 1 mm in gauge thickness could be utilized. Three driver materials were investigated, a 1070 mild steel (0.75 mm sheet thickness), an annealed 70/30 brass (0.85 mm sheet thickness) and a stainless steel SS321 (0.90 mm sheet thickness) respectively. These materials were chosen for their formable properties and success in previous works as driver blank material (Raghavan, 1994; Moore et al., 2002; Moshkar et al., 2003).

The 7 inch width specimen was utilized to compare the driver materials (Figure 3.5(c) and 3.6(c)) using DC5754 material. All three drivers were prepared according to section 3.4 and had a central hole diameter of 1.4 inches (49.8 mm). The results from the major and minor strain distribution across the hole profile obtained from the ARGUS strain measurement system can be seen in Figure 3.17. From the plot, the 1070 mild steel

shows the highest formability of the selected materials and was therefore selected as the driver blank material.

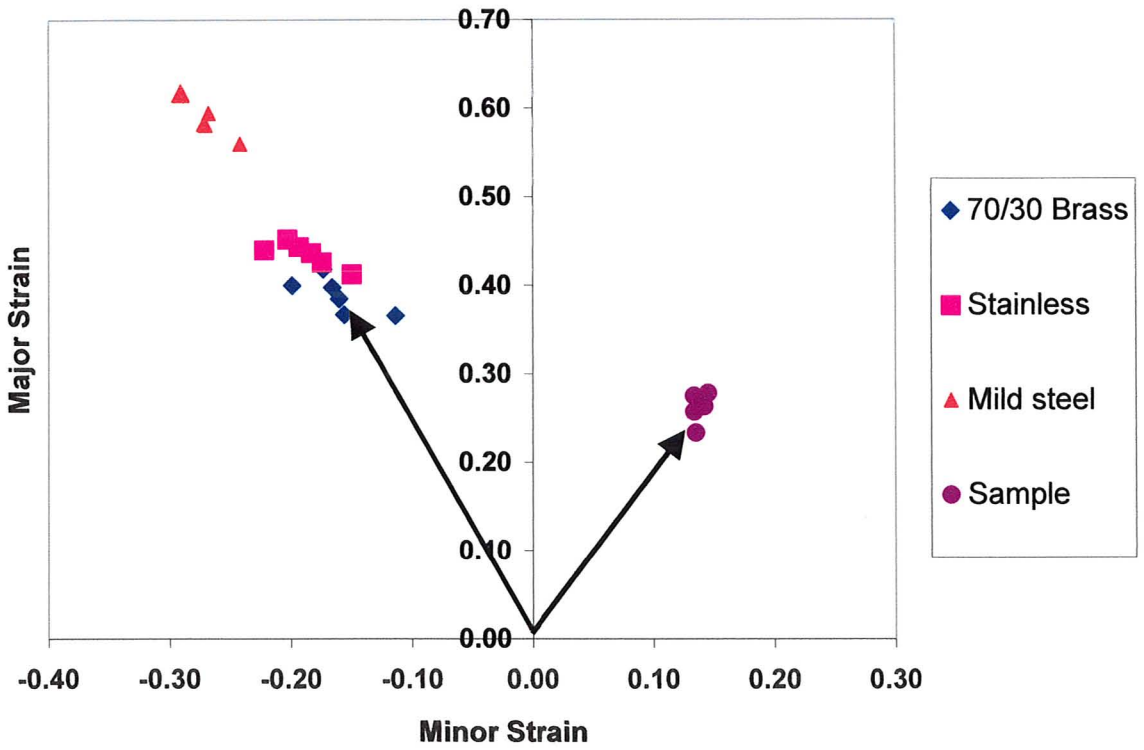

Figure 3.17: True major and minor strain plot of driver material selection for DC5754 7 inch geometry sample showing sample and driver strain paths.

3.6.2 Determination of Punch Profile

Two conditions must be fulfilled when determining the success of the Marciniak test method for FLD development. The first condition is that fracture must occur in the stretching region of the specimen and secondly that the driver must not fail before the test specimen. Both conditions are influenced by friction and distribution of strain between the punch and sheet materials as a result of the tooling geometry.

The first punch that was developed had a punch profile radius of 0.250 inch (Figure 3.3(a)). This punch resulted in all 4 inch, 5 inch and 7 inch width specimens failing catastrophically at the punch profile radius (Figure 3.18) or failure of the driver occurred prior to the test specimen (Figure 3.19).

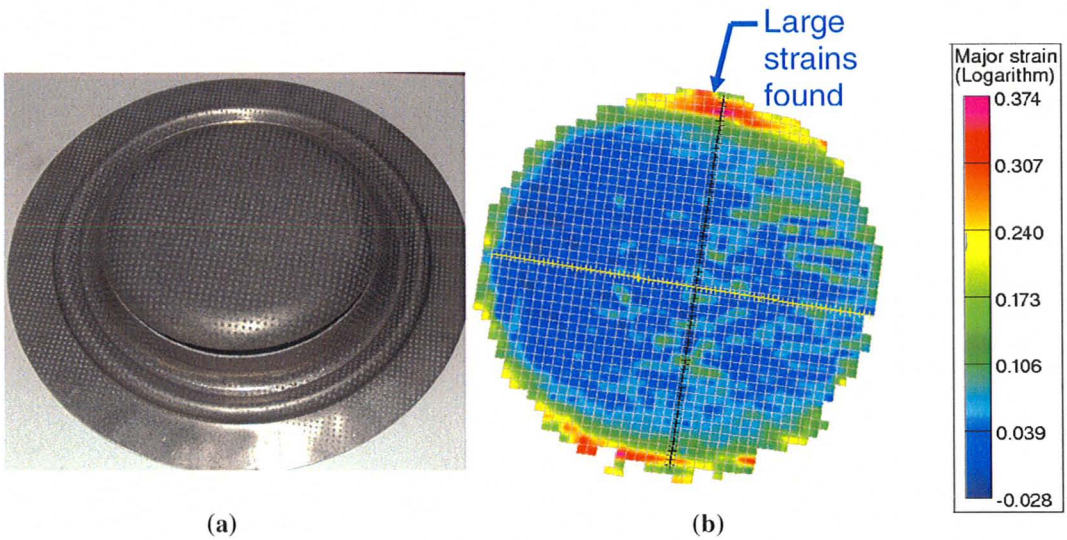

Figure 3.18: (a) Failure along punch profile and (b) strain distribution across 7 inch width specimen.

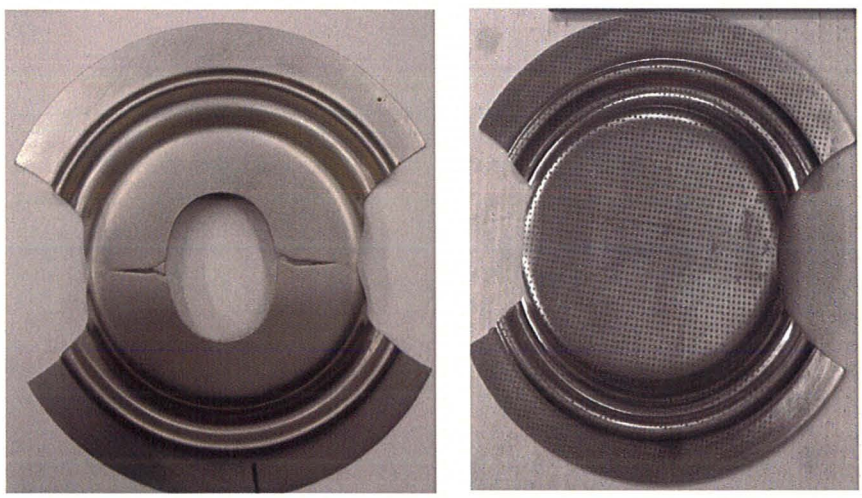

(a) 4 inch width driver **(b) 4 inch width test specimen**

Figure 3.19: Failure initiated by fracture in driver material prior to fracture in the test specimen.

From these conditions, it was determined that a second punch with a larger draw radius (0.500 inch) was needed. A larger draw radius reduced the friction conditions between the punch and the driver which allowed material to flow more freely over the punch profile. Fracture was ultimately achieved in the flat stretching region of the specimen by the proper deformation of the driver blank. An example of a successful 4 inch width test specimen can be seen in Figure 3.20.

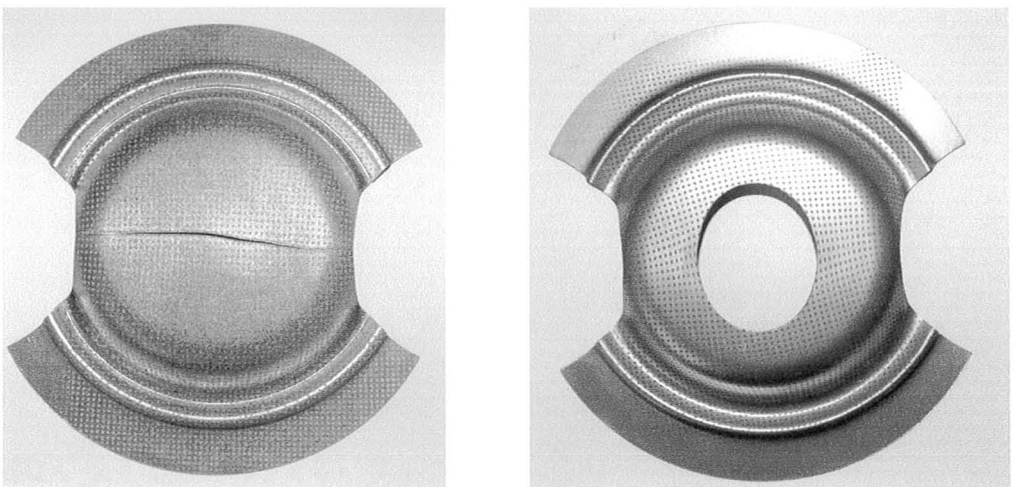

(a) 4 inch width test specimen **(b) 4 inch width driver**

Figure 3.20: Successfully test specimen fractured along the stretching region with no failure in the deformed driver blank.

3.6.3 Determination of the Driver Geometry

The last parameter to be investigated was the diameter of the driver hole for the 4 inch, 5 inch and 7 inch width specimens. For each specimen, a variety of hole diameters were tested according to the diameters used in previous works for aluminum alloys (Moore et al., 2002; Moshkar et al., 2003). To determine the optimal diameter for the driver hole, the forming limit for each test specimen was evaluated. The results can be seen in Figure 3.21 (DC material) and Figure 3.22 (CC material) for each strain path.

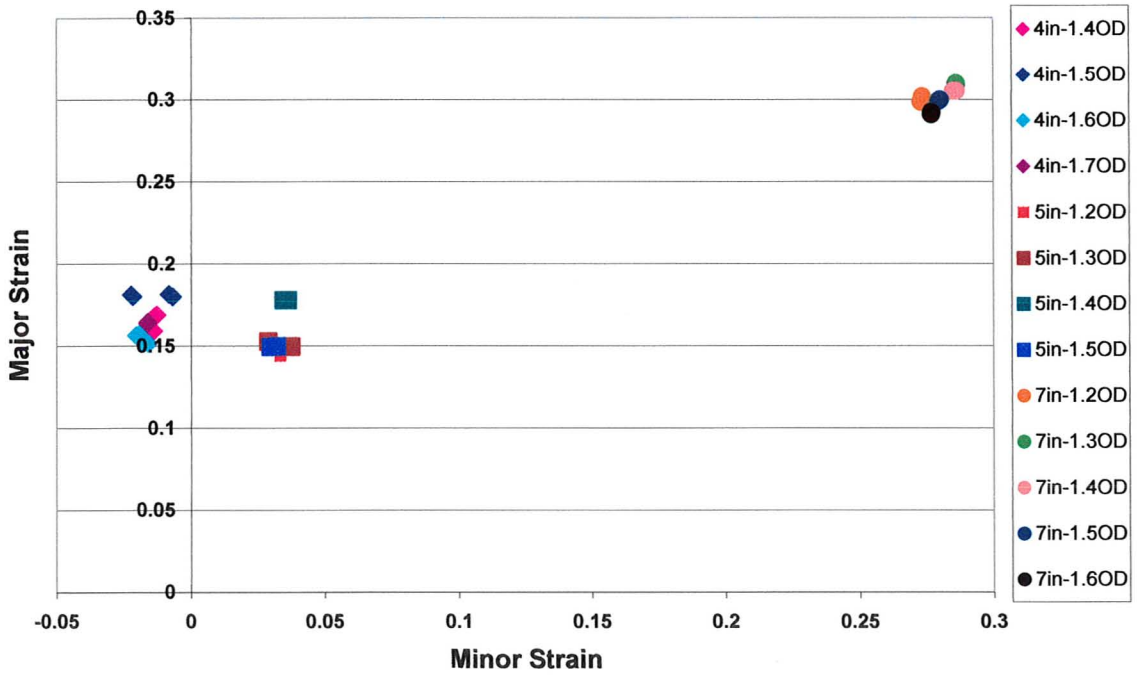

Figure 3.21: Forming limit results for 4 inch, 5 inch and 7inch width specimens for various washer geometries – DC material.

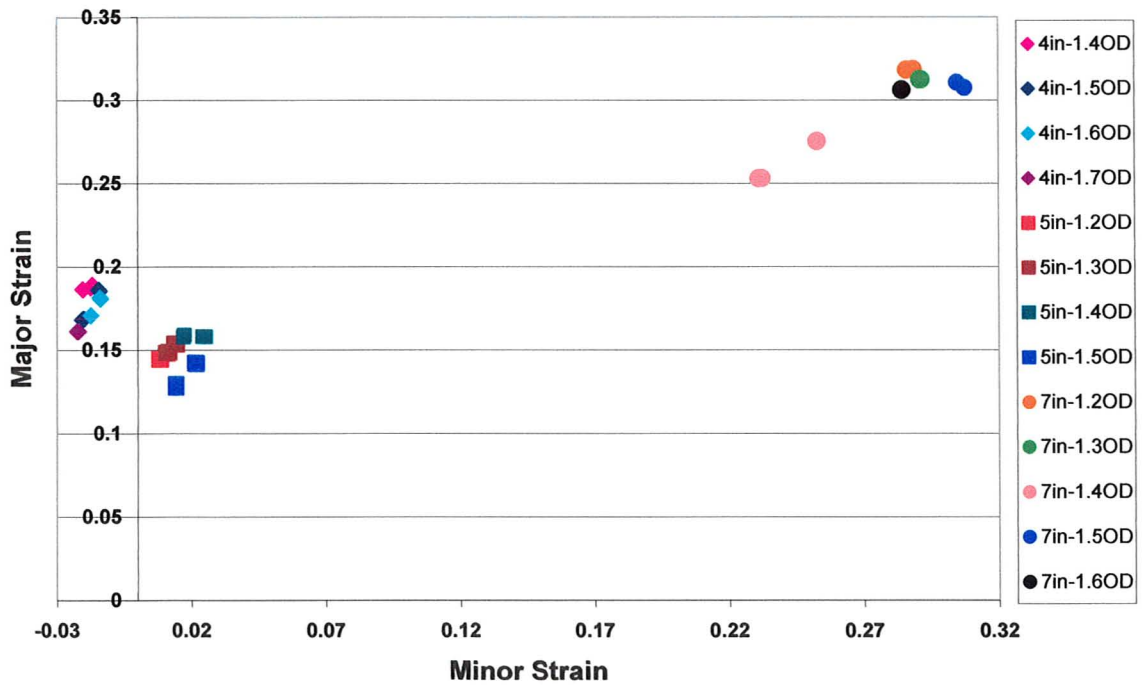

Figure 3.22: Forming limit results for 4 inch, 5 inch and 7inch width specimens for various washer geometries – CC material.

Comparing the results, the DC material showed more consistency in the performance of the drivers. It was clearly seen which hole diameter produced the best formability results. For the CC material though, specimens of the same geometrical width and hole diameter showed considerable scatter in the limit strain data. Therefore, the drivers that showed the highest and most consistent formability were chosen as the optimal hole diameter for testing. The optimal diameters of the driver hole for the 4 inch, 5 inch and 7 inch width specimens has been summarized in Table 3.3.

Table 3.3: Determined hole diameters for each specimen geometries

Material Type	*4 inch width geometry*	*5 inch width geometry*	*7 inch width geometry*
CC	1.4	1.4	1.2
DC	1.5	1.4	1.3

3.7 Forming Limits Evaluation

In order to assess the strains at the onset of localization, a graphical interpolation method presented by Bragard et al., (1972) was used. The strain distribution of a sheet specimen near fracture was examined. A plot of the strain profile of the surface elements showed a sharp inflection in the region of localized necking (or fracture). This indicates the surface elements outside the region of localization cease straining while elements located in the region of localization continue straining at a rapid rate until fracture occurs. To detect the onset of localization a polynomial curve was fitted. This method consisted of eliminating the points in the sharp inflection of the strain profile and fitting a curve to

the rest of the data. The peak value on the curve was chosen as the strain value at the onset of localization.

To determine the onset of localization for the specimens tested in this work, the major and minor strain distributions as line profiles, obtained from the ARGUS and ARAMIS systems, were plotted. From the strain profiles, the values on the curve which lie in the sharp inflection zone (localized neck or fracture zone) were omitted. This was done using the strain map of the specimen at localization (or fracture). Single point strain values were taken just outside the localized necking zone or in other regions of high strain such as shear bands which did not localize. These strain values were used as reference points. All strain values lying below them were considered safe from localization and all strain values greater were omitted from the strain profile.

A specimen strain map which was used to determine localization is shown in Figure 3.23. The major strain value lying just outside of the localized region is 0.163 or in a distant shear band which did not localized is 0.174. Using these strain values as reference, all values lying at and below 0.163 (or 0.174 in the shear band) on the strain profile (Figure 3.24) were considered safe from localization and all strain values above were omitted (values shown with open symbols). Using the strain values just prior to localization (values shown with closed symbols), a polynomial of the 4^{th} order was used to fit the data. The fitted curve represents a graphical interpolation of the true major and minor strains which provides strain values corresponding to the onset of necking. For the specimen shown in Figure 3.23 and Figure 3.24, the onset of localization was interpolated to be 0.182.

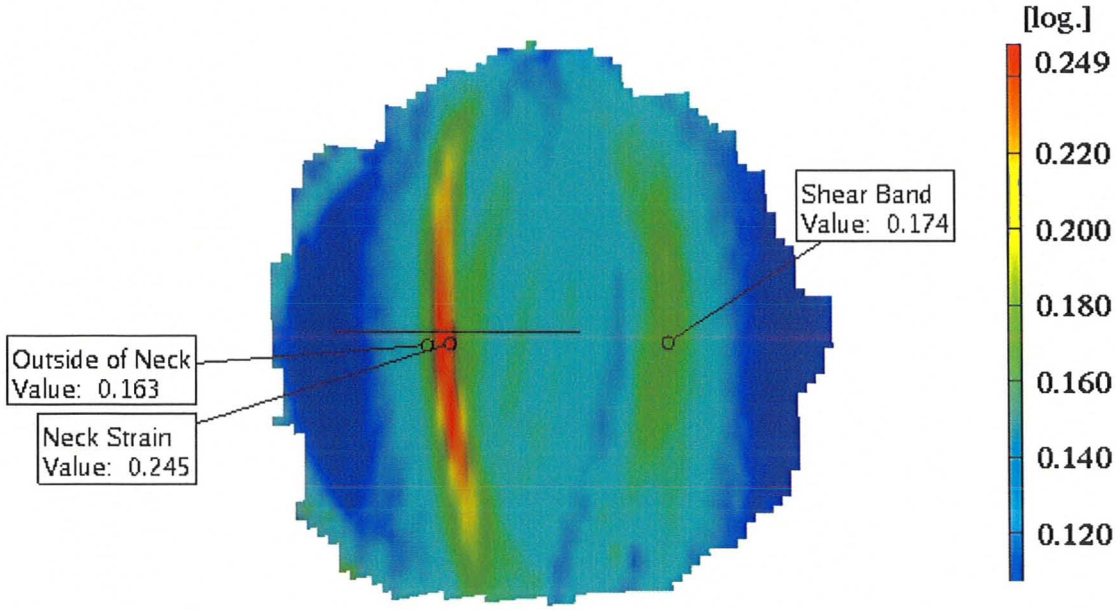

Figure 3.23: Strain map of 4 inch width specimen showing localization and prominent shear band.

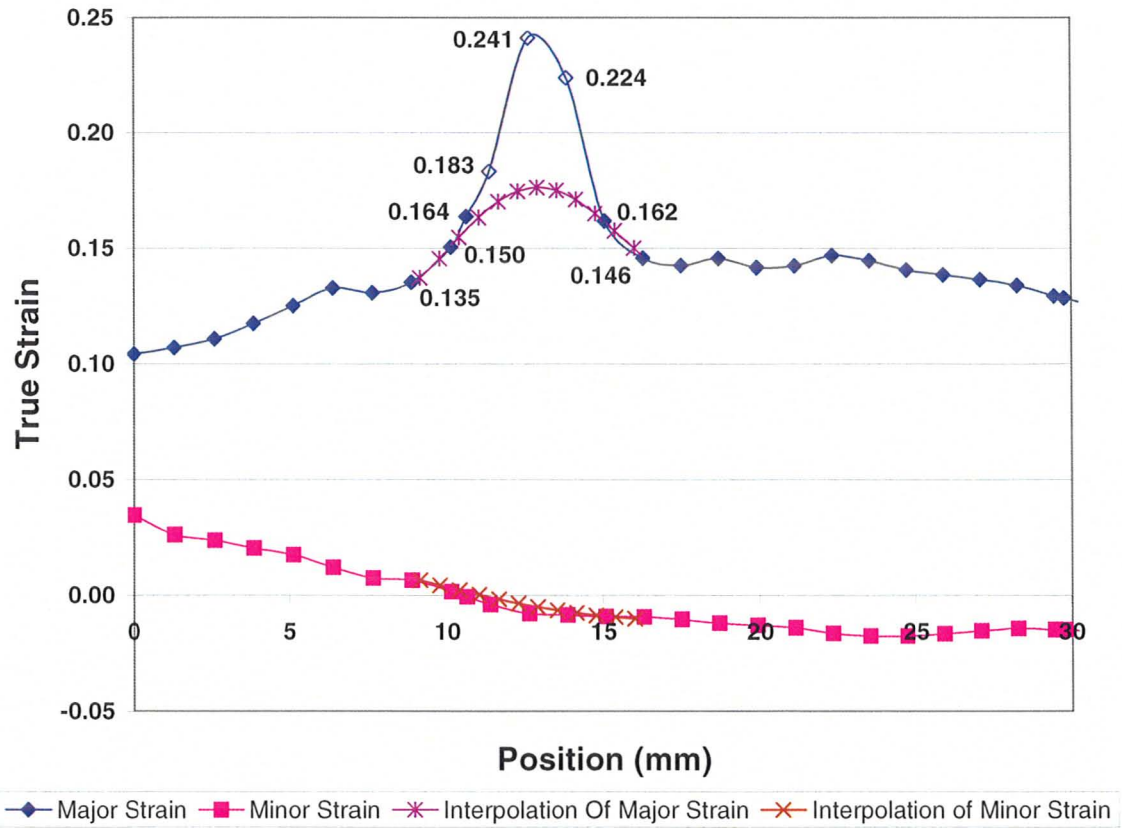

Figure 3.24: True major and minor strain plot showing 4th order polynomial interpolation.

To determine the appropriate polynomial fitting order, the various fitting curves were plotted against the original major strain curve. Considering the strain profile described above, the fitted curves can be seen in Figure 3.25 with the estimated forming limits shown in Table 3.4. A polynomial order of 2 or 3 resulted in a major strain values that were too low (0.174 was consider safe from localization) and a curve which did not agree well with the original data. A polynomial order of 4 or 5 yielded curves that were situated above the safe reference strain point of 0.174 but below the strain values found in the region of localization (0.183). The curve also fitted well with the strain profile data. A polynomial order greater than 5 resulted in major strain values larger than that found in the localized neck and therefore was not considered.

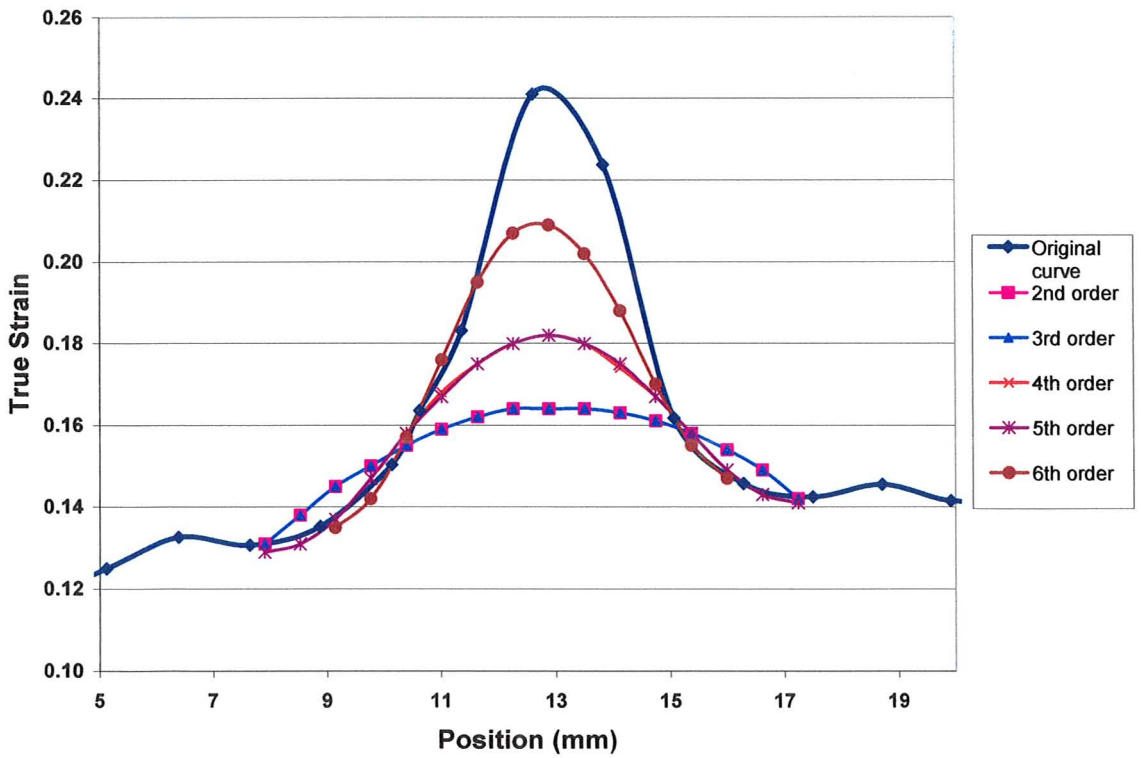

Figure 3.25: True major strain profile for specimen in Figure 3.23 and 3.24 showing the various fitted polynomial curves for forming limit evaluation.

Table 3.4: Effect of polynomial fitting order on forming limits evaluation using the Bragard criterion

Polynomial Fitting Order	*Major Strain*	*Minor Strain*
2	0.164	-0.005
3	0.164	-0.005
4	0.182	-0.005
5	0.182	-0.005
6	0.210	-0.01

The influence of facet size on forming limit evaluation was also explored. The strain profile across one specimen which was computed using three different facet sizes is shown in Figure 3.26. Upon looking at the graph, the most noticeable difference in using various facet sizes is the strain value estimated at localization (or fracture). The smaller the facet size the higher the strain value found.

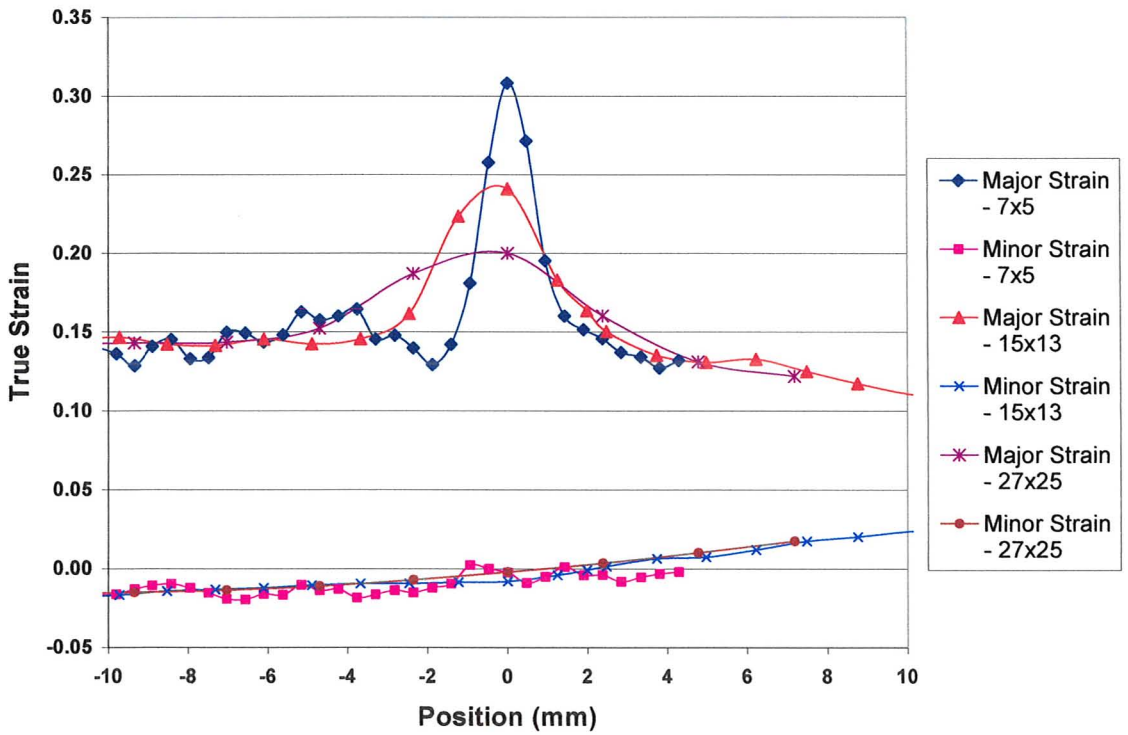

Figure 3.26: True major and minor strain plot showing 4th order polynomial interpolation.

In terms of determining the forming limits, this has little effect since these values are omitted in the estimation. It can also be seen that the amount of scatter in the data is higher for a smaller facet size (7x5) which makes fitting a parabola to the data for forming limit elevation rather difficult. In addition, a facet size that is too large such as 27x25, gives very little data in the region near the neck for analysis. For these reasons, a 15x13 facet size was selected to obtain smoother strain profiles which provide enough information near the neck for analysis. The forming limits were evaluated for the curves given in Figure 3.26 and can be seen in Table 3.5. The facet size has relatively little influence on the determination of major and minor strain values estimated by the Bragard method and a 4^{th} order polynomial fit.

Table 3.5: Effect of facet size of forming limits evaluation using the Bragard criterion

Facet Size	*Major Strain*	*Minor Strain*
7 x 5	0.171	-0.009
15 x 13	0.176	-0.005
27 x 25	0.178	-0.004

3.8 Metallography

3.8.1 Specimen Preparation

All specimens chosen for observation of shear bands and fracture analysis were sectioned along the centre line of the RD-LT plane using a low speed diamond saw to reveal the through-thickness direction (Figure 3.27). For specimens which were fractured completely (left-hand side strain path geometries) the two halves were first aligned and then sectioned to obtain corresponding fracture surfaces. For the 7 inch specimen width,

fractured sections were taken perpendicular to the fractured surface due to their fracture profile (Figure 3.27(c)).

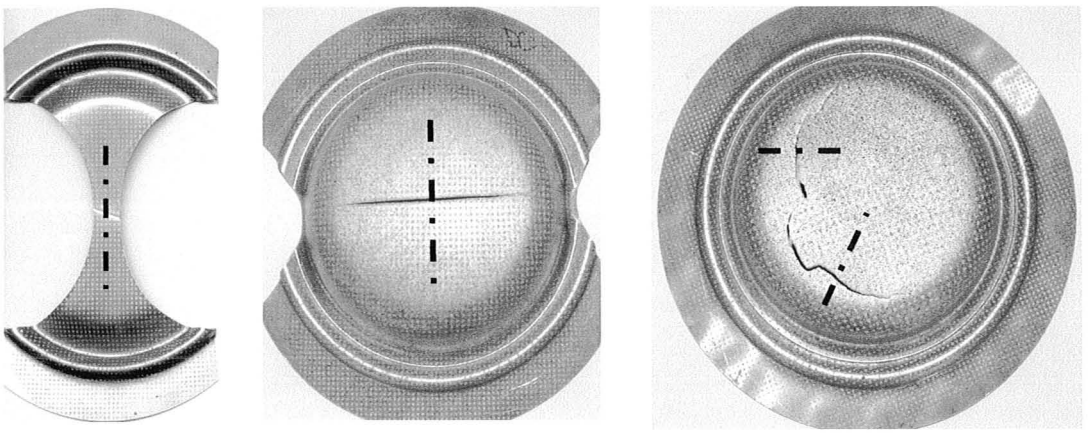

(a) 0.5 inch width (b) 5 inch geometry (c) 7 inch geometry

Figure 3.27: Various specimen width geometries showing sectioning for fracture strain measurements.

All specimens were mounted in epoxy resin, ground and polished to a mirror finish using the Struers Roto automatic polisher. The grinding and polishing sequence is shown in Table 3.6.

Table 3.6: Grinding and Polishing Sequence for AA5754

Step	*Surface*	*Suspension/Lubricant*	*Load (N)*	*Time (min)*
1	1200 SiC paper	water	10	1
2	2400 Sic paper	water	10	1
3	4000 SiC paper	water	15	1
4	MD-Dac	15μm natural diamond slurry and blue lubricant	20	4
5	MD-Rondo	3μm natural diamond slurry and blue lubricant	20	4
6	MD-Nap	1μm natural diamond slurry and blue lubricant	20	4
7	MD-Chem	0.05μm colloidal silica and water	15	4

3.8.2 Heat Treatment and Etching for Shear Bands

All specimens after sectioning and mounting were heat treated to delineate bands of intense shear. A heat treatment of 14 days at 100°C was utilized to diffuse precipitates of Al-Mg inter-metallics into intense deformation regions (Spencer, 2000). The microstructure was revealed by etching with a 40% Phosphoric acid (H_3PO_4) etching solution heated to 45°C and held for 1.5 minute on the polished specimen surface. A typical optical micrograph showing a pair of intersecting macroscopic shear bands is shown in Figure 3.28. The shear bands were revealed through the use of Nomarski Differential Interference (or NDI) contrast (Lang, 1977) using an optical microscope.

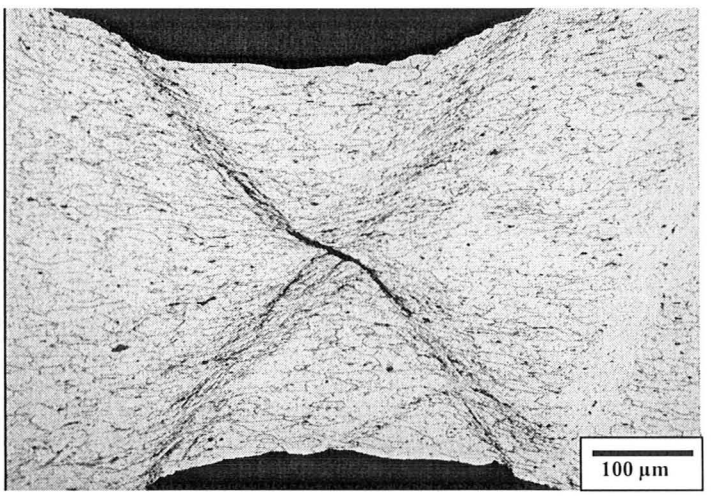

Figure 3.28: Revealed through thickness showing shear bands from heat treatment and etching technique on necked specimen using NDI contrast.

3.9 Fracture Strain Measurements

Fracture strain measurements were taken from both sides of the fractured surface after specimens were sectioned, mounted and polished. Each fracture pair was imaged using a digital camera mounted to an optical microscope under low magnification. An

image editing program (Adobe Phototshop) was used to align the two fractured surfaces. The minimum cross-sectional thickness was then measured by importing the modified image into the image analysis program, UTHSCSA Image Tool (Figure 3.29).

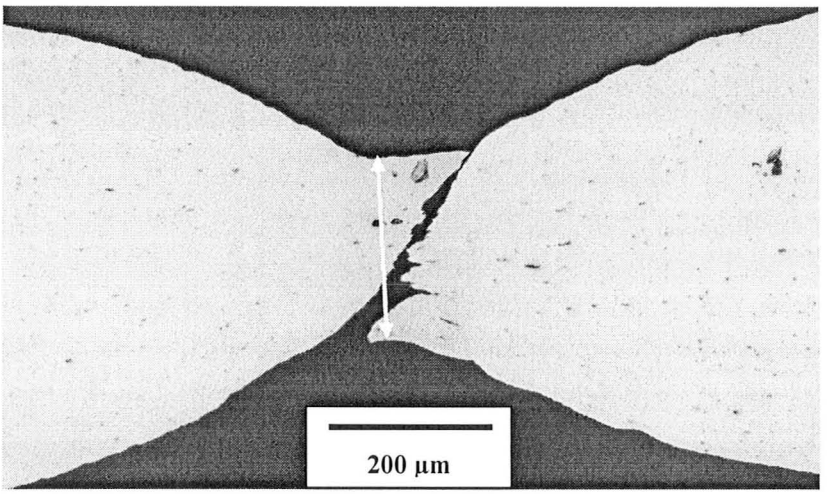

Figure 3.29: Modified image of aligned fractured halves for minimum cross-sectional thickness measurements.

From this, the true thickness strain was determined using the following equation,

$$\varepsilon_3 = \ln\left[\frac{t_m}{t_0}\right] \tag{3.1}$$

where t_o is the original sheet thickness and t_m is the measured minimum cross-sectional thickness. The fracture strain for all specimens can be calculated by making the assumption of volume constancy, i.e.

$$\varepsilon_1 + \varepsilon_2 + \varepsilon_3 = 0 \tag{3.2}$$

where ε_1, ε_2 represent the two principal surface strains and ε_3 represents the strain in the thickness direction. Knowing the thickness strain ε_3 and determining the minor ε_2 from the ARAMIS system, the major principal strain ε_1 was determined using Eqn.3.2.

The fracture surface contour of ductile materials can be highly irregular due to void growth and coalescence, which can introduce a large degree of error into the thickness strain (ε_3) measurement. When a material cavitates, the laws of plasticity which are based on the assumption of volume constancy, cease to apply. Therefore, the thickness strain becomes overestimated and the fracture strain (ε_1) is underestimated. In the case of regular sheet materials, the volume change due to void-nucleating particles is expected to be small (less than a few percent), but undoubtedly should not be ignored.

In an attempt to minimize the scatter in the fracture strain measurements provided in the current study, all samples were sectioned in the same manner along the centre line of the RD-LT plane. The thickness strain was evaluated as the average of many measurements along the aligned fractured halves. As a result, the source of error associated with the minimum cross-sectional thickness measurements introduces an uncertainty of $\pm$ 0.05 in ε_3. Specimens which represented the average fracture strain and fracture mechanism observed for each material and geometry were chosen for analysis of the fracture behaviour.

Chapter 4
Experimental Results

The following chapter presents the results obtained in the present work. It is divided into four main sections. The first section examines the materials characteristics in terms of microstructure and standard mechanical properties. The next section assesses the forming limits of the materials using the in-plane testing technique. The third section addresses the deformation behaviour of the sheet materials as a function specimen geometry using DIC analyzes methods. The final section focuses on the failure behaviour of the materials using optical microscopy techniques.

4.1 Material Characteristics and Mechanical Properties

4.1.1 Optical Metallography

Optical metallurgy of the sheet materials was performed in the as-received state prior to any testing. As mentioned in Chapter 3, the as-received materials were cold rolled to a 1 mm gauge thickness and annealed at 450°C for 2 hours to achieve the O-temper state. The microstructures of the CC and DC materials were examined in the rolling, transverse and normal directions. The average grain size for each material can be seen in the micrographs in Figure 4.1. Upon observation, the grains appear to be equiaxed with the average DC material grain size being slightly larger than the CC material.

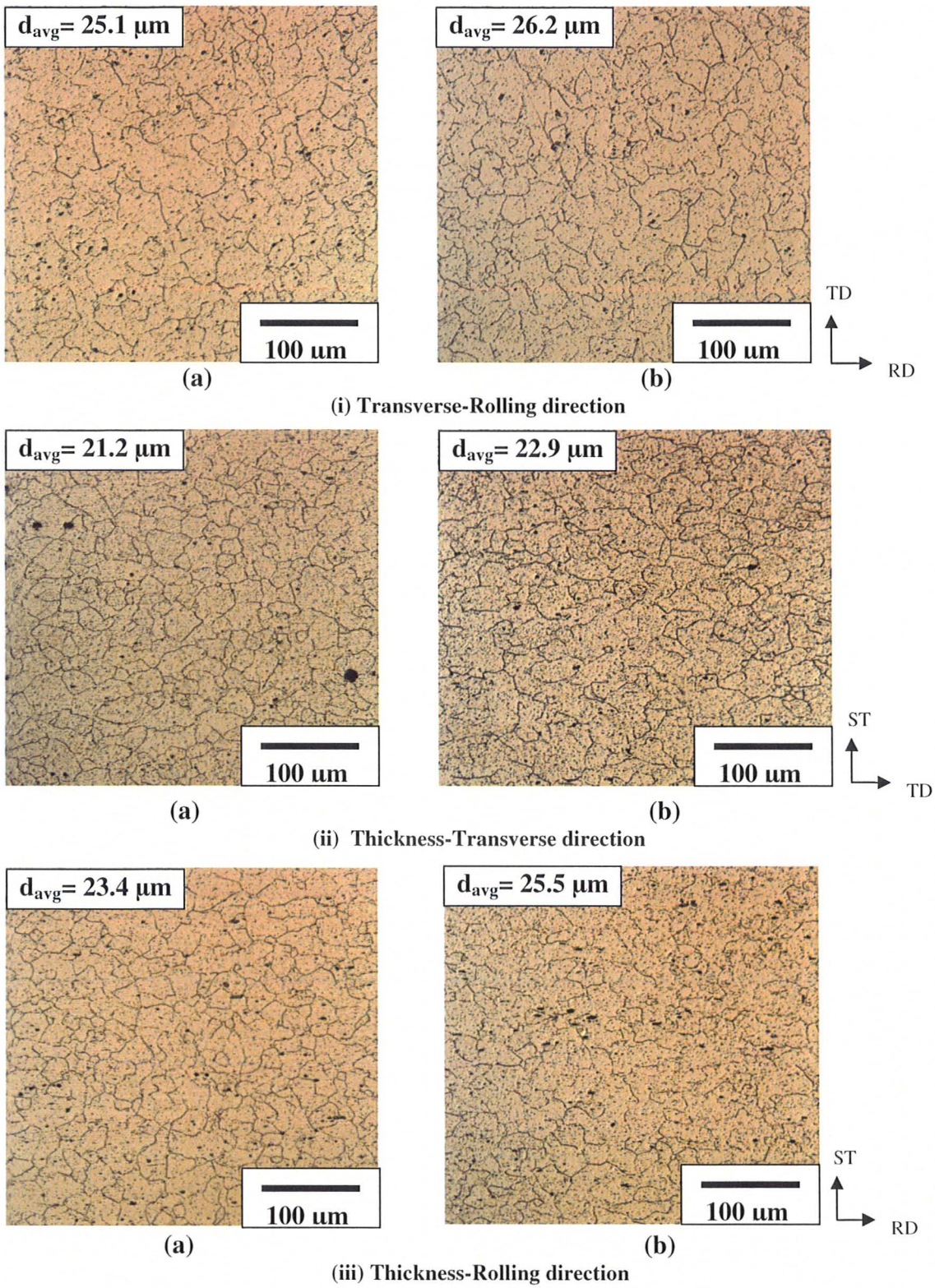

Figure 4.1: Microstructure and grain sizes for (a) CC5754 and (b) DC5754.

4.1.2 Uniaxial Tensile Test of Standard Sheet Samples

Samples of CC and DC as-received sheet material were tested in uniaxial tension in the rolling direction. The tensile properties for each material, displayed in Table 4.1, were obtained by plotting the true stress vs. true strain curves, shown in Figure 4.2.

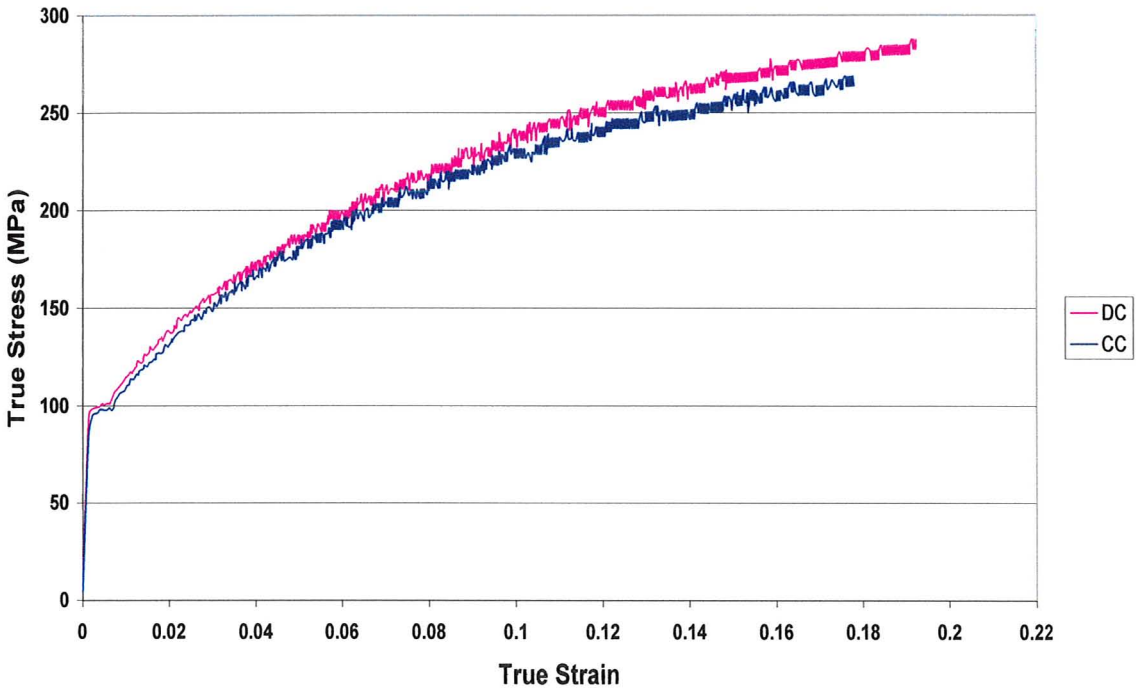

Figure 4.2: True stress-strain curves for CC and DC5754 – Rolling direction.

The tensile responses of both materials were quite similar. Both materials exhibited discontinuous yielding as shown by the serrations in the tensile curve. This is associated with the Portevin-Le Chatelier (PLC) effect observed in Al-Mg alloys. In both materials, serrations on the curves were classified as type B bands which are associated with an applied strain rate of 10^{-4} /s (Lebyodkin et al., 1996). The serrations begin immediately upon the completion of the Lüder strain and reach amplitudes of ±4 MPa for DC and ±5 MPa for CC.

Table 4.1: Tensile properties for CC and DC 5754

Material Type	*Uniform Strain*	*True 0.2% Offset Yield Strength (MPa)*	*True Ultimate Tensile Strength (MPa)*	*Strain Hardening Exponent, n*
CC	0.178	95	263	0.310
DC	0.192	99	288	0.319

According to Table 4.1, the DC material exhibits higher yield and ultimate tensile strengths in comparison to CC material. The amount of uniform strain varies between the two materials, with the DC material exhibiting a slightly higher uniform strain. It is important to note that both materials fail well below the strain expected from the Considère criterion using the Hollomon equation.

4.1.3 Fracture Behaviour of Uniaxial Tensile Test Samples

The fracture behaviour of the tensile samples was investigated. The samples were prepared according to Chapter 3 (Section 3.7) to reveal the fracture of the samples. The optical micrographs (Figure 4.3 and 4.4) show that the fracture mechanisms of the two materials are different. Before the initiation of fracture, both materials reveal the formation of a pair of intense conjugate shear bands inside the neck region. For the CC material, the smooth angled fracture profile (53° to the tensile axis) indicates that failure initiates along only one shear system which is characteristic of the void sheeting fracture mechanism. For the DC material, fracture occurs along two shear systems resulting in a "V" shaped profile. This type of failure is characteristic of the double-cup fracture mechanism which results from the formation of a central void at the intersection of the conjugate shear bands.

The fracture behaviour of the two materials was also examined in terms of the amount of total ductility shown prior to fracture. The CC material shows a lower total ductility in comparison to the DC material, as given by the thickness reduction measurements (t_m) or fracture strain. Using the method described in Chapter 3 (Section 3.8), the fracture strain of DC and CC materials were obtained as 1.43 and 1.31 respectively.

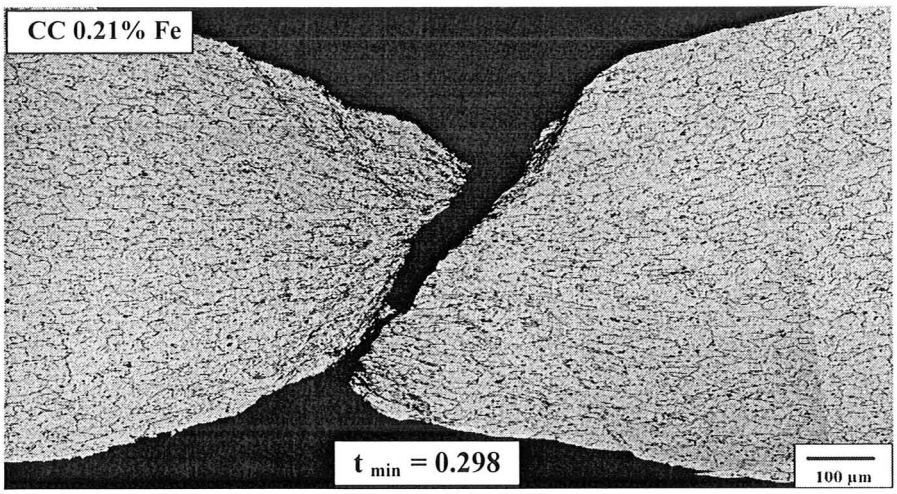

Figure 4.3: Through-thickness sections of CC tensile sample showing shear localization failure and shear band formation.

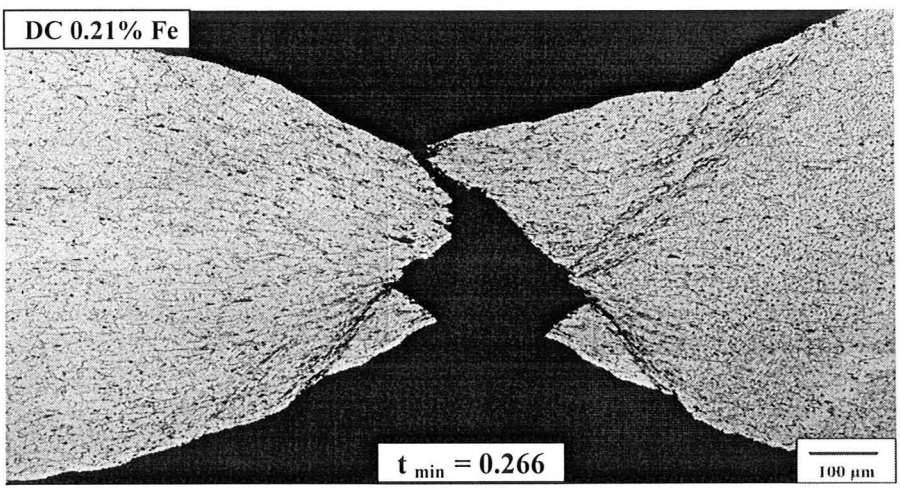

Figure 4.4: Through-thickness sections of DC tensile sample showing double-cup failure and shear band formation.

4.2 Evaluation of Forming Limits

4.2.1 Load versus Displacement Data

Punch load and displacement data were recorded for all test specimens as a function of time. All testing was performed at a speed of 0.01 inches per second (15 mm/min) with a data acquisition rate of 5 data points per second. A comparison of the punch load versus punch displacement curves for the specimen geometries can be seen in Figure 4.5 and Figure 4.6 for the two materials. The profile of the curves is such that the loading rate shows a gradual increase to a peak, represented by an inflection point in the curve. After the inflection point, the loading rate decreases to a saturation point at maximum load which is characteristic of the onset of localized necking. The load then quickly drops off until fracture is reached. The maximum load and maximum punch displacement for each material under each strain path is summarized in Table 4.2. Higher punch loads were reached for all DC specimen geometries which is consistent with the results found from the uniaxial tensile test sample. The higher load reflects the higher yield strength and ultimate tensile strength in comparison to CC5754. In terms of punch displacement, the two materials show similar results with the CC material reaching a slightly larger value. The appearance of PLC bands is associated with abrupt drops in load, as shown by the serrations on the uniaxial tensile curves (Figure 4.2). Due to the lower data acquisition rate, limited by the software and the relatively large load cell (50,000 lbs or 222,411 N) of the forming press, the curves were unable to reveal the presence of PLC bands.

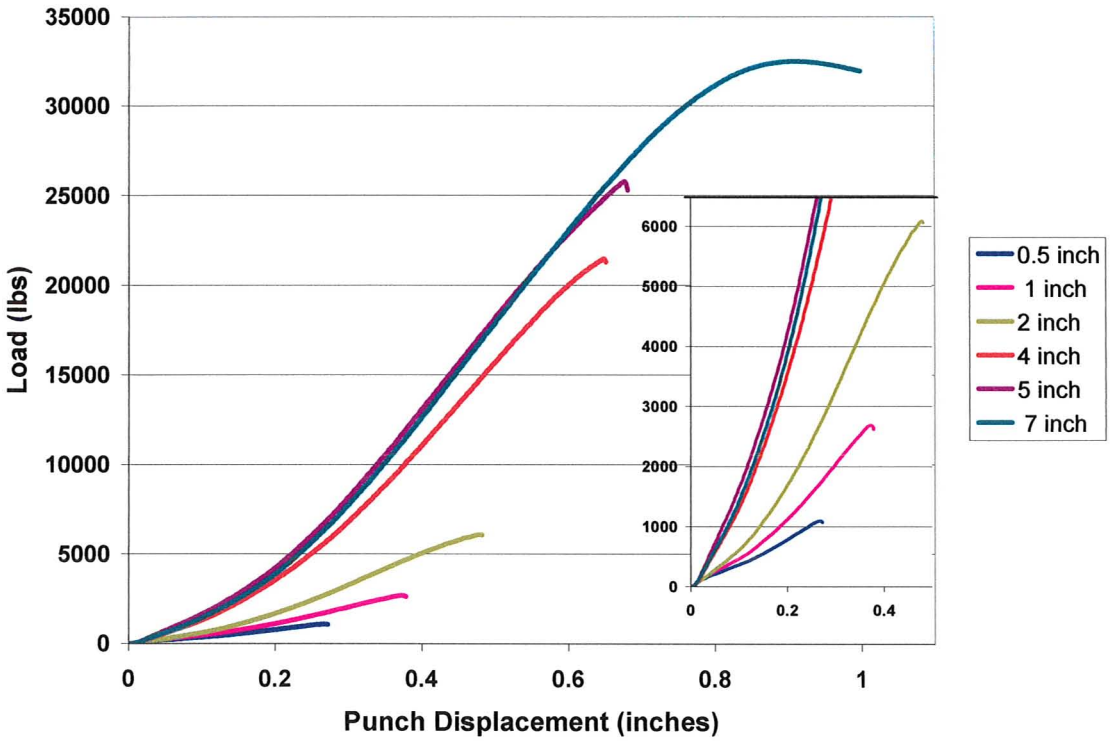

Figure 4.5: Punch load versus punch displacement data for CC5754.

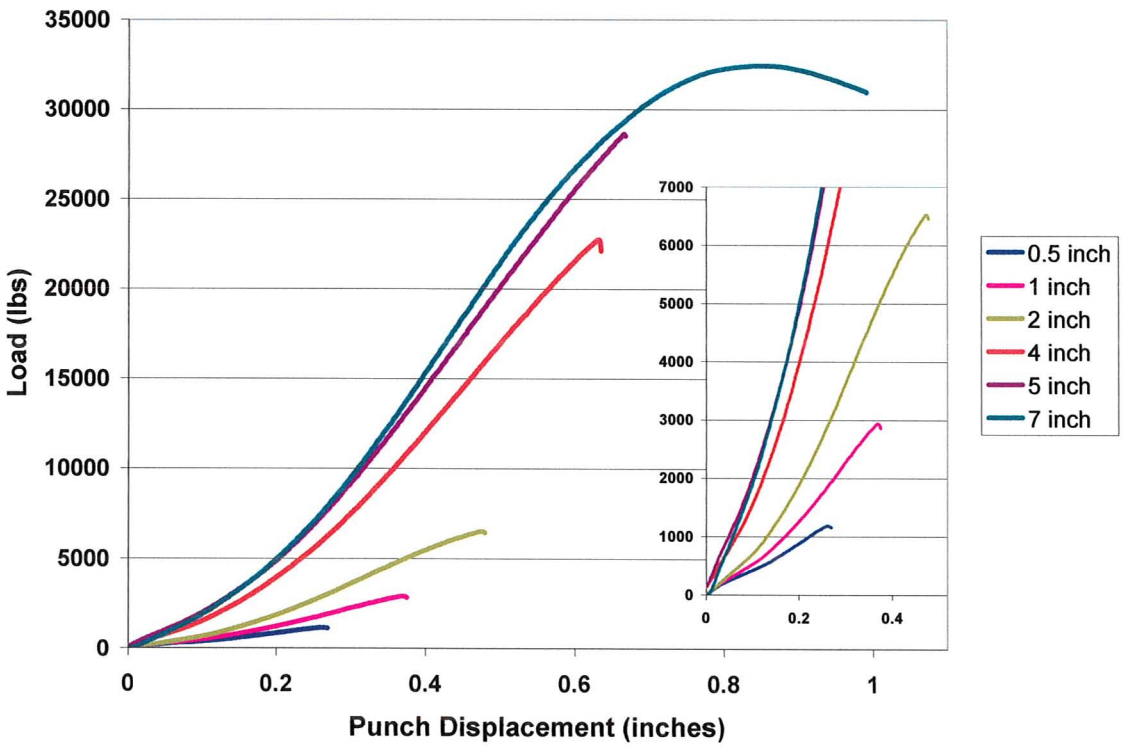

Figure 4.6: Punch load versus punch displacement data for DC5754.

Table 4.2: Maximum punch load and punch displacement data for CC5754 specimens

Material	*Punch*	*0.5 inch*	*1 inch*	*2 inch*	*4 inch*	*5 inch*	*7 inch*
CC	*Load (lbs)*	1094	2686	6068	21,458	25,782	32,460
	Displacement (inches)	0.269	0.378	0.482	0.651	0.674	0.998
DC	*Load (lbs)*	1183	2935	6526	22,757	28,632	32,480
	Displacement (inches)	0.262	0.375	0.479	0.639	0.668	0.991

4.2.2 Forming Limit Diagram

The evaluation of the forming limits was completed following the methodology described in Chapter 3 (Section 3.6), which can be seen in Appendix A. This involved using the graphical interpolation method presented by Bragard et al. (1972). The onset of localization was determined using the major and minor strain distributions as line profiles, obtained from the ARAMIS systems. From the strain profiles, a polynomial of the 4^{th} order was used to fit the data. The values prior to and after localization can be seen in the figures in Appendix A, along with the interpolated major strain value corresponding to the forming limit.

The in-plane forming limit curves for CC5754 and DC5754 can be seen in Figure 4.7. It is apparent from the results that the forming limits of the two materials are very similar. The DC material shows a slightly higher forming limit on the LHS in comparison to the CC material (approximately 3 pct) while nearly identical results can be seen under balanced biaxial tension (less than 1 pct). The RHS of the FLD though, shows

a very limited amount of information. It appears the testing technique was unable to generate more strain paths on the extreme RHS of the FLD. For this reason, forming limit curves on the RHS were approximated by a straight line.

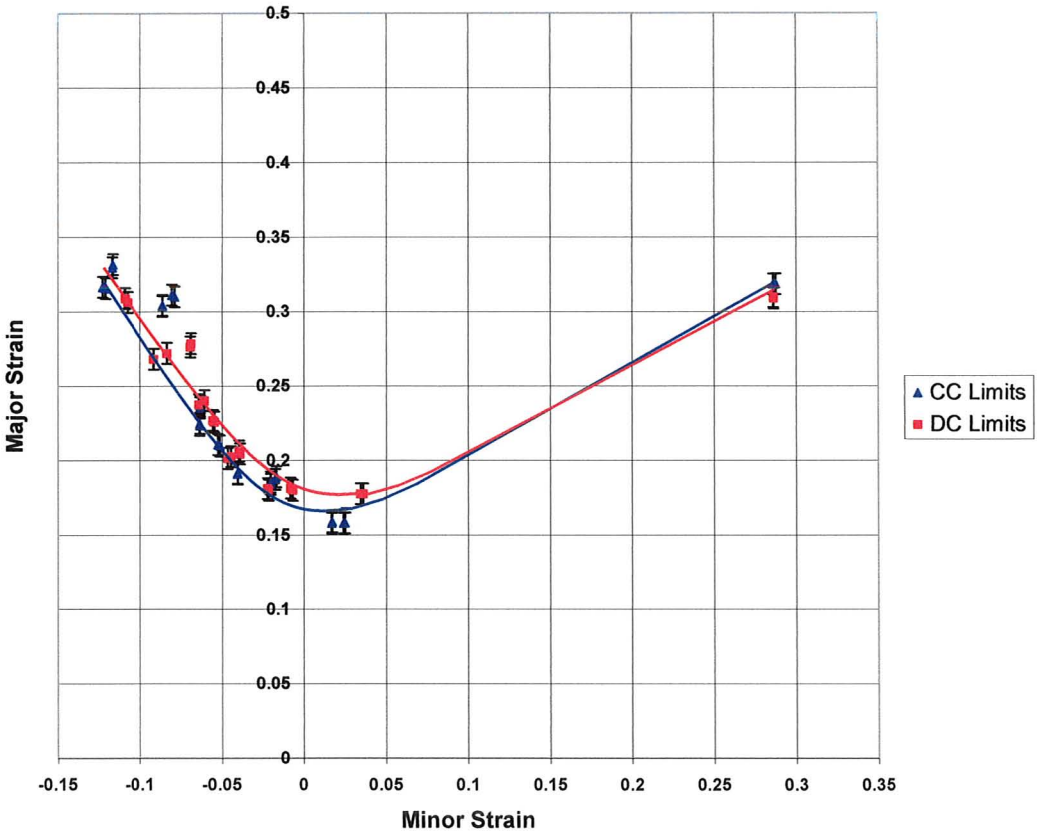

Figure 4.7: In-plane forming limit curve for CC5754 and DC5754 material.

4.3 Examination of Material Deformation Behaviour

Observations of material strain distribution during deformation and failure were carried out using DIC. The results are shown in two sections, left-hand side (LHS) and right-hand side (RHS) specimen geometries. An image recording rate of one image per second was used to capture the deformation process and all testing was performed at room temperature with a strain rate of 3×10^{-3} s^{-1}.

4.3.1 Specimen Geometries for Left-Hand Side of FLD

(i) Strain Distribution Observations

DIC results from the observed strain map sequences show the formation and propagation of PLC bands in both materials for the 0.5 inch, 1 inch and 2 inch width specimen geometries. The deformation bands were characterized as type B PLC bands. This type of deformation behaviour is associated with a discontinuous but correlated propagation of the deformation bands, referred to as hopping bands and is characteristic at strain rates between 10^{-4} to 10^{-3} s^{-1} (Casarotto et al., 2005). The PLC bands were nucleated at both ends of the test specimen and traveled across the specimen gauge length in the tensile direction (Figure 4.8).

PLC bands are characterized by specific spatial features. The band inclination angle is one of these features. According to the results, the PLC bands were inclined to the specimen axis at well-defined angles, which did not change significantly throughout the deformation process. The angles were measure from the strain map results using the image analysis program UTHSCSA Image Tool. According to the measurements, the inclination angle of the PLC bands increased as the specimen's width increased and the DC material revealed a slightly larger angle than the CC material. All results are as displayed in Table 4.3.

Table 4.3: Inclination angle of the deformation bands with respect to the tensile axis

Material	*0.5 inch*	*1 inch*	*2 inch*
CC	59°	62°	67°
DC	62°	64°	65°

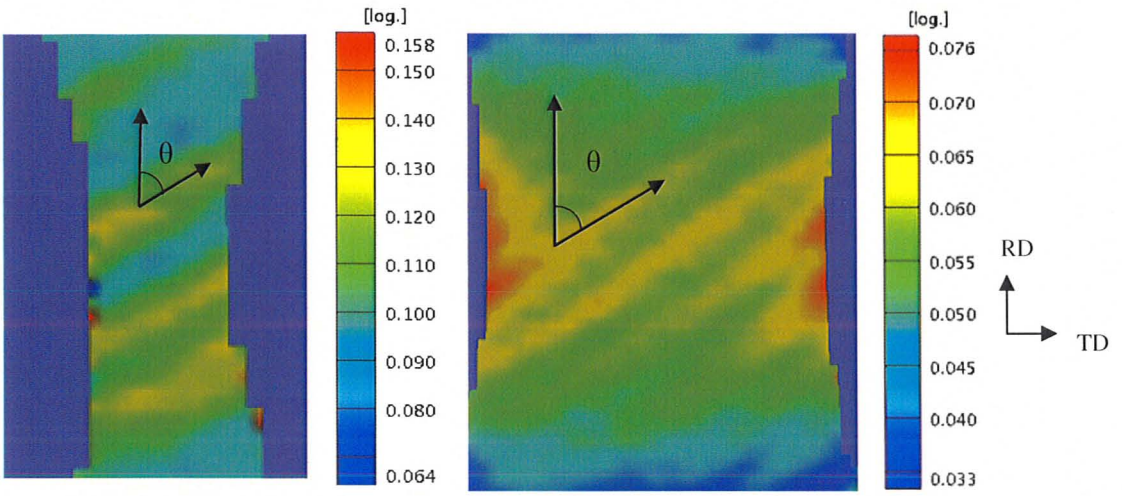

Figure 4.8: Strain maps for 0.5 inch (θ=59-62°) and 2 inch (θ=65-67°) specimens showing type B PLC band deformation behaviour and band inclination angles.

Another PLC band spatial feature observed during deformation is the formation of symmetrical bands of equal inclination but opposite direction where bifurcation from one direction to the other occurs (Chihab et al., 1987). An example of this is illustrated in Figure 4.9 for a 0.5 inch width specimen. At the start of deformation, PLC bands nucleate and propagate along the specimen gauge length at well-defined angles and directions, shown by band A. As deformation continues, symmetrical bands then form of equal inclination but opposite direction, represented by band B. As straining continues, both symmetrical bands propagate along the specimen's gauge length. For the materials tested in this study, the strain at which symmetrical band formation was observed varied with the specimen geometries. These results are displayed in Table 4.4, which gives the true global strain at symmetrical band formation as a function of the material and specimen geometry.

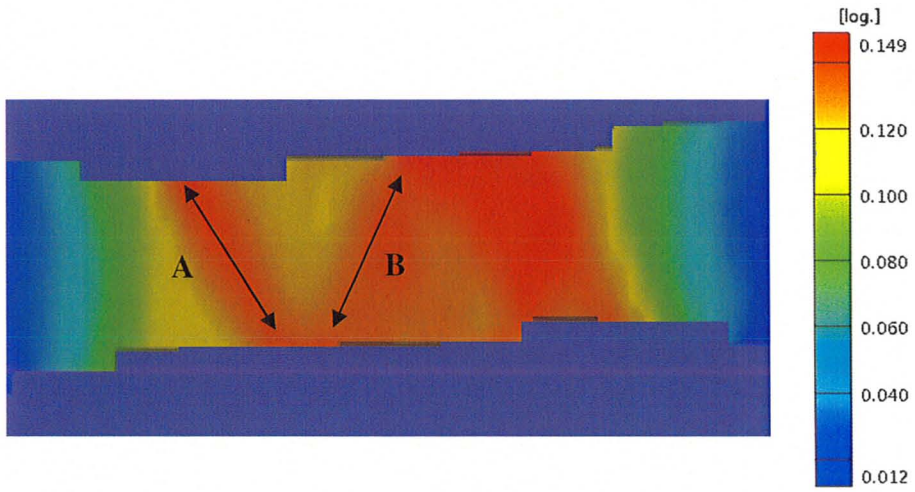

Figure 4.9: Strain map showing symmetrical PLC bands propagating along specimen gauge length.

According to the results, as the specimen's geometrical width increases and the strain path shifts towards plane strain conditions, the strain at which symmetrical band formation was observed was delayed. For the 2 inch width specimen, the direction of band propagation remained fixed throughout most of the deformation process and only when the specimen was nearing strain localization was a symmetrical band observed. In addition, the CC material consistently showed a lower global strain at which symmetrical band alteration occurred.

Table 4.4: True global strain at symmetrical band formation for CC and DC material

Material	*0.5 inch*	*1 inch*	*2 inch*
CC	0.082	0.113	0.141
DC	0.092	0.120	0.145

Direct surface observations were also used to determine the PLC deformation behaviour. Previous works by various authors (Li et al., 1998; Casarotto et al., 2005) show that surface markings in the form of regularly spaced parallel bands are seen by

materials that exhibit type B PLC bands. An example of the surface markings observed in the present work is shown in Figure 4.10 and Appendix B. The majority of the deformation bands are aligned in one direction which is consistent with the direction of PLC movement observed by the ARAMIS system. A limited number of symmetrical bands are seen which developed just prior to specimen failure. It is important to note that at the intersection of the symmetrical bands located in the center of the specimen, strain localization has been initiated.

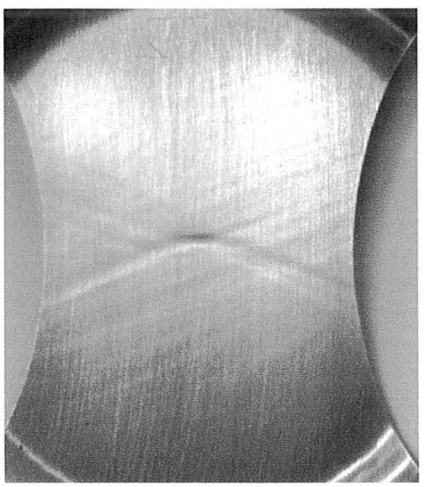

Figure 4.10: CC5754-2 inch width test specimen showing characteristic surface marking associated with PLC deformation bands.

(ii) Local Strain as a Function of Global Strain

Further processing of the specimen strain maps was performed to observe the local true strain as a function of the overall global true strain in order to determine the PLC band strain for each material and specimen geometry. The PLC band strain was defined as the difference in strain value between the local and global strain. The PLC band strain as a function of specimen geometry and material can be seen in Figure 4.11 to

Figure 4.13 where the values were obtained according to Chapter 3 (Section 3.5.3). The straight line on the plots represents homogenous plastic deformation where the local true strain equals the global true strain. As deformation proceeds, the local strain deviates from the global strain linearly indicating deformation involving PLC banding. In addition, the band strain reaches a maximum before strain localization, indicated by the rapid increase in slope of the curve. The results of the plots show that the band strain increases linearly with the global strain for both materials and as the specimen's geometrical width increases, the maximum amount of strain carried in the PLC bands decreases. These results are listed in Table 4. 5, where the maximum strain carried in the PLC bands were estimated according to the procedure given in Chapter 3 (Section 3.5.3).

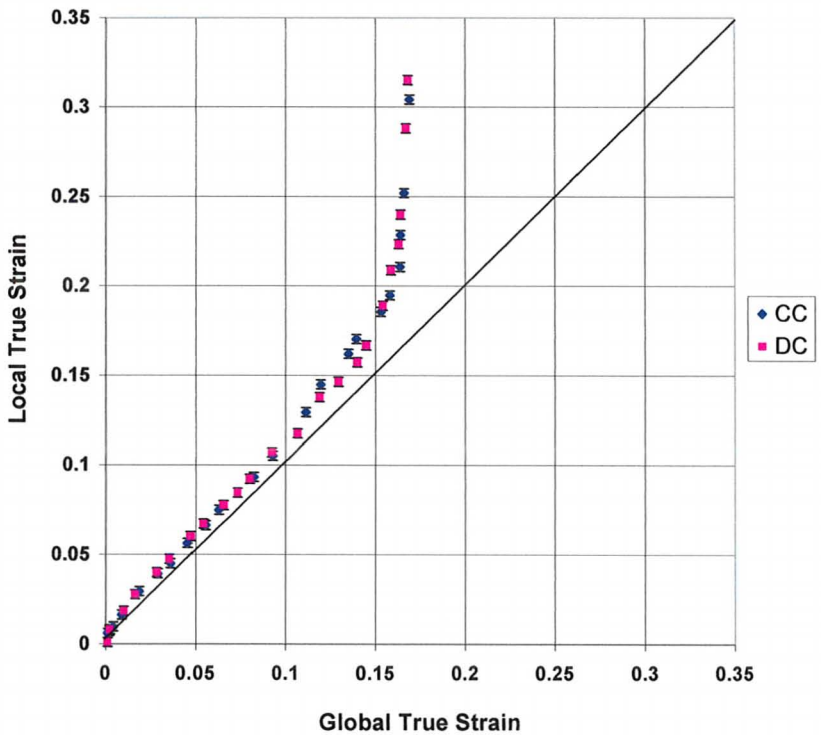

Figure 4.11: Plot of local true strain in deformation bands as function of global true strain for 0.5 inch width geometry.

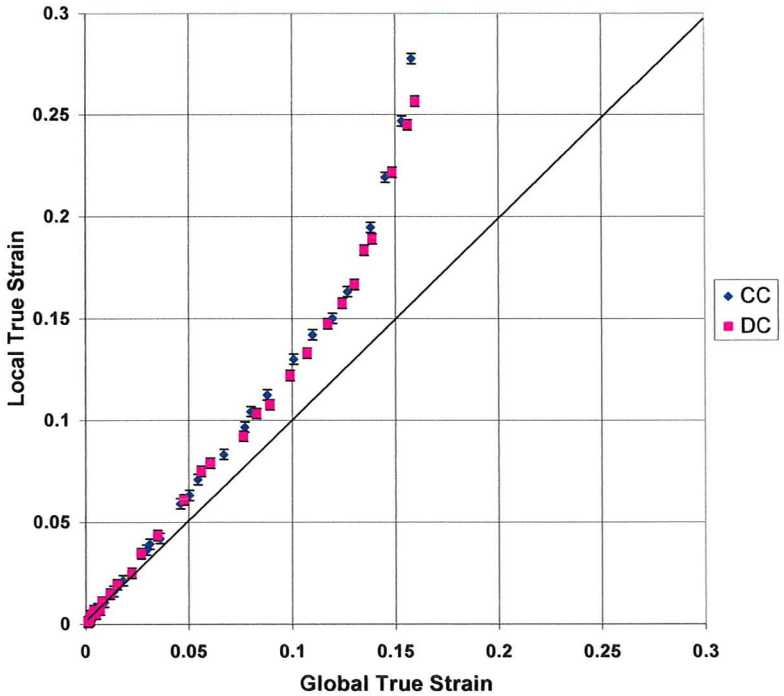

Figure 4.12: Plot of local true strain in deformation bands as function of global true strain for 1 inch width geometry.

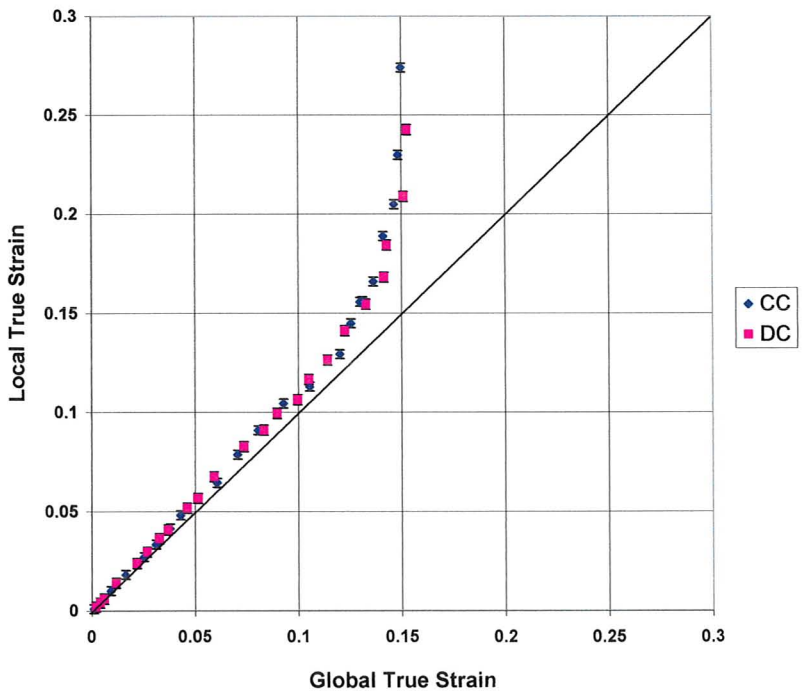

Figure 4.13: Plot of local true strain in deformation bands as function of global true strain for 2 inch width geometry.

Table 4. 5: Maximum strain carried in PLC bands according to the local and global true strain plots

Material	*0.5 inch*	*1 inch*	*2 inch*
CC	0.0325	0.0305	0.021
DC	0.0309	0.0302	0.022

Before the onset of serrated flow can begin, an incubation period consisting of homogenous plastic flow must be reached, referred to as the incubation strain, ε_c. Once the incubation strain is reached, deformation involving PLC bands begins. From the local true strain versus global true strain plots shown in Figure 4.11 to Figure 4.13, ε_c was estimated. According to the plots, at the start of deformation, the local strain largely coincides with the global strain, represented by the straight line, indicating homogenous plastic flow. The deviation of the local strain from the global strain represented the onset of PLC deformation. According to the results, as the specimen's geometrical width increases, the incubation strain also increased. This means that the development of PLC bands was delayed as the strain path moved towards plane strain conditions. These results are shown in Table 4. 6, where no differences were identified between the two materials.

Table 4. 6: Global true strain at the onset of PLC band development in CC5754 and DC5754.

Specimen Width	*Incubation Strain*
0.5 inch	0.010
1 inch	0.015
2 inch	0.035

4.3.2 Specimen Geometries for Right-Hand Side of FLD

(i) Strain Distribution Observations

DIC results from the observed strain map sequences show the formation and propagation of deformation bands in both materials for the 4 inch and 5 inch width specimen strain paths. The 7 inch width specimen's showed homogenous plastic flow and therefore, no deformation bands. The deformation bands for the 4 inch and 5 inch specimens display characteristics of PLC banding but their exact nature could not be determined from the DIC results alone. Nucleation of the bands occurred near the center of the specimen and propagated outwards in a discontinuous but correlated motion, spanning the width of the specimen. The deformation bands were not inclined to the specimen axis at any well-defined angle and propagated with a slight wave-like or curved profile, almost perpendicular to the tensile direction (Figure 4.14).

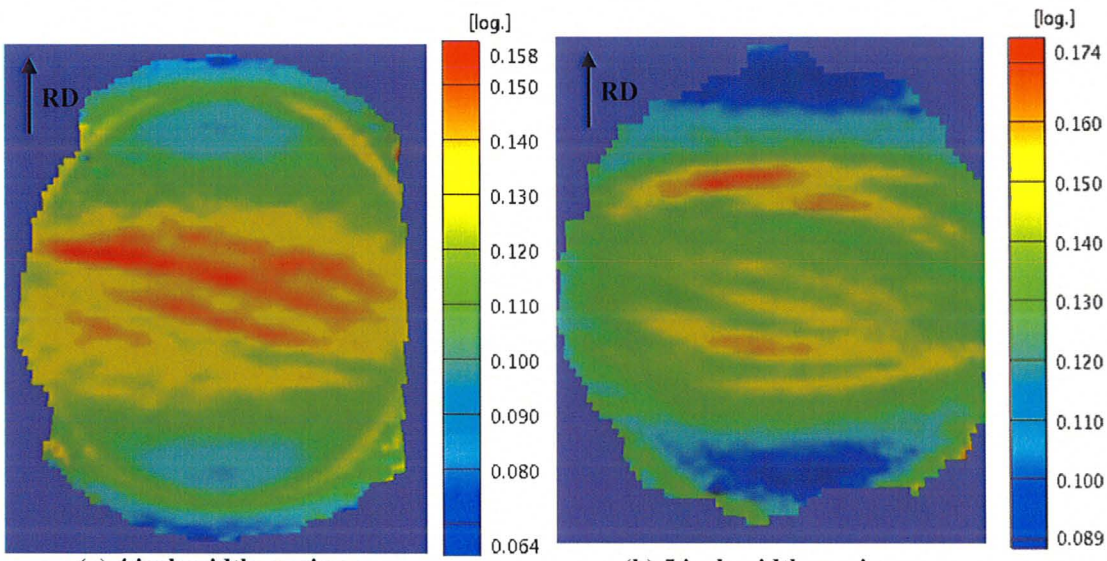

(a) 4 inch width specimen **(b) 5 inch width specimen**

Figure 4.14: Strain maps for tested specimens showing deformation behaviour.

Direct surface observations support the result observed by the DIC strain maps. The test specimens revealed the appearance of surface markings which are associated with PLC deformation bands. The deformation bands though, are not typical of those seen under uniaxial testing conditions. The bands span the specimen surface in a random manner with varying intensity, rather then in a regular parallel pattern as seen with type B PLC bands. An example of the surface markings observed can be seen in Figure 4.15 and Appendix B.

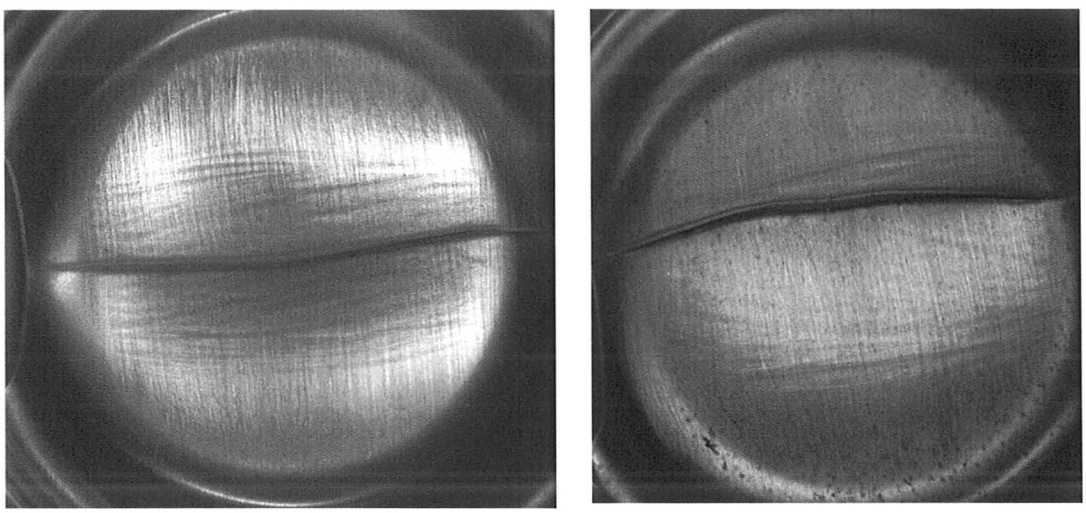

(a) CC5754 **(b) DC5754**

Figure 4.15: 4 inch width test specimens showing characteristic surface marking associated with PLC deformation bands.

(ii) Local Strain as a Function of Global Strain

The local true strain versus global true strain plots were evaluated with respect to the specimen geometry and material and can be seen in Figure 4.16 to Figure 4.18. The results show a similar relationship to those found in the result from the LHS specimen geometries. As the specimen's geometrical width increased, the maximum amount of

strain carried in the PLC bands decreased until no deformation bands were observed. The absence of PLC bands under balanced biaxial tension conditions is consistent with result found from various authors (Li and Lege, 1998; Robinson and Shaw, 1994). The maximum strain carried in the deformation bands are listed in Table 4.7.

Table 4.7: Maximum strain carried in the deformation bands according to the local and global true strain plots

Material	*4 inch*	*5 inch*	*7 inch*
CC	0.0171	0.0087	~ 0
DC	0.0204	0.0102	~ 0

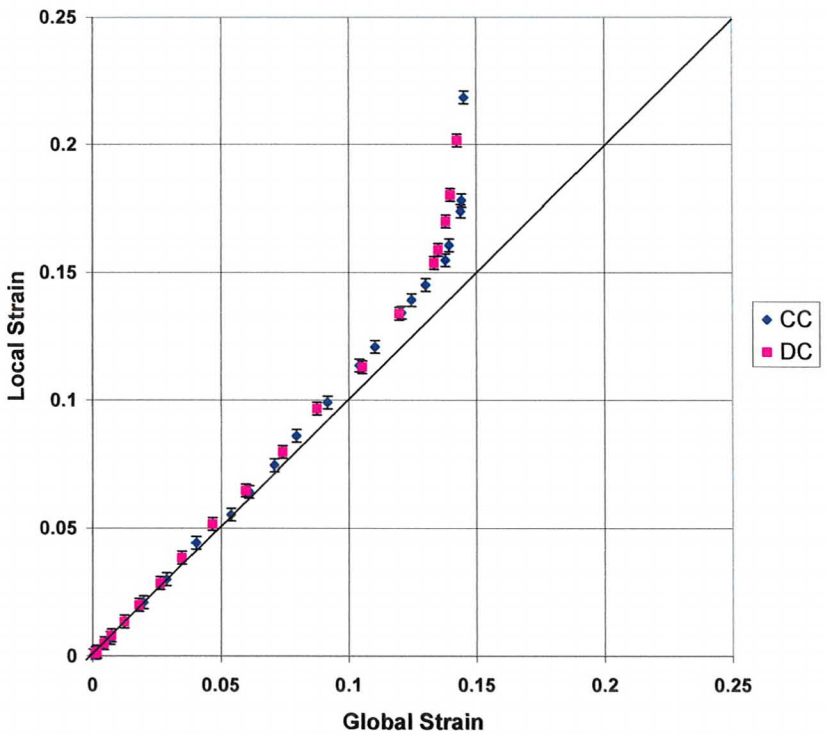

Figure 4.16: Plot of local true strain as function of global true strain for 4 inch width geometry.

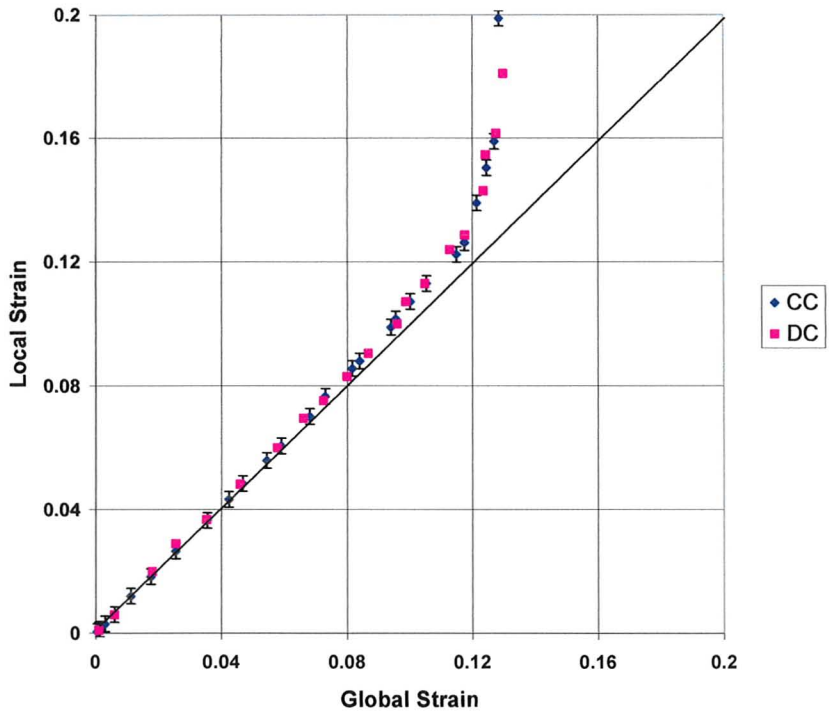

Figure 4.17: Plot of local true strain as function of global true strain for 5 inch width geometry.

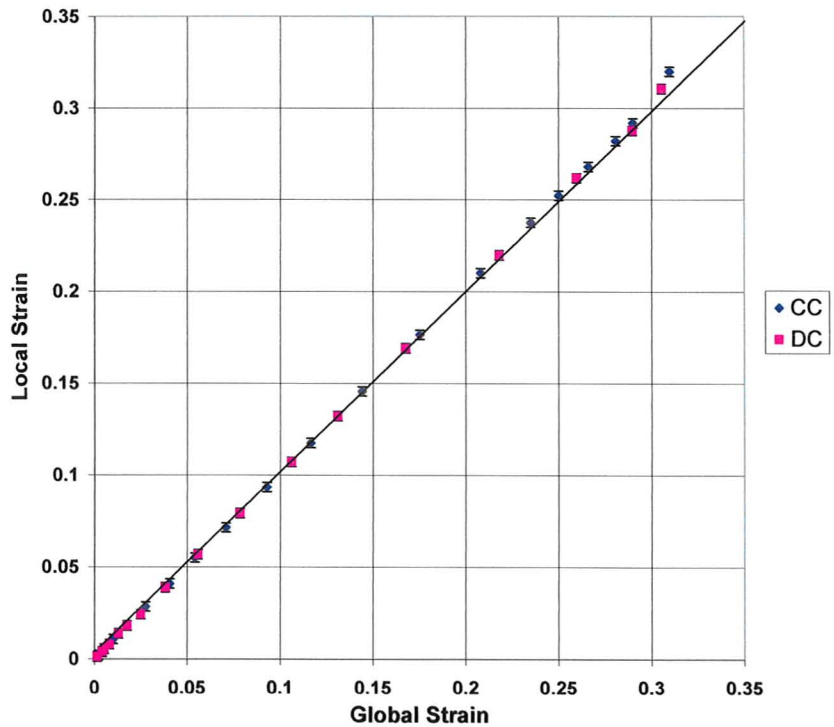

Figure 4.18: Plot of local true strain as function of global true strain for 7 inch width geometry.

The critical strain for the formation of deformation bands was also determined for the various specimen geometries and a similar trend is observed as seen from the result of the LHS samples. As the specimen's geometrical width increased, the critical strain increased meaning that the development of deformation bands was delayed as the strain path moves towards the balanced biaxial tension for the two materials.

Table 4.8: Global true strain at the onset of PLC band development in CC5754 and DC5754.

Specimen Width	*Incubation Strain*
4 inch	0.070
5 inch	0.080
7 inch	None

4.4 Microstructural Analysis of Fracture Behaviour

The following section investigates the post-necking and fracture behaviour of CC5754 and DC5754. The results are shown in two sections, left-hand side and right-hand side specimen geometries. All samples were prepared according to the procedure outlined in Chapter 3 (Section 3.8). From the optical micrographs, the thickness reduction of the sheet was measured, represented by t_{min}, and the major and minor strain values were calculated as described in Chapter 3 (Section 3.9). The strain paths for the specimen geometries were then plotted, along with the major and minor strains determined from the optical micrographs to compare the strains at which localization, shear banding and fracture occurred in the two materials.

4.4.1 Specimen Geometries for Left-Hand Side of FLD

Combinations of optical micrographs were used to examine the fracture behaviour of CC5754 and DC5754. The optical micrographs were taken from two samples; the first sample being tested up to the point of localization necking and the other sample to fracture. The fracture behaviour of the materials can be seen in Figure 4.19 to Figure 4.21.

The shear localization mode of ductile fracture occurs by two main mechanisms in AA5754. The first fracture mechanism, referred to as void sheeting, is identified by a smooth angled fracture profile inclined 50° to 60° to the tensile axis. This type of fracture is initiated along only one shear system and is associated with material instabilities that lead to rapid failure resulting in a small amount of overall total ductility. The second fracture mechanism, double-cup results from fracture along two or more shear systems. A characteristic "V" shaped profile is seen which results from the growth of a central void at the intersection of conjugate shear bands, followed by the formation of shear lips. This type of fracture mechanism yields a larger amount of total ductility in the fracture region. A third fracture mechanism can be defined, referred to as the mixed mechanism. This fracture mechanism initially begins as a double-cup failure but ends by the void sheeting mechanism. The fracture surface is defined by a jagged profile, which results from the initial development of a central void but due to material instabilities, rapid preferential failure occurs along one shear system.

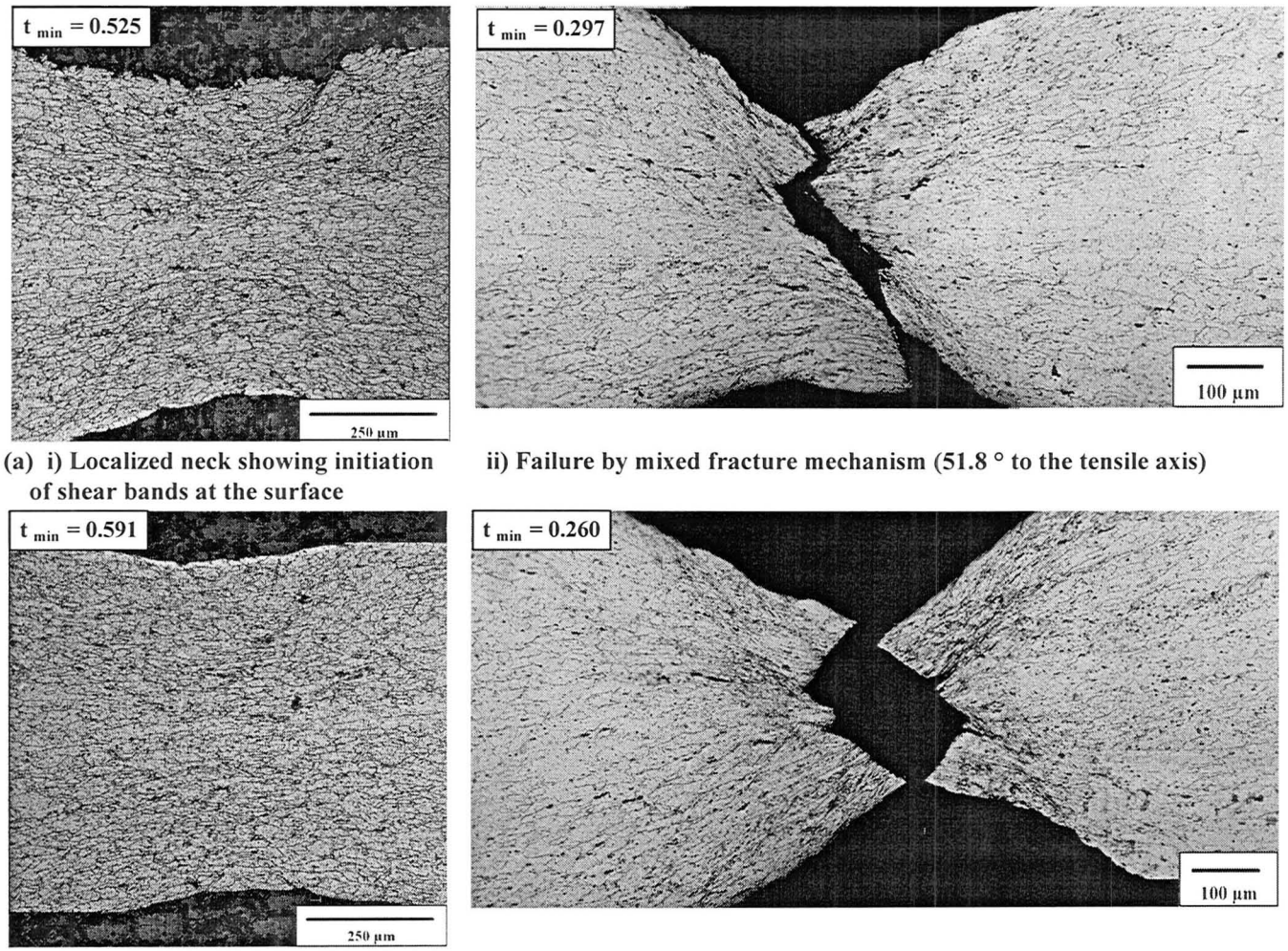

(a) i) Localized neck showing initiation of shear bands at the surface

ii) Failure by mixed fracture mechanism (51.8 ° to the tensile axis)

(b) i) Localized neck region

ii) Failure by double-cup fracture mechanism

Figure 4.19: Through-thickness sections of (a) CC5754 and (b) DC5754 showing strain localization (left) and the fracture profile (right) for 0.5 inch width specimens.

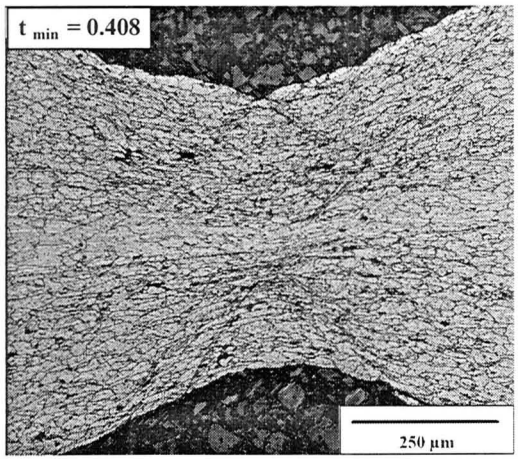

(a) i) Localized neck showing shear banding

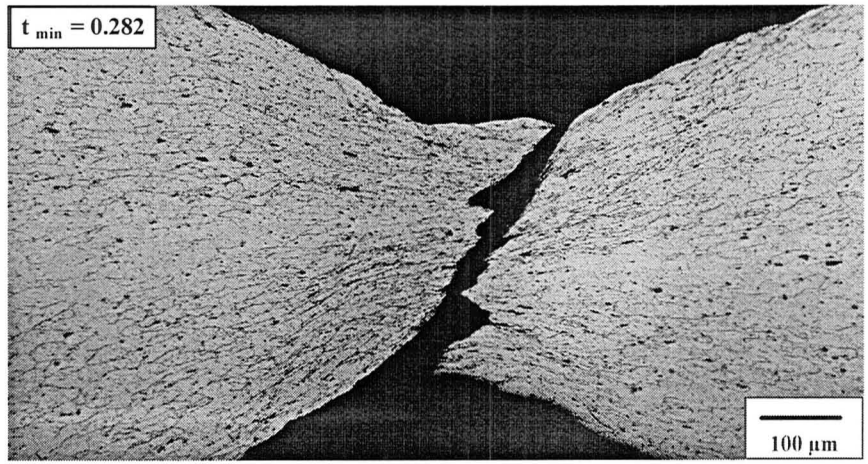

ii) Failure by mixed fracture mechanism (58.7° to the tensile axis)

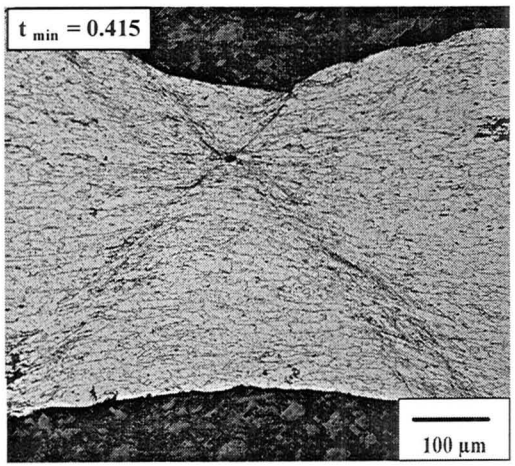

(b) i) Localized neck showing intense conjugate shear bands

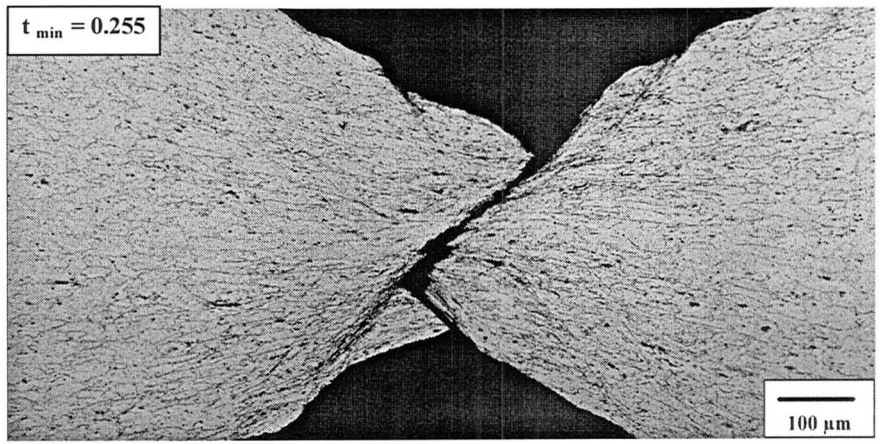

ii) Failure by mixed fracture mechanism (45.3° to the tensile axis)

Figure 4.20: Through-thickness sections of (a) CC5754 and (b) DC5754 showing strain localization (left) and the fracture profile (right) for 1 inch width specimens.

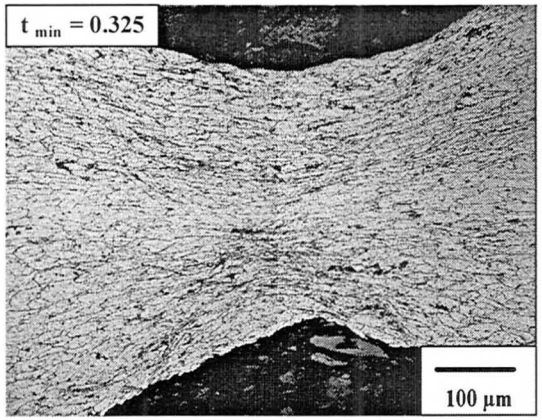

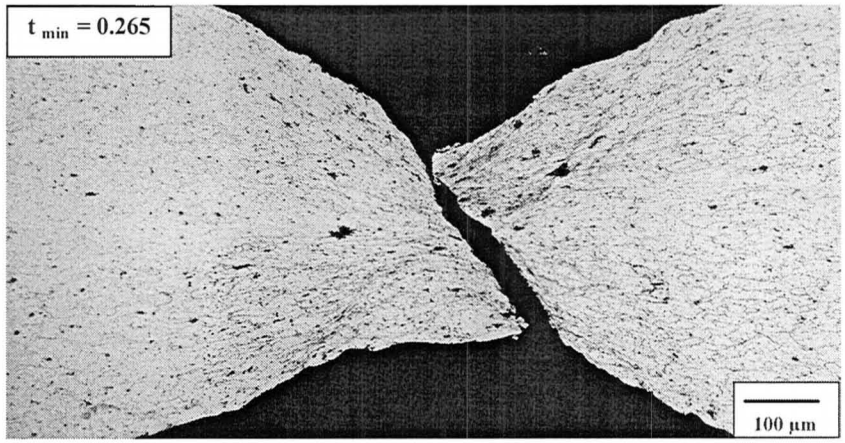

(a) i) Localized neck showing intense shear bands ii) Failure by void sheeting fracture mechanism (58.7° to the tensile axis)

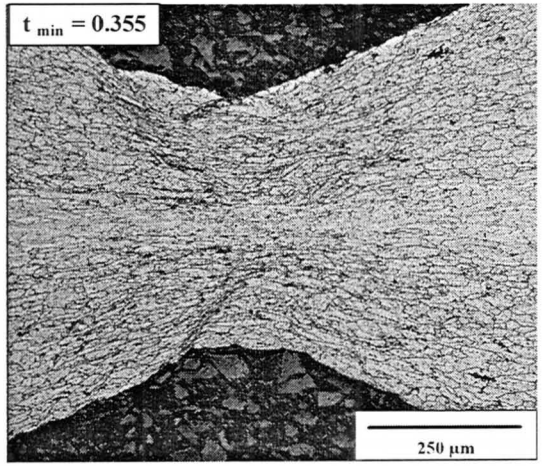

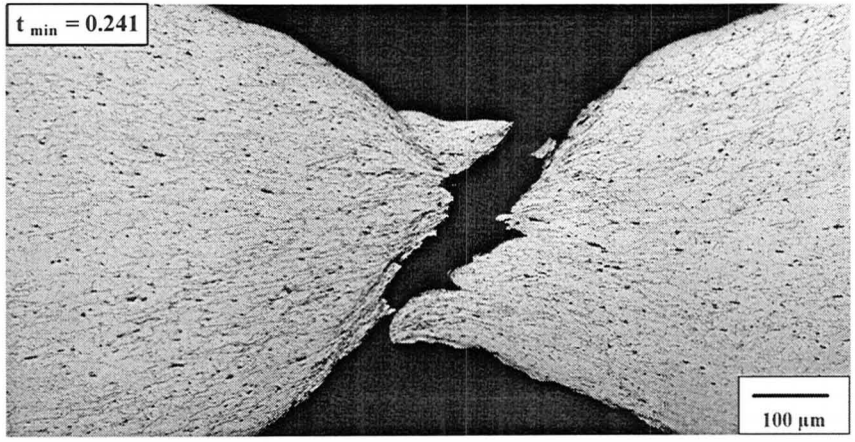

(b) i) Localized neck showing intense shear bands ii) Failure by mixed fracture mechanism (51.3° to the tensile axis)

Figure 4.21: Through-thickness sections of (a) CC5754 and (b) DC5754 showing strain localization (left) and the fracture profile (right) for 2 inch width specimens.

Examination of the material behaviour at necking for CC5754 and DC5754 showed areas of high strain concentration in the form of shear bands for all specimen geometries prior to fracture. According to the optical micrographs, the shear bands were initiated at the sample surface and then extended towards the sheet interior, intersecting with other developing shear bands. No shearing was visible outside the necking region. Variations in the fracture mechanism were also revealed by the examination of the fracture profiles for each material and specimen geometry and have been summarized in Table 4.9. Included in the table are the strain values calculated from the micrographs at necking and fracture. The CC material was observed to fail by the mixed and void sheeting fracture mechanisms while the DC material failed by the double-cup and mixed fracture mechanisms. From the LHS strain paths tested, the 0.5 inch width specimens showed the largest variation in fracture strain between the two materials. However, due the source of error associated with the thickness reduction measurements, any differences found between the materials will be considered negligible.

Table 4.9: Summary of failure mechanism and strain values determined from optical micrographs for LHS samples

Specimen Geometry Width	*Material*	*Strain in the Neck ±0.03*	*Fracture Strain ±0.05*	*Fracture Mechanism*
0.5 inch	CC	0.73	1.30	Mixed
	DC	0.61	1.44	Double-cup
1 inch	CC	0.95	1.33	Mixed
	DC	0.93	1.42	Mixed
2 inch	CC	1.16	1.37	Void sheeting
	DC	1.07	1.46	Mixed

4.4.2 Specimen Geometries for Right-Hand Side of FLD

Combinations of optical micrographs were used to examine the fracture behaviour of CC5754 and DC5754 for specimen geometries on the right-hand side of the FLD. All specimens were tested up to fracture since strain localization could not be captured. For fracture analysis, samples were taken along the centre line of the RD-LT plane at mid-width, near the site of fracture initiation (Figure 4.22).

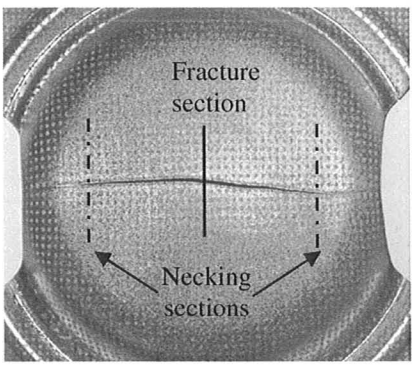

Figure 4.22: Sectioning of specimens for fracture and necking strain measurements.

For analysis of the localized necking region, sections were taken just outside of the fracture region (Figure 4.22). Therefore, the localized necking micrographs are not at the site of fracture initiation in the samples but they can be used to provide insight into the fracture behaviour of the materials since strain localization could not be captured. Figure 4.23 to Figure 4.28 presents the necking and fracture optical micrographs for the CC and DC material.

(a) Localized neck showing void formation

(b) Propagation of damage

(c) Propagation of damage

(d) Failure by double-cup fracture mechanism

Figure 4.23: Through-thickness sections of CC5754 showing shear banding and propagation of damage leading to fracture for 4 inch width geometry.

(a) Localized neck showing void formation

(b) Propagation of damage

(c) Propagation of damage

(d) Failure by double-cup fracture mechanism

Figure 4.24: Through-thickness sections of DC5754 showing shear banding and propagation of damage leading to fracture for 4 inch width geometry.

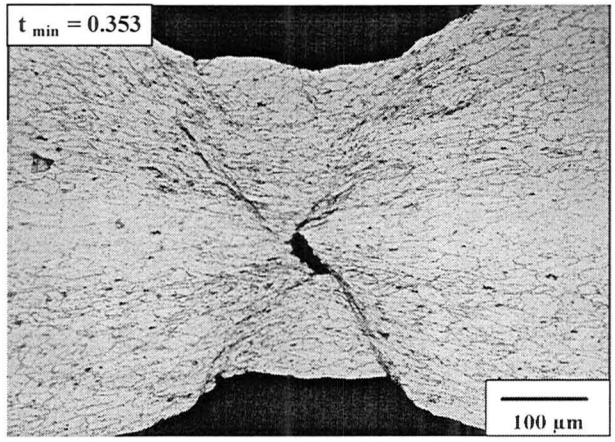

(a) Localized neck showing void formation

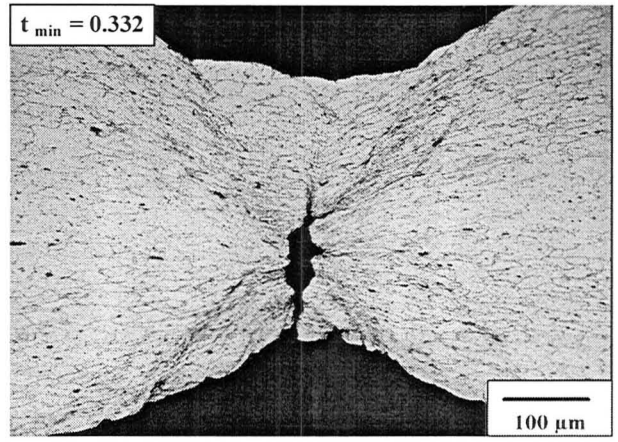

(b) Propagation of damage

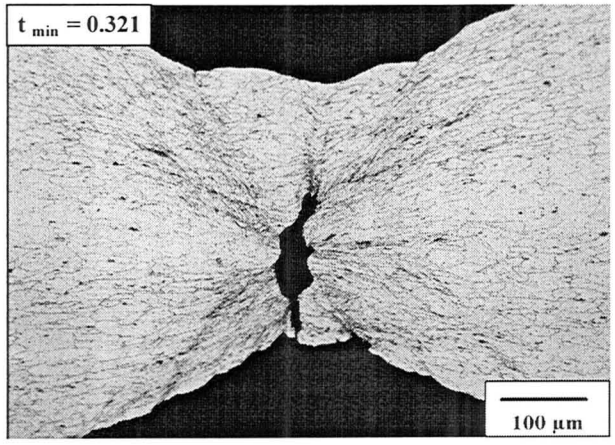

(c) Propagation of damage

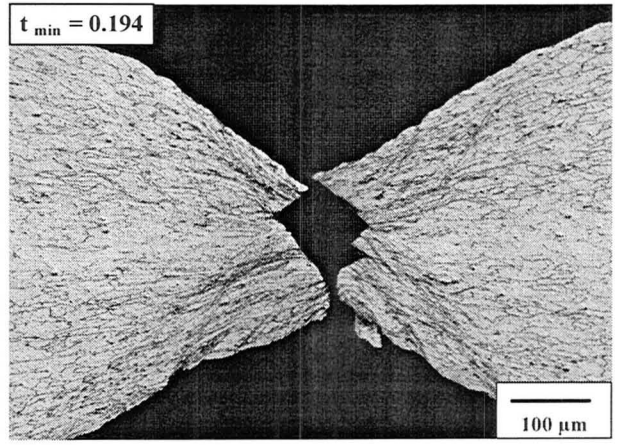

(d) Failure by double-cup fracture mechanism

Figure 4.25: Through-thickness sections of CC5754 showing shear banding and propagation of damage leading to fracture for 5 inch width geometry.

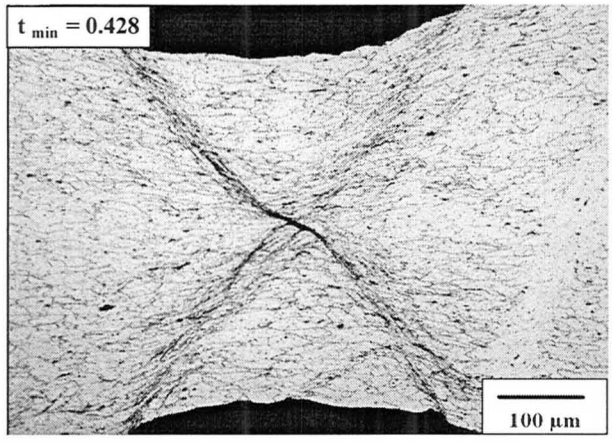

(a) Localized neck showing void formation

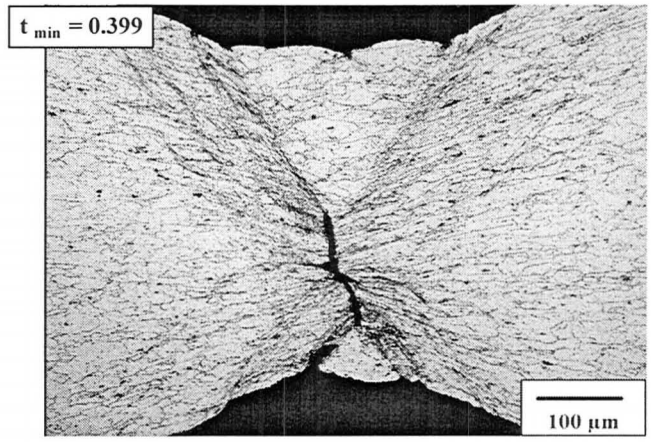

(b) Propagation of damage

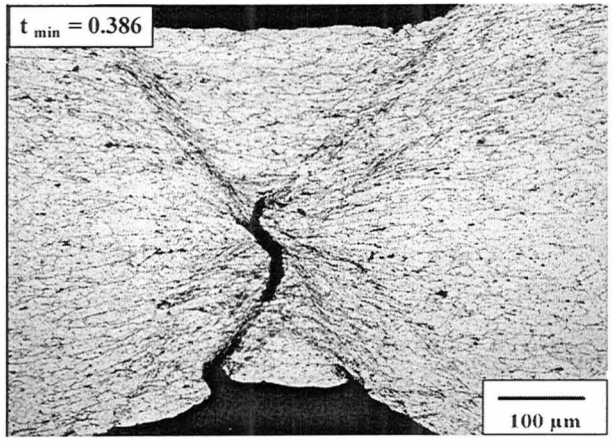

(c) Propagation of damage

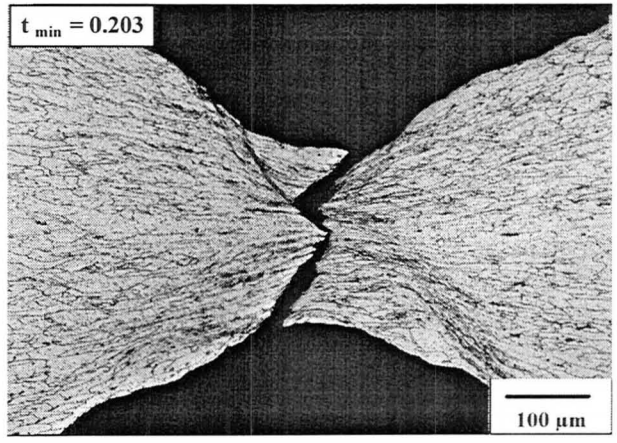

(d) Failure by mixed fracture mechanism

Figure 4.26: Through-thickness sections of DC5754 showing shear banding and propagation of damage leading to fracture for 5 inch width geometry.

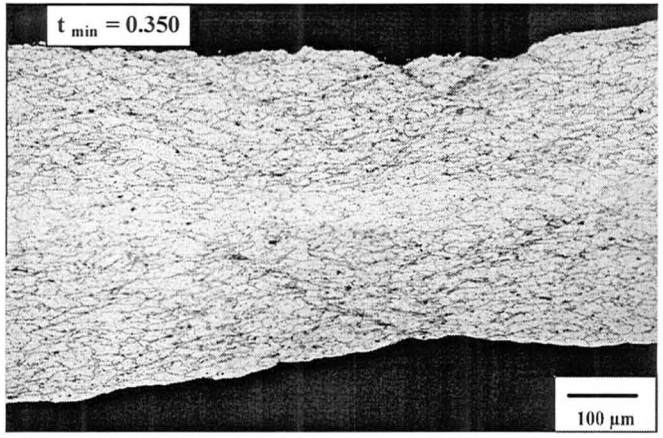

(a) Localized neck showing minor shear banding

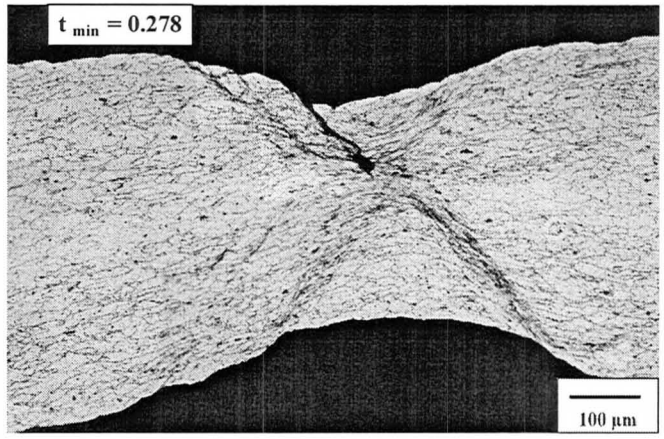

(b) Initiation of damage along shear band

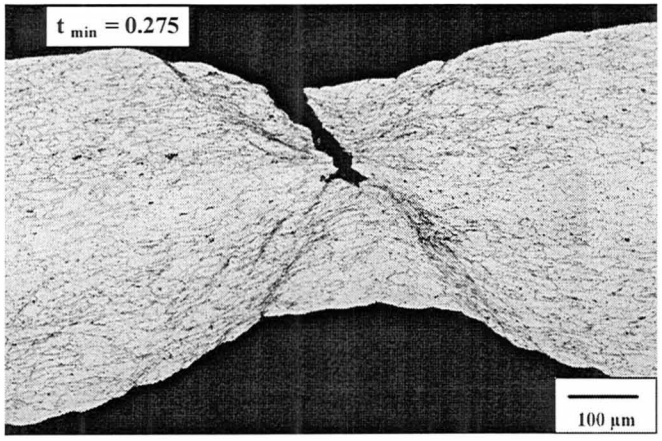

(c) Propagation of damage

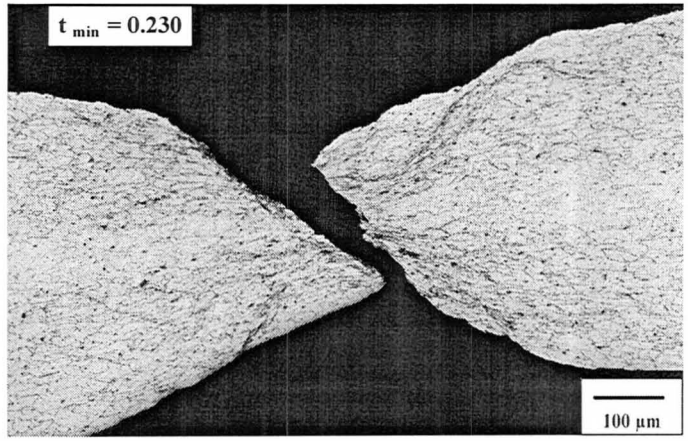

(d) Failure by void sheeting fracture mechanism

Figure 4.27: Through-thickness sections of CC5754 showing shear banding and propagation of damage leading to fracture for 7 inch width geometry.

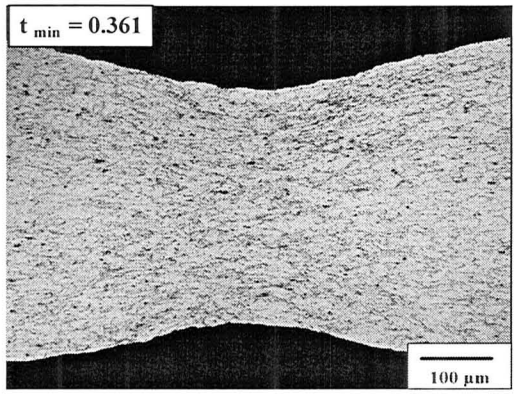

(a) Localized neck showing no shear bands

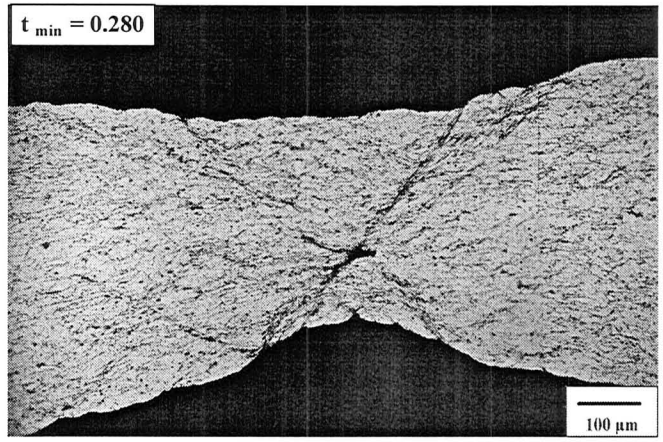

(b) Localized neck showing shear banding and void formation

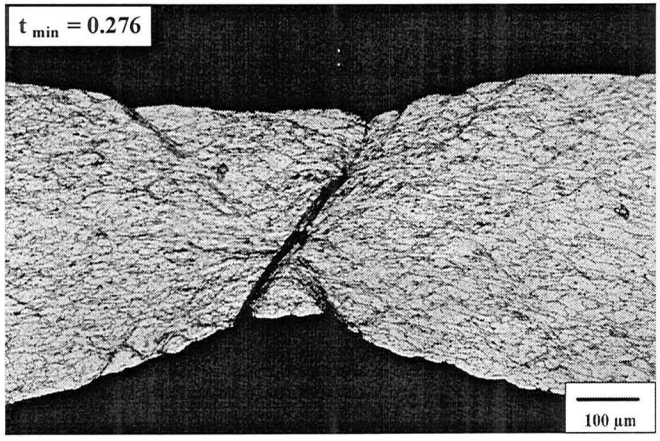

(c) Propagation of damage

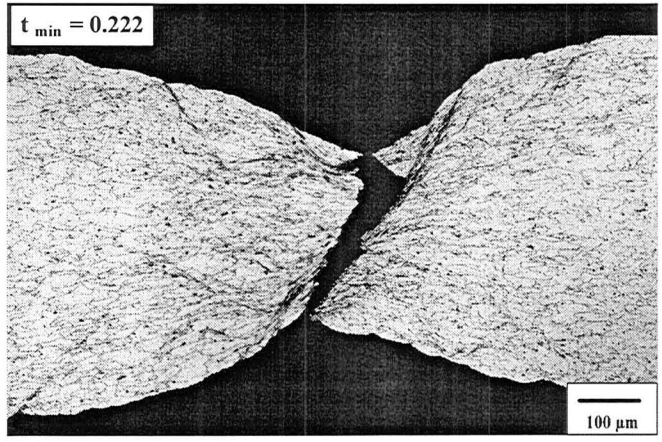

(d) Failure by mixed fracture mechanism

Figure 4.28: Through-thickness sections of DC5754 showing shear banding and propagation of damage leading to fracture for 7 inch width geometry.

Examination of the material behaviour at necking for CC5754 and DC5754 shows macroscopic shear bands for all specimens prior to fracture. For the 4 inch and 5 inch width specimens, visible shearing was limited to the localized necking region. For the 7 inch width geometry, an extensive quantity of shear bands were seen inside and outside of the necking region, especially for the DC material (Figure 4.26 (b), (c)).

Both materials reveal a pair of intense conjugate shear bands inside the neck region from which a central void forms. As deformation continues, the void grows either centrally by a ductile cutting process or preferentially along one shear system, which eventually leads to fracture. For the 4 inch and 5 inch width geometries, void growth in the CC material showed a preference to the shear cutting while the for the DC material, the void grew preferentially along one shear band system. For the 7 inch width geometry, both materials showed preferentially void growth along one shear band system.

The fracture strains between the materials showed very little variation despite differences observed in the fracture mechanism for each material and specimen geometry, which has been summarized in Table 4.10. Included in the table are the strain values calculated from the micrographs at necking and fracture. The CC material was observed to fail by the double-cup and void sheeting fracture mechanisms while the DC material failed by the double-cup and mixed fracture mechanisms.

Table 4.10: Summary of failure mechanism and strain values determined from optical micrographs for RHS samples

Specimen Geometry	*Material*	*Strain in the Neck ±0.03*	*Fracture Strain ±0.05*	*Fracture Mechanism*
4 inch width	CC	1.05	1.45	Double-cup
		1.17		
		1.21		
	DC	0.96	1.47	Double-cup
		1.05		
		1.28		
5 inch width	CC	1.04	1.31	Double-cup
		1.10		
		1.14		
	DC	0.85	1.27	Mixed
		0.92		
		0.95		
7 inch width	CC	0.525	0.734	Void sheeting
		0.639		
		0.645		
	DC	0.510	0.750	Mixed
		0.636		
		0.644		

The strain paths of the specimen geometries for CC5754 and DC5754 were also plotted and can be seen in Figure 4.29 and Figure 4.30. Included in the plots are the major and minor strains determined from the optical micrographs for post-necking and fracture and the forming limits. The difference in strain between the fracture limits and forming limits is indicative of the amount of post-necking strain or deformation the material can withstand before fracture. Typically, as the strain path shifts to the RHS of the FLD, the amount of post-necking strain that can be observed decreases. This trend is generally observed but due to the scatter in the fracture strains results for CC5754 and DC5754, no variation in post-necking strain can be identified between the materials.

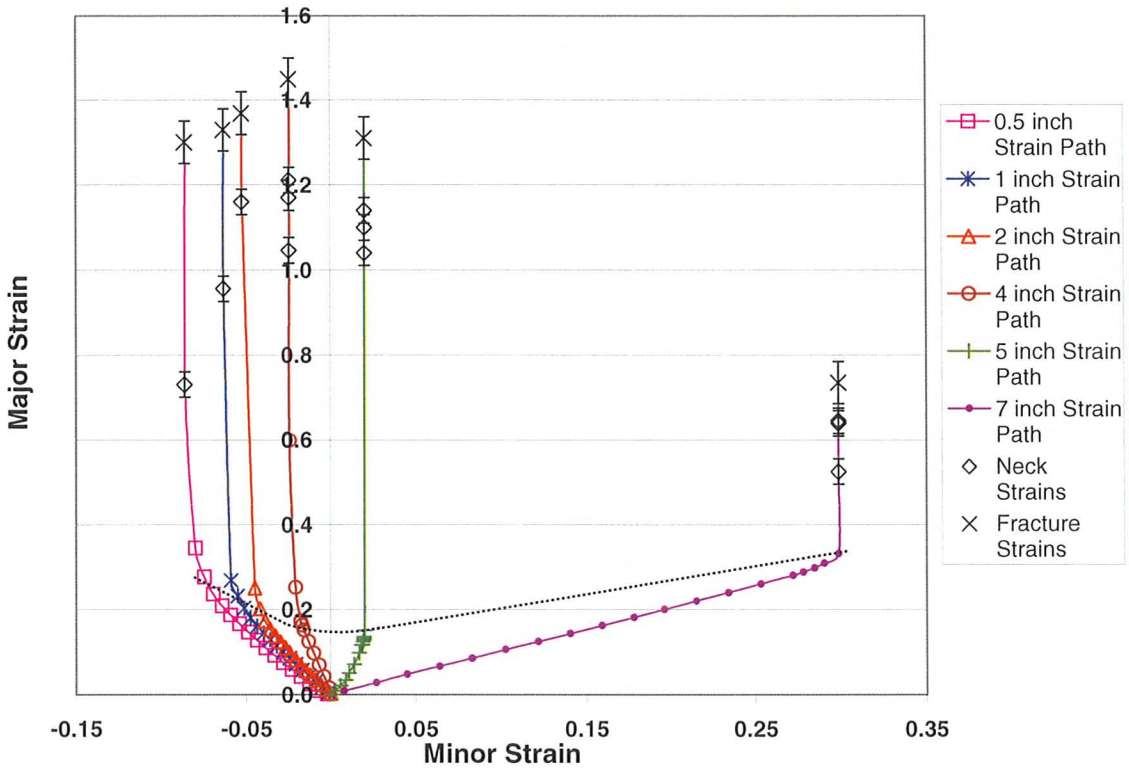

Figure 4.29: CC5754 specimen strain paths showing necking and fracture strains.

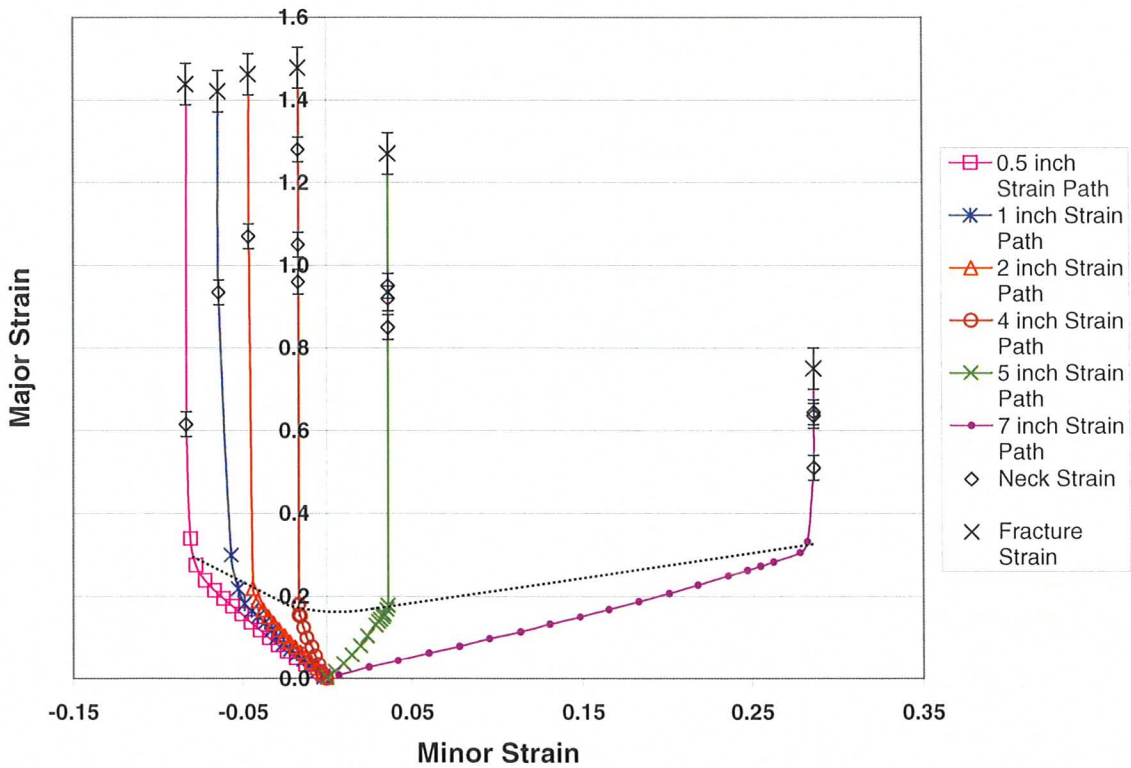

Figure 4.30: DC5754 specimen strain paths showing necking and fracture strains.

Chapter 5
Discussion

The following chapter will discuss the experimental results obtained in the current work, as provided in Chapter 4. The first section compares the microstructural characteristics of the materials and its influence on the mechanical properties. From the gained understandings of the materials mechanical properties, the forming limits are then examined along with the deformation behaviour of the sheet materials as a function of specimen geometry. The next section focuses on the post-necking and fracture behaviour of the materials from the optical microscopy results and finally, the testing technique is evaluated.

5.1 Influence of Material Characteristics on the Uniaxial Tensile Mechanical Properties of CC5754 and DC5754

The first step to understanding formability is to understand the relationship between the microstructural and the intrinsic characteristics of a material and the measured mechanical properties. This can be accomplished by examining the tensile response of CC5754 and DC5754 in uniaxial tension and applying the information to the formability and failure results. From the tensile testing results, differences between the two materials were noticed, most specifically in terms of the achieved strength level and uniform strain. Therefore, the variation in mechanical properties between the two

materials is examined with respect to the as-received material characteristics, such as grain size and compositional differences, and the rate of work-hardening.

5.1.1 Grain Size

According to Burger at al. (1995), the 5000 series of Al-Mg alloys exhibits the largest grain size dependence of the yield strength in comparison to most other aluminum alloys. This is due to the stress required to initiate plastic flow in the material due to dynamic strain aging (DSA). As a result, any comparisons between different Al-Mg alloys should take grain size effects into account. The differences in grain size and structure though, arises primarily from the variation in dispersoid content and distribution, which depend on the processing parameters such as the extent of cold work and the final annealing treatment (Burger et al., 1995).

The grain size dependence of the yield stress is given by the Hall-Petch equation:

$$\sigma_y = \sigma_0 + kd^{-1/2} \tag{5.1}$$

where σ_y represents the yield stress (MPa), σ_0 represents the frictional stress (MPa), k is a constant ($MNm^{-3/2}$) which is specific to the material and d is the average grain size (m). As a result, the yield stress is inversely related to the grain size of the material strengthening i.e. smaller grain sizes give higher yield strengths.

Considering the microstructural analysis results of the as-received material in the current work, the average grain size of CC5754 and DC5754 was found to be 23.2 μm and 24.9 μm respectively. In considering these results, the CC material should have a

slightly higher yield stress due to the smaller grain size. According to the tensile properties listed in Table 4.1, the yield stress of the CC material is lower than that of the DC material (99 MPa for DC5754 versus 95 MPa for CC5754). Eqn. 5.1 can also be applied beyond the yield point to describe the flow stress behaviour of AA5754 (Lloyd and Court, 2003). It was found that the value for the constant k decreases after yielding, indicating that the large grain size effect is primarily associated with initiating plastic flow. This means that even less variation should be observed between the ultimate tensile strengths of the two materials, which according to Table 4.1, is clearly not observed (288 MPa for DC5754 versus 263 MPa for CC5754). Therefore, grain size variations in CC5754 and DC5754 is not responsible for the differences in flow stress behaviour, as seen from the true stress-strain curves in Figure 4.2.

5.1.2 Composition and Work-Hardening Behaviour

The main alloying element in the 5000 series alloys is Mg which is responsible for providing solid solution strengthening to the alloy. As a result, the yield and ultimate tensile strength also increases with increasing solute concentration of Mg. The extent of work-hardening in Al-Mg alloys has been shown to increase with the Mg content according to Burger et al. (1995) and Lloyd (1980). Therefore, the importance of Mg content on the strength, deformation and tensile elongation of Al-Mg alloys should also be considered.

According to the chemical composition of the materials provided in Table 3.1, CC5754 contains a slightly higher wt% of Mg in comparison to the DC5754 (3.1 wt% for DC5754 versus 3.4 wt% for CC5754). Let us consider a situation in which no second-

phase particles containing Mg are present in the alloys. In this case, the CC material would exhibit a higher yield and ultimate tensile strength due to the greater concentration of Mg in solid solution. However, this situation is highly unlikely to occur since some Mg will form Mg_2Si second-phase particles but the effectiveness of the particles as a strengthening mechanism is considered to be small (Girard, 2002). Therefore, strengthening of the 5000 series alloys is due to the amount Mg which remains in solid solution with the aluminum matrix.

Various studies have shown that Al-Mg alloys contain a large variety of second-phase particles, with a wide size distribution which is influenced by the casting process. The microstructures of CC and DC cast material have been quantitatively analyzed to determine the nature of the second-phase particles. However, the exact nature of all the particles phases is still not known since the 5000 series alloys contain a number of different kinds of constituent particles (Pilkey et al., 1995). Therefore, the exact amount of Mg which is found in solid-solution within the two materials is not conclusively known.

The influence of Mg content in regards to deformation behaviour has been extensively studied at the atomic scale and is related to the work-hardening capability of the material. Considering the deformation of AA5754, after yielding the flow curves are heavily serrated and the flow stress has a negative strain rate sensitivity (m). This is a result of the DSA phenomenon where shear stresses acting on slip planes cause dislocations to move through the lattice where they interact with Mg solute atoms. The diffusion of the solute atoms temporarily inhibits dislocation mobility which makes

dislocation rearrangement difficult and enhances slip resistance resulting in a high work-hardening rate. With increasing time though, the role of the Mg atoms to act as obstacles becomes more effective and the force needed to move dislocations increases. As a result, the flow stress exhibits a negative strain rate sensitivity and plastic flow instabilities are observed, usually in the form of narrow bands of localized deformation (Cieslar et al., 2003). In addition, as the Mg content increases in the material, the amplitude of the serrations observed on the stress-strain curve increases. This is a consequence of DSA which reflects the role of Mg atoms in locking dislocations and increasing the extent of work-hardening in the alloy (Lloyd, 1980).

During tensile testing, the rate of work hardening ($d\sigma/d\varepsilon$ or θ) of a material has been shown to control both the flow stress and the achieved uniform strain when the Considère Criterion (1885) is satisfied (Eqn. 5.2). Once the work-hardening capacity of the material is exhausted, instability in the form of diffuse necking occurs, thus limiting the amount of uniform strain that can be achieved.

$$\frac{d\sigma}{d\varepsilon} = \sigma \tag{5.2}$$

Many stress-strain relationships have been proposed to explain the plastic deformation behaviour of a material during uniaxial tension testing. The most commonly used expression is the Hollomon equation (1945), which describes work-hardening as a power law function of stress and strain. According to the equation, k and n are constants known as the strength coefficient and strain hardening exponent, respectively.

$$\sigma = k\varepsilon^n \tag{5.3}$$

The Hollomon Eqn. does not adequately describe the deformation behaviour of Aluminum alloys including AA5754, especially in terms of estimating the onset of diffuse necking according to the Considère Criterion. As a result, the strain hardening exponent is greatly overestimated since the curves must be extrapolated beyond the experimental data (Table 4.1). Works using the Voce equation (1948), which describes plastic deformation in terms of dislocation dynamics, have shown to be more accurate, according a study performed by Duan et al. (2005), on AA5754. The Voce equation is expressed in the form below where *a, b* and *c* are constants.

$$\sigma = B - (B - A)\exp(-n_o\varepsilon) \tag{5.4}$$

A comparison of the curve fittings from the Holloman Eqn. and Voce Eqn. is shown in Figure 5.1. According to the plot, the Holloman Eqn. does not fit the experimental data well near diffuse necking; for the stress values are overestimated, indicating that the material is work-hardening at a higher rate than what actually is observed.

The work-hardening rates ($d\sigma/d\varepsilon$) of the materials were obtained by fitting the experimental data with the Voce Eqn. (Figure 5.2). According to the plot, the uniform strain was then determined by the point of intersection with the experimental stress-strain curve and was found to be 0.170 and 0.185 for CC5754 and DC5754, respectively. These values are slightly lower that that listed in Table 4.1 but overall the values agree well with the experimental data. Upon examination of the work-hardening curves, the CC5754

material shows a lower work-hardening rate and a greater decrease in the work-hardening rate with strain in comparison to the DC material. Thus, the difference in the shape of the work-hardening curves reflects the difference in attainable uniform strain between the materials.

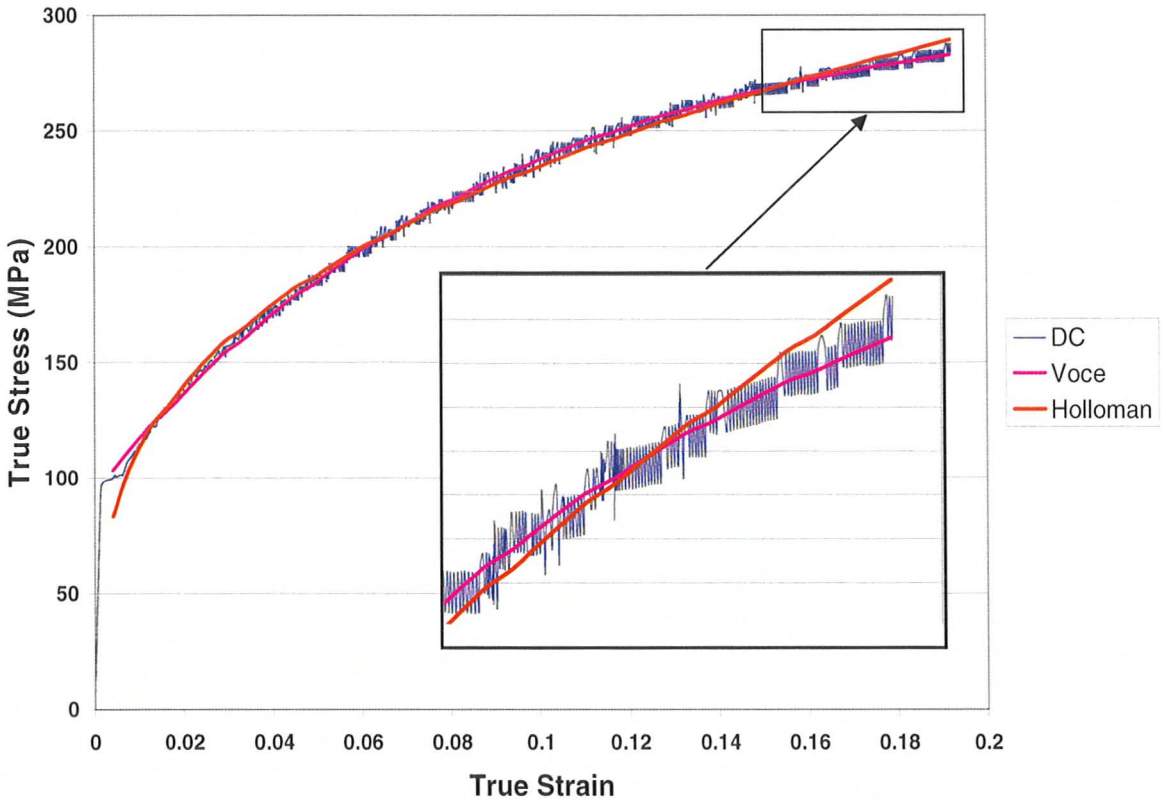

Figure 5.1: Comparison of stress-strain relations used for curve fitting of DC5754 tensile specimens.

The rate of work-hardening is essentially controlled by two factors; the accumulation of dislocations which strengthen the material and dynamic recovery processes which soften. With continued deformation and straining of the material, the influence of the dynamic recovery processes on the rate of work-hardening becomes greater resulting in a continual decrease of the work-hardening capacity of the material.

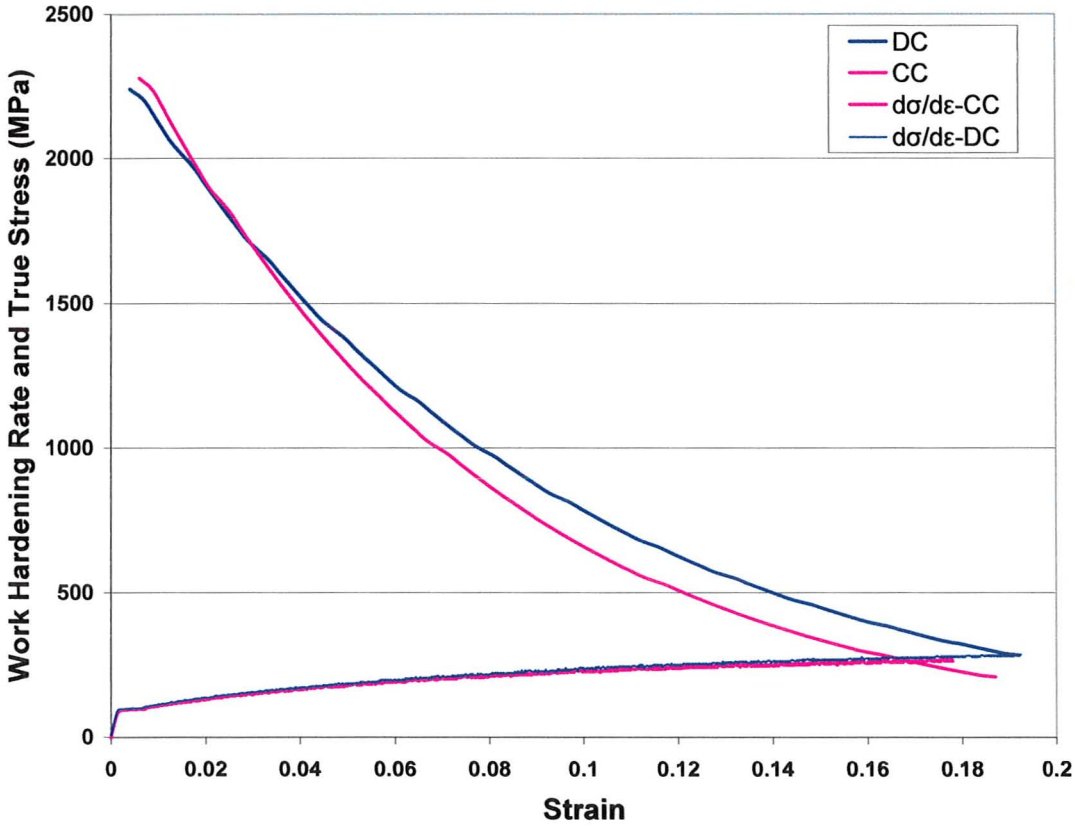

Figure 5.2: Plot of work hardening rate dσ/dε as a function of strain following the Voce Eqn. for uniaxial test specimens of CC5754 and DC5754.

If we consider the tensile properties of CC5754 and DC5754, listed in Table 4.1, the yield and ultimate tensile strengths of the CC material is lower than that of the DC material, despite the smaller grain size and higher wt% of Mg according to the chemical composition. These results seem contradictory and suggest more investigations must be done to determine the concentration of Mg in solid solution.

5.2 Analysis of Forming Limits

5.2.1 Overview

The amount of useful plastic deformation in sheet metal forming operations is limited by the onset of strain localization which is a combination of the uniform strain and the amount of deformation that can be achieved after diffusing necking. A schematic view of a typical failure region in a sheet metal formed specimen can be seen in Figure 5.3. As described in the previous section, uniform strain is strongly influenced by the work-hardening behaviour of the material and is a function of the rate of decrease of the work-hardening rate ($d\sigma/d\varepsilon$) with strain. After diffuse necking, the rate of specimen thinning is greater than the rate of strain hardening and deformation is unstable. At this point, the amount of post-uniform deformation that can be attained is highly dependent on the strain-rate sensitivity of the material. This is represented by the instability strain in Figure 5.3, which corresponds to the onset of strain localization. Therefore, the forming limits of CC5754 and DC5754 are examined with respect to the material properties that can influence the deformation behaviour and limit the materials performance.

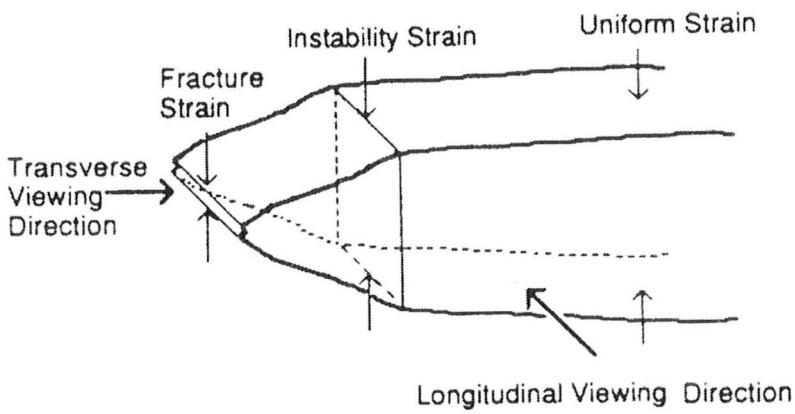

Figure 5.3: Schematic view of failure region of a uniaxial sheet metal specimen (Morris et al., 1987).

5.2.2 Influence of Material Properties on the FLC

A material's resistance to necking instability is promoted by high work hardening rates, which is associated with a high n-value. An increase in the value of n has a favourable influence on plastic deformation since the corresponding increase in the flow stress assists in evenly distributing the strain within the sheet metal. Therefore, a material with a large n value will typically have higher limit strains. However, the formability of aluminum is lower than that of steel even though the n value is estimated to be higher according to the Hollomon Eqn. The critical strain at which localized necking occurs on the LHS of the FLD, as described by Hill (1952), is consider to follow Eqn. 5.5.

$$\varepsilon_1^* = \frac{n}{1+\beta} \tag{5.5}$$

For the case of uniaxial tension, localized necking commences at strain equal to $2n$ and diffuse necking at strains equal to n, according to Figure 5.4. This situation is not observed for AA5754.

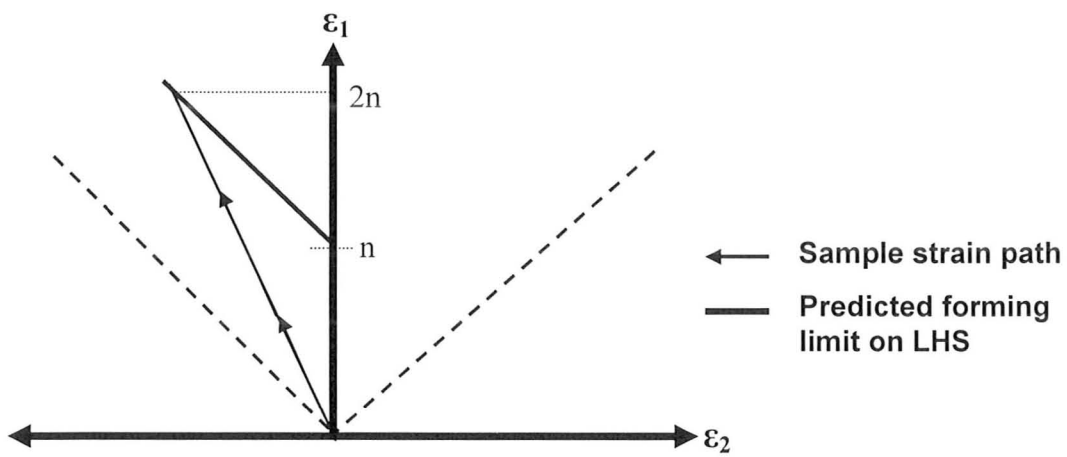

Figure 5.4: Conditions for localized necking on the LHS of the FLD according to Hill's theory with a material obeying the Holloman Eqn.

The disagreement is attributed to the decreasing value of n under conditions of larger plastic deformation. An example of this can be seen in Figure 5.5 for an Al-Mg alloy. If we take the instantaneous strain hardening exponent n' at the strain equal to diffuse necking in Figure 5.5, was find that n' is approximately equal to 0.23. Under conditions of uniaxial tension, localized necking commences at a strain equal to 1.35 n' and diffuse necking at strain equal to $0.8n'$. Therefore, the value of n, as predicted by the Holloman Eqn. cannot be used directly to compare the formability of CC5754 and DC5754.

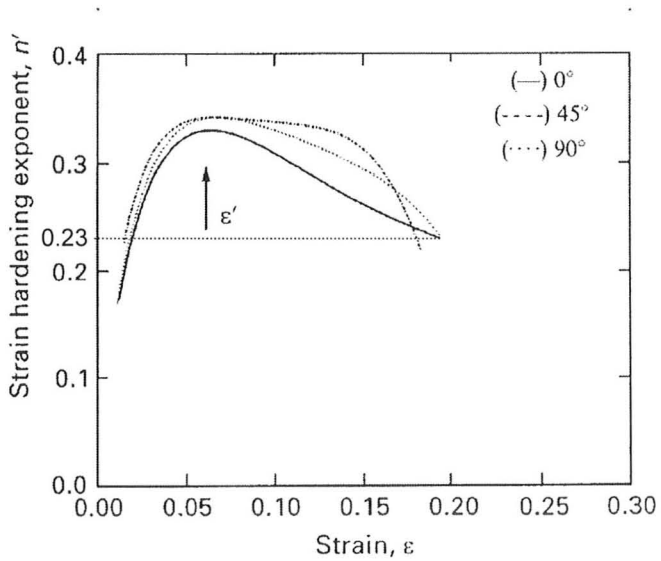

Figure 5.5: Instantaneous strain hardening exponent (n′) variation with strain for Al-Mg6.8 alloy sheet (Romhanji et al., 1998). Data taken at various angles to the rolling direction.

For a material obeying the Voce Eqn. (5.4), the strain at which diffuse necking occurs can be estimated using the Considère Criterion. It appears that the instability strain is dependent upon three parameters, as shown in Eqn. 5.6.

$$\varepsilon = \frac{1}{n_o} \ln\left[\frac{(n_0 + 1)(B - A)}{B}\right] \tag{5.6}$$

Unlike determination of forming limits using the Hollomon Eqn., where a direct relationship of the n-value with strain path variations has been established (Eqn. 5.5), the same can not be said for the Voce Eqn. According to Eqn. 5.6, it is clear that the limit strain increases with increasing values of B and decreases with increasing values of A and n_o. However, the relationship of these parameters with varying strain paths requires a more intensive analysis which would be dependent on the properties of the material.

Upon examination of the in-plane forming limit curves for CC5754 and DC5754, it is apparent that the forming limits of the two materials are similar which is consistent with other studies reported by Kang (2002). According to Figure 4.7, the DC material showed a slightly higher forming limit on the LHS in comparison to the CC material (approximately 3 pct). According to Burger at al. (1995) and Romhanji et al., (1998), the contribution of post-uniform strain after diffuse necking to the forming limits of aluminum alloys is small and is considered to be negligible to the overall global strain. Again, this is a result of the negative strain-rate sensitivity of the material, where the growth of the neck is accelerated by strain-rate softening leading to rapid localization after diffuse necking. If we can extend the information that was found during tensile testing of the uniaxial specimens to other strain paths, then the differences in the forming limits of CC5754 and DC5754 can be attributed to a variation in uniform strain and work-hardening rate.

For the RHS of the FLD, the forming limits can not be analyzed and predicted in the same manner as the LHS. During deformation of AA5754 under stretching conditions, the uniform strain is followed almost instantaneously by strain localization

and fracture once failure occurs. The influence of material properties such as n, strain-rate sensitivity (m) and the inhomogeneity factor, f_0 have been used to quantitatively predict and analyze the limit strains on the RHS but the results do not always agree well with the experimental data due to the complexity of the relationship between the material properties. Upon examination of the RHS of the FLD for CC5754 and DC5754 (Figure 4.7), it can be seen that nearly identical forming limits were found (less than 1 pct difference). If the M-K analysis is applied, which assumes that limit strains under stretching conditions are controlled by material imperfections, then f_0 does not vary significantly between the two materials. Conceptually, f_0 is considered to represent microstructural variations such as thickness variations, non-uniform distribution of particles, varying texture etc. These finding suggest that any microstructural variations identified between CC and DC cast 5754 do not play a large role in limiting the formability under stretching conditions.

5.3 Influence of the Deformation Behaviour on Strain Localization

5.3.1 Spatial Features of Deformation Bands

The PLC effect is a manifestation of macroscopic scale non-uniformities which can be revealed by a variety of behavioural phenomena. It is most commonly observed by the repeated appearance of discontinuities on the stress-strain curve during deformation referred to as serrated yielding. Surface marking, in the form of regularly spaced parallel bands, are also observed in conjunction with the serrations on the stress-

strain curve. Due to the limitations of testing technique used in the current work, as a result of the forming press load cell and software, the punch load versus punch displacement data was unable to reveal serrations due to the presence of PLC bands. However, surface marking and observations from the DIC strain map sequences do support deformation behaviour related to PLC banding. Therefore, the basis of the deformation behaviour analysis is provided by these two main sources.

The deformation producing type B surface markings is recognized as a succession of localized necks propagating along the gauge length which may either be continuous or discontinuous in nature. The angle of inclination of the localized necks on the LHS of the FLD is predicted to occur at a specific angle to the loading direction as described by Hill (1952) under plane stress conditions (Robinson and Shaw, 1994). Using Eqn. 2.2, where β is defined from Eqn. 2.1, the results show that the predicted angle of inclination of the PLC bands agrees well with the measured values for each strain path (Table 5.1). Differences in the angle, for a given strain path, have been attributed to the influence of rolling texture (Webernig et al., 1986).

Table 5.1: Comparison of the predicted inclination angles of the deformation bands with measured values for specimen geometries on the LHS of the FLD.

Material	*0.5 inch*		*1 inch*		*2 inch*	
	Actual	*Predicted*	*Actual*	*Predicted*	*Actual*	*Predicted*
CC	59°	60.3°	62°	63°	67°	64.5°
DC	62°	62.6°	64°	64.2°	65°	65.9°

The deformation behaviour producing the surface markings on the specimen geometries on the RHS of the FLD, most particularly the 4 inch and 5 inch width geometry, do not correlate well with the characteristics seen on the LHS. The deformation bands were not inclined to the specimen axis at any well-defined angle and propagated with a slight wave-like or curved profile in the tensile direction. For the 4 inch width specimen, the strain path lies just to the LHS of the FLD. The predicted inclination angle of the deformation bands is between 71-72° but measurements show angles ranging from 67° to as high as 86°. For the 5 inch width specimen, the strain path lies to the RHS of the FLD, under stretching conditions. The number of surface markings observed and their intensity was drastically decreased in comparison to the 4 inch width specimens. Therefore, the only conclusion that can be drawn is that under plane strain and stretching conditions, the deformation behaviour of the PLC bands is significantly altered or suppressed from that seen under strain paths seen on the LHS of the FLD.

No PLC bands or surface markings were associated with the 7 inch width specimens which is consistent with results observed from various authors on balanced biaxial specimens (Webernig et al., 1986, Robinson and Shaw, 1994; Li and Lege, 1998). Deformation producing surface markings is recognized as a succession of localized necks propagating along the gauge length. In order for this to occur, an absolute non-deforming plane must exist in the material. Under strain ratios where β is positive, no such plane exists that can be observed from the face of the specimen (Li and Lege, 1998).

Another important feature of PLC deformation is the commonly observed occurrence of an incubation strain, ε_c. After a finite amount of plastic strain, the

deformation behaviour changes from a homogenous to an inhomogeneous one, initiating the onset of serrated yielding. According to the results in Figure 4.11 to Figure 4.13 and Figure 4.16 to Figure 4.18, as the strain path of the specimen moves from simple tension towards balanced biaxial conditions, the development of PLC bands is suppressed (Table 4.6 and 4.8). Again, no PLC bands or surface markings were associated with the specimens strained in biaxial tension and therefore, so no incubation strain was measured. The band strain was also found to linearly increase with the global strain with the maximum band strain decreasing with the change in strain path from the LHS to RHS of FLD (Table 4.5 and 4.7).

The formation of PLC bands has been considered to represent geometric imperfections in the material which limits the formability according to the M-K analysis (Kang et al., 2005). According the M-K analysis, the material in the imperfection does not deform in the same manner as the material outside of it. If we relate this to the findings in the current study, the strain path of the material in the in the PLC band will increase at a higher rate with respect to the material outside. As a result, the material in the imperfection experiences a loss of work-hardening capacity (Kang et al., 2005). Graphically, this can be represented on major and minor strain plot where the material in the imperfection deviates from proportional straining. An example of this is shown in Figure 5.6 for specimen geometries on the LHS of the FLD. In addition, the earlier onset of PLC banding (i.e. lower ε_c) results in the material in the imperfection to deviate sooner from the proportional strain path and approaches a plane strain condition sooner. Thus, theoretically a PLC forming material will exhibit lower forming strains.

According to Kang et al. (2005) a strong correlation was also found between the band strain and the thickness variation associated with the surface markings as a result of serrated yielding. As the maximum band strain increased, the variation in thickness also increased, representing a greater imperfection in the material. Further, no PLC bands were observed on the surface of the specimen under biaxial tension. Therefore, it is possible that as the strain path of the materials are shifted from the LHS to the RHS of the FLD, the extent of the PLC bands to act as geometric imperfections to initiate premature failure is decreased. Graphically this means that the 0.5 inch width specimens will show the earliest deviation, which progressively decreases as the strain paths shifts to the RHS of the FLD.

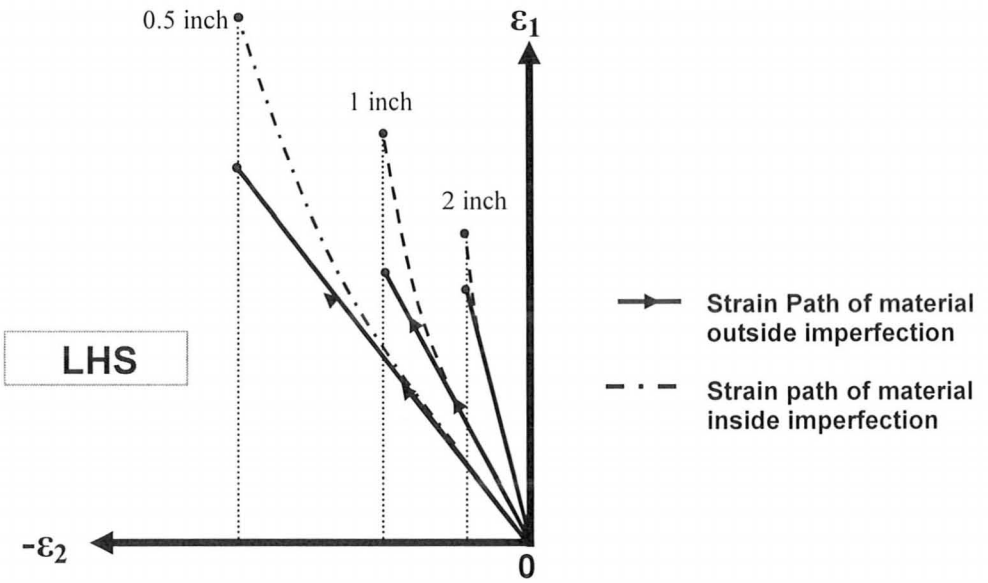

Figure 5.6: Gradual change in strain path within the imperfection with increasing strain for 0.5 inch, 1 inch and 2 inch geometries.

5.3.2 Failure Mechanisms

The failure behaviour of the specimens was investigated from the DIC strain map sequences. It was concluded that strain localization was initiated by the intersection of

two conjugate shear bands for the 0.5 inch, 1 inch and 2 inch specimen geometries. This mechanism was encountered in both materials, for all specimen samples tested. A series of strain maps demonstrating the progression leading to strain localization can be seen in Figure 5.6 for 1 inch and 2 inch width specimen geometries. At some point during the deformation, a pair of conjugate shear bands emerges. The strain at the intersection point of the shear bands is much higher than that found in the surrounding material and approaches a value close to the materials forming limit, which eventual becomes the site of strain localization. Failure then quickly spreads along one of the defining bands.

The failure behaviour of the 4 inch, 5 inch and 7 inch width specimens did not fail by the same mechanism as seen with the other specimen geometries. The 7 inch width specimens showed homogenous plastic flow and therefore, no deformation bands were seen prior to failure. For the 4 inch and 5 inch width specimens, the deformation bands were nucleated near the centre of the specimen and propagated outwards in a discontinuous but correlated motion, spanning the width of the specimen. In addition, no symmetrical deformation bands were observed during testing.

According to the DIC strain map sequences and strain plots across the specimens just prior to the final stages to failure, multiple shear bands can be seen in which strain begins to localize. The actual site of strain localization then develops along one of the dominant shear bands. An example of the process is shown in Figure 5.8. For this situation then, the actual mechanism of failure would then be strongly influenced by local variations in the microstructure such as inhomogeneities which cause strain concentrations.

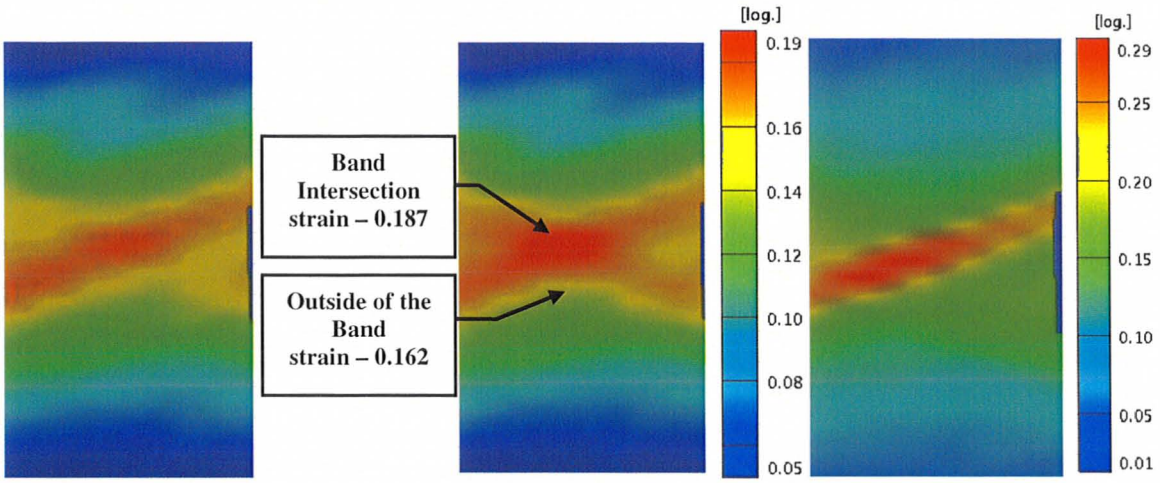

(a) 1 inch with specimen

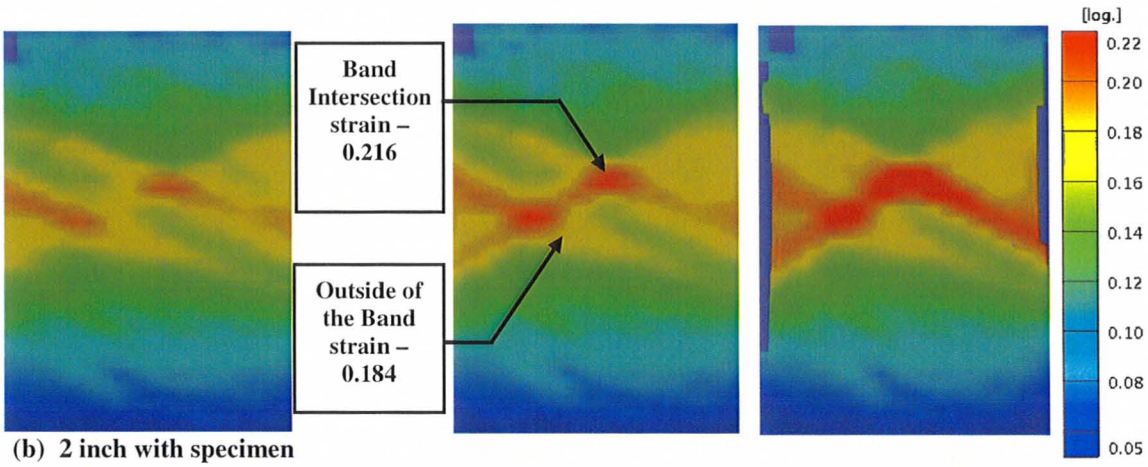

(b) 2 inch with specimen

Figure 5.7: Strain map sequences showing symmetrical band formation

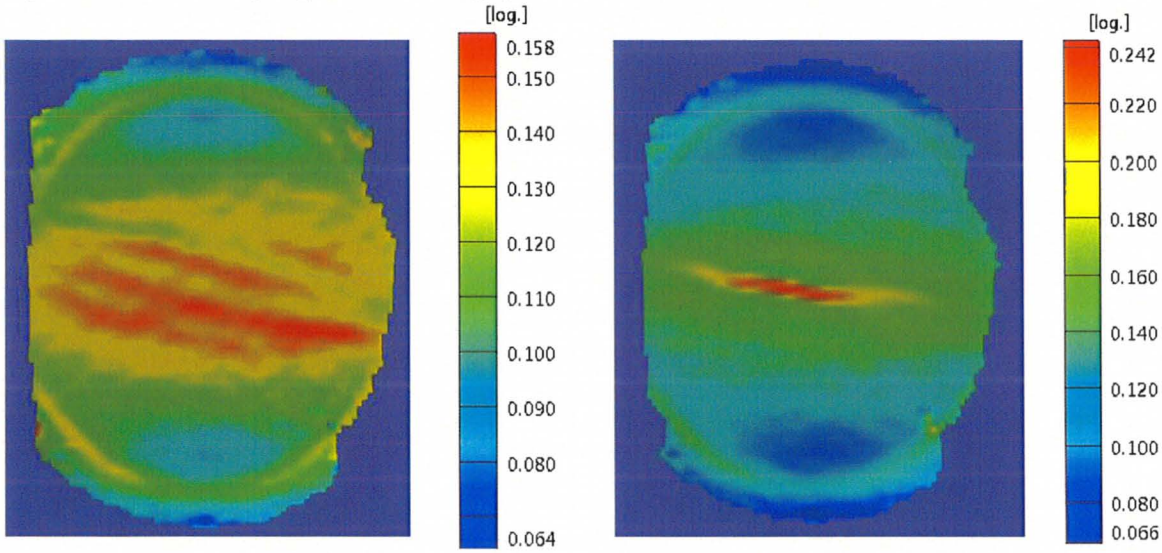

(a) Strain map just prior to failure

(b) Strain map of failed specimen

Figure 5.8: Strain map sequence for 4 inch width specimen showing deformation bands and failure.

5.4 Post-Necking and Fracture Behaviour

After strain localization occurs, plastic flow is still highly unstable as a result of a reduced work-hardening rate and a negative strain-rate sensitivity, both of which promote strain softening. When plastic deformation localizes, one or two consequential situations can be expected: that the plastic incompatibilities between the deforming and non-deforming zones is responsible for introducing stress concentrations which initiates bands of intense shearing or that the intense plastic deformation locally leads to accelerated damage accumulation around particles in terms of the nucleation, growth and coalescence of voids (Pardeon and Brechet, 2004). For the case of AA5754, unstable deformation gives way to the localization of plastic flow into bands of intense shearing, which accelerates ductile fracture.

In considering the results of the post-necking and fracture behaviour, shown in Chapter 4 (Section 4.4), little variation is seen between CC5754 and DC5754, despite the variation in fracture mechanism observed between the different strain paths. Both materials were considerably ductile as revealed by the high fracture strains. These results do not compare well with the findings from Kang et al. (2006) who studied the tensile fracture behaviour of CC5754. According to the study, the material showed a very limited amount of ductility, as seen in fracture profile in Figure 5.9 If a thickness reduction measurements is taken across the fractured profile in Figure 5.9, the value of t_m is more than double than that reported from tensile testing of CC5754 in the current study (t_m = 0.298 according to Figure 4.3), which results in a much lower fracture strain.

These findings are highly unusual considering the material is of the same composition and iron content (0.21 wt %). The discrepancies in the results are quite large and could be attributed to the techniques used in the determination of the fracture strains by Kang et al. (2006) and this work, as well as the validity of the certain assumptions of the theory of plasticity such as constancy of volume in voided solid. In addition, the material used in each study did not come from the same batch of CC5754 and DC5754. Therefore, a variation in the processes methods of the materials could have altered the nature and distribution of the second-phase particles, thus affecting the post-deformation behaviour.

Figure 5.9: Void-sheeting fracture profile for CC5754 0.21wt%Fe material tested in uniaxial tension (Kang et al., 2006).

The main factor which was thought to limit post-necking strain of CC5754 is the variation in the nature and spatial distribution of the second-phase particles in the microstructure. According to Kang et al. (2006) the strain to produce damage at stringers is lower than that for isolate particles. Therefore, when shear bands are formed in CC5754, they produce damage which accelerates to final fracture, thus limiting the post-deformation strain.

For the DC material though, the initiation of shear banding does not cause damage at isolate particles and therefore, necking occurs by continuous shear band formation, resulting in a greater amount of post-deformation strain (Kang, 2006), as shown in Figure 5.10. The DC5754 fracture profile reveals a pair of intense conjugate shear bands inside the localized neck region from which a central void forms. This is consistent with the results found in the current study in regards to the post-deformation behaviour of the DC material. These findings suggest that more data is needed to make a definite conclusion on the post-deformation and fracture behaviour of CC5754, in regards to DC5754.

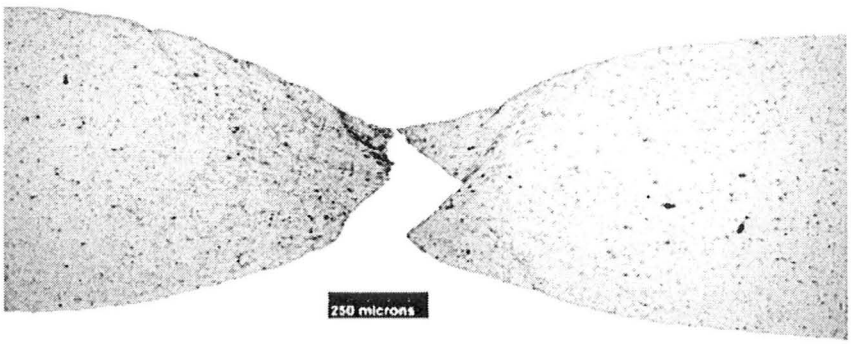

Figure 5.10: Double-cup fracture profile for DC5754 0.21wt%Fe material tested in uniaxial tension (Kang et al., 2006).

5.5 Evaluation of Test Technique

5.5.1 Digital Image Correlation Technique

The in-plane test methodology developed by Marciniak (1973) was chosen for formability evaluation in the current work. This method was combined with the digital image correlation (DIC) technique which provided in-situ strain measurements and a complete deformation history during the testing process. The success of the test

technique was due to the simplicity at which the data could be captured by the camera system. During in-plane deformation, the surface of the specimen remains level at all times to the camera system. This allows a complete view of the specimen's surface at all times, making data analysis by the system much simpler. The use of the DIC technique for out-of-plane testing entails more stringent optical requirements including specialized lenses to accommodate a large depth of focus and measuring volume due to the greater punch depths that are achieved (Figure 5.11). Therefore, the relative ease at which data can be obtained from in-plane testing makes the testing technique superior to that of out-of-plane testing.

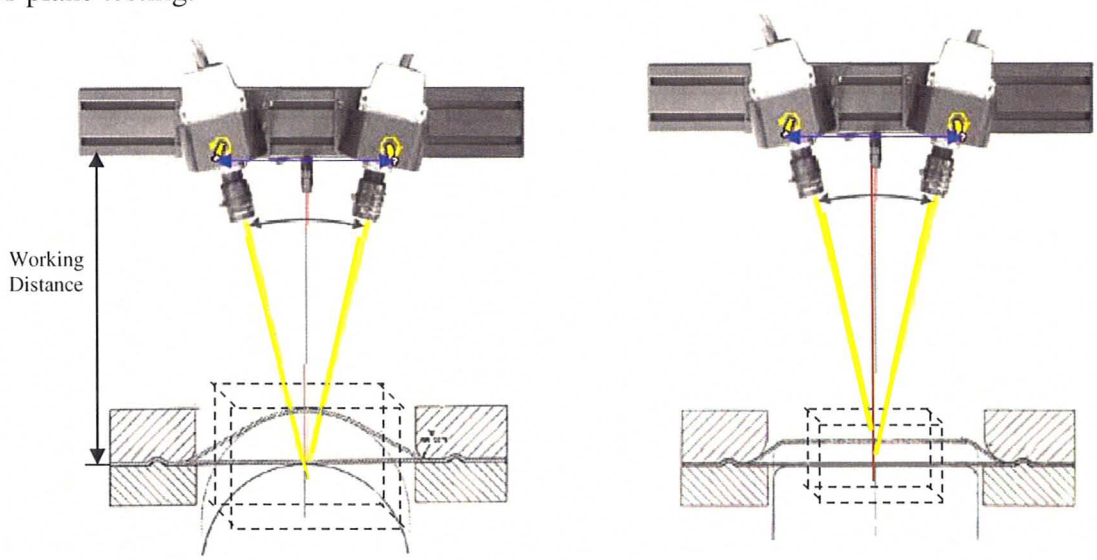

(a) Out-of-plane testing using hemispherical punch **(b) In-plane testing using Marciniak punch**

Figure 5.11: ARAMIS system set-up showing variation in measuring volume needed to accommodate deformation process.

5.5.2 Design and Optimization of Specimen and Driver Geometries

The design of specimen geometry proved to be an important factor, most specifically on the LHS of the FLD, when it came to determining the forming limits by

the graphical interpolation method presented by Bragard et al. (1972). The tapered specimen geometry (Figure 5.12 (b)) made analysis difficult due to the variation in strain distribution across the gauge length. The strain profile corresponding to the specimen geometry in Figure 5.12 (b) can be seen in Figure 5.13 (b) for a failed specimen. At the centre of the specimen where the cross-section is the smallest, the largest strains were found which also corresponds to the site of strain localization and fracture. The strain values just prior to localization are used to determine the forming limits and a polynomial of the 4th order was used to fit the data. Due to the steep profile of the curve at the peek, the data fitting process was not always able to fit the curve accurately. Examples can be seen in Appendix A. The use of a set width along the gauge length, Figure 5.12(a), would have made analysis much simpler and more accurate since the strain distribution outside of the localized neck would be more uniform across the gauge length (Figure 5.13 (a)).

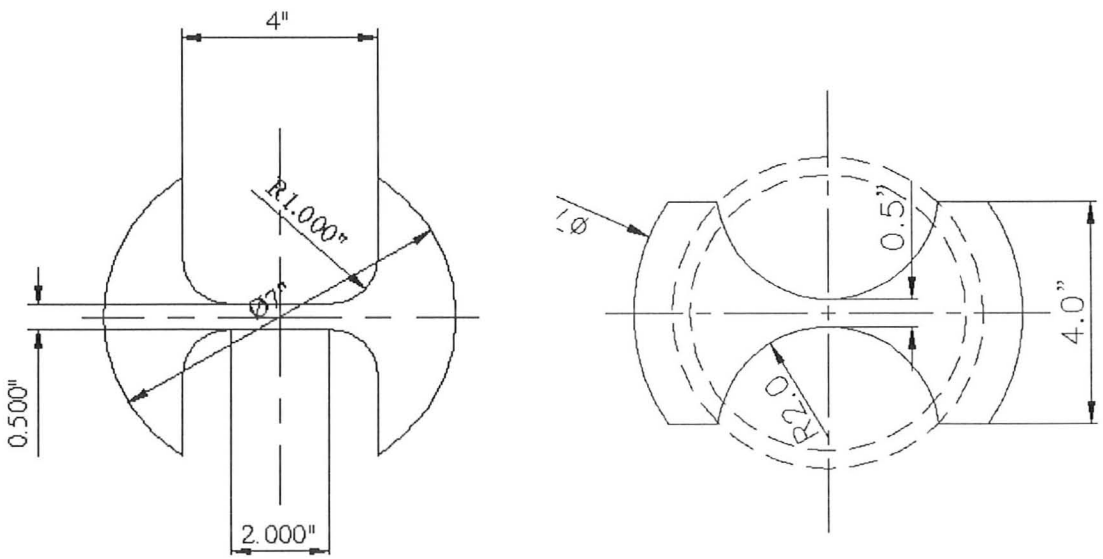

(a) Standard specimen geometry **(b) Tapered specimen geometry**

Figure 5.12: Comparison of specimen geometries for left-hand side of FLD. Drawings produced by Situ Quan and Mike Bruhis, 2004.

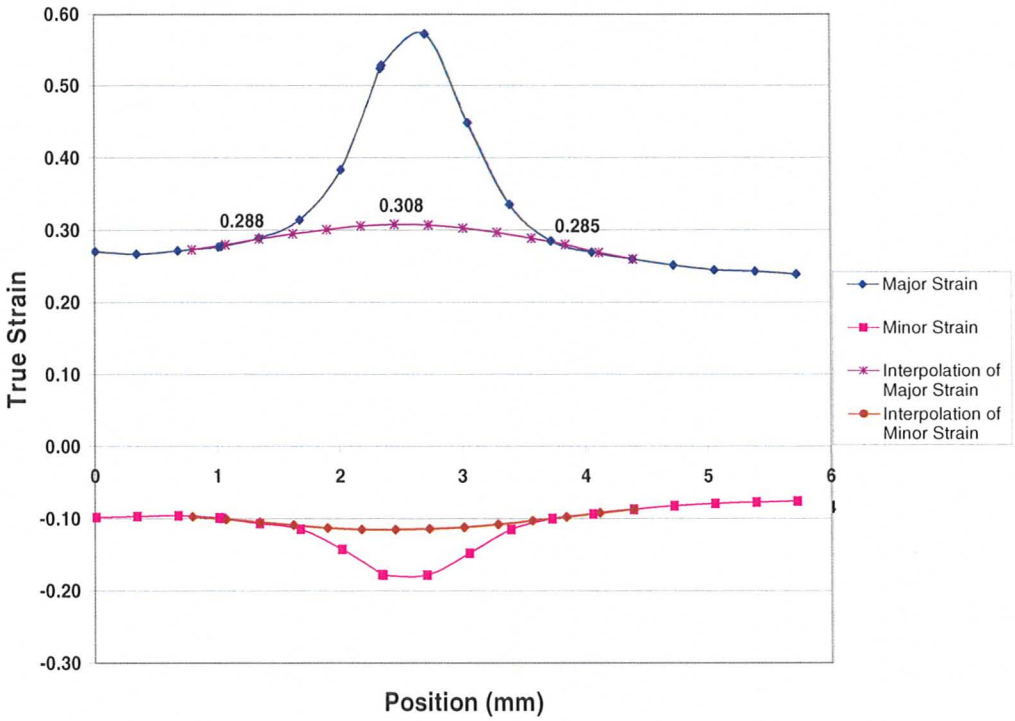

(a) Strain plot of section across standard 0.5 inch width specimen geometry shown in Figure 5.5(a).

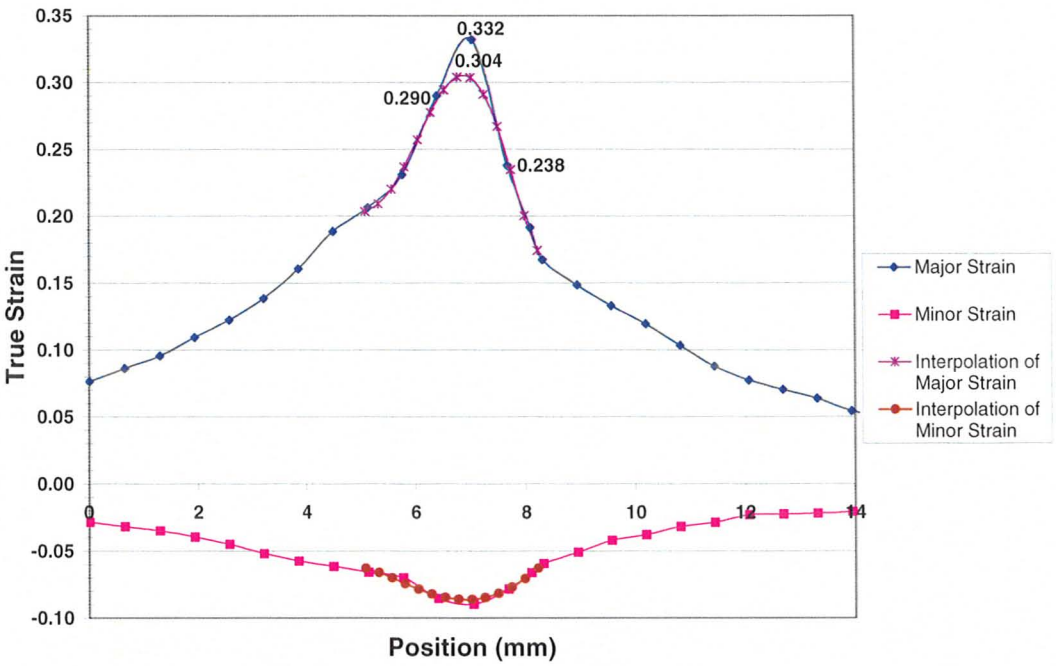

(b) Strain plot of section across tapered 0.5 inch width specimen geometry shown in Figure 5.5(b).

Figure 5.13: True major and minor strain plot showing 4th order polynomial interpolation.

The success of the Marciniak in-plane test method, for specimen geometries on the right-hand side of the FLD, relies on three critical parameters: (1) the driver blank material, (2) the friction conditions around punch profile and (3) the diameter of the driver hole. All these factors were determined experimentally by trial-and-error to obtain optimal testing conditions for formability analysis. The first parameter, the driver blank material, was determined with relative ease. Limited testing was needed to confirm the work performed by various authors who had succeeded at determined forming limits through the Marciniak test method (Raghavan, 1994; Moshkar et al., 2003).

However, determination of the friction conditions around the punch profile and the driver blank material required significant effort and time. During the trial-and-error testing period it was uncertain as to whether the failure of the test specimens and drivers was due to improper hole diameters in the driver material or to high friction conditions around the punch profile. Specimens with a variety of hole diameters in the driver were tested before it was determined that a punch with a larger draw radius was needed.

Once the radius of the punch profile was increased, fracture was achieved in the flat stretching region of the specimen by the proper deformation of the driver blank. The last critical parameter, optimization of the driver hole diameters, was then determined. Again, this task required a significant amount of time and effort due to inconsistencies in the performance of the drivers. Upon testing, it was not clearly seen which hole diameter performed best without doing a full detailed analysis of the test specimen with the ARAMIS system. In addition, specimens of the same geometrical width and hole diameter showed considerable scatter in the limit strain data. Variability in the

performance could have been due to the machining of the driver blanks. Despite the holes in the driver blank being filed so that no burred edges existed, sites of strain concentration still could have existed. Therefore, to determine the geometry of the driver blanks and hole diameters with a large degree of confidence, a greater number of test specimens needed to be examined. An FE test simulation utilizing a range of test conditions (driver blank material, thickness, friction etc) should be used in the future to optimize the test conditions for different strain paths.

Chapter 6
Conclusion

The objective of this study was to evaluate and compare the formability and fracture behaviour of AA5754 automotive sheet material in the O-temper, produced via two different processing routes, direct-chill (or DC) casting and continuous casting (CC), by the use of the forming limit diagram (FLD).

The in-plane test methodology developed by Marciniak (1973) was chosen for formability evaluation for its sensitivity to material inhomogeneities in order to try to differentiate materials with similar characteristics. Optimization of the test conditions for in-plane formability testing resulted in achieving failure under a series of strain paths ranging from simple tension through plane strain to balanced biaxial tension. The in-plane test technique was successful at determining the intrinsic forming limits of the two materials which compared well with results from previous studies. The DC5754 material showed a slightly higher forming limit on the left-hand side of the FLD in comparison to the CC material. This was attributed to the variation in processing methods and composition of the alloys which has been shown to alter the material's mechanical properties, most specifically in terms of the achieved strength level, uniform strain and work-hardening characteristics. However, the majority of the strain paths generated were found on the left-hand side or near plane strain conditions of the FLD. The forming limits on the right-hand side were approximated by a straight line, thus making it difficult to make a complete interpretation of the results.

The in-plane test methodology was coupled together with digital image correlation (DIC) techniques to provide in-situ strain measurements and deformation analysis throughout the testing process. The DIC technique revealed macroscopic scale non-uniformities, in the form of PLC deformation bands, in the plastic flow behaviour of the materials at room temperature as a result of dynamic strain aging (DSA). This behaviour appeared to be dependent on the strain path, for the characteristics of the deformation bands were altered in respect to the type of bands that were observed and the strain at which they were formed. The PLC effect was also shown to appear in the form of surface band marking, which acted as geometric imperfections to initiate premature failure, thus leading to a reduction in ductility and limiting the potential application of the materials.

Finally, the post-necking and fracture behaviour of CC5754 and DC5754 showed little difference between the materials, despite the variation in fracture mechanism observed between the different strain paths. Both materials were considerably ductile as revealed by the high fracture strains, which contradicts previous studies on the fracture behaviour of CC5754. These finding suggests that either the present in-plane forming technique was unable to differentiate the materials in a conclusive manner or that the actual differences in the materials used in the current study were small.

References

Akeret R. Shear bands as a cause of plastic instability in sheet forming. Symposium on Plastic Instability, Paris, France (1985).

H.Azari. Review of DC and CC of Al alloys. Post Doctoral Fellow, McMaster University (2000) Private communication.

Bird JE, Carlson JM. Shear band formation during sheet forming. J. Metals (1986) 47-54.

Bird JE, Carlson JM. Geometric models of internal shape change as shear bands form during plane strain extension. Met. Trans. A **18A** (1987) 563-579.

Bird JE, Newman KE, Narasimhan K, Carlson JM. Heterogeneous initiation and growth of sample-scale shear bands during necking of Al-Mg sheet. Acta Metall. **v35** (1987) 2971-2982.

Bird JE, Carlson JM. Progressive failure of surface microstructure during sample-scale shearing flow. Acta Metall. **v36** (1987) 2307-2322.

Bragard A, Barnet JC, Bonnarens H. A simplified technique to determine the FLD at the onset of necking. Metall. Rep. CRM (1972).

Burger GB, Gupta AK, Jeffrey PW, Lloyd DJ. Microstructural control of aluminum sheet used in automotive applications. Mater. Charact. **v35** (1995) 23-39.

Casarotto L, Tutsch R, Ritter R, Dierke H, Klose F, Neuhauser H. Investigation of PLC bands with optical techniques. Comput. Mater. Sci. **v32** (2005) 316–322.

Charpentier PL. Influence of punch curvature on the stretching limits of steel sheet. Met. Trans. A **6A** (1975) 1665-1669.

Cheng XM, Morris JG. Texture, microstructure and formability of SC and DC cast Al-Mg alloys. Mat. Sci. Eng. **A323** (2002) 32-41.

Chihab K, Estrin Y, Kubin LP, Vergnol J. The kinetics of the Portevin-Le Chatelier bands in an Al-5at%Mg Alloy. Scripta Metal. **v21** (1987) 203-208.

Cieslar M, Fressengeas C, Karimi A, Martin JL. Portevin-Le Chatelier effect in biaxially strained Al-Fe-Si foils. Scripta Mater. **v48** (2003) 1105-1110.

Considère AG. Memoire sur l'emploi du fer et de l'acier dans les constructions. Annales des Ponts et Chausses (ser.6) 9 (1885) 574-775.

Cottrell AH. A note on the Portevin-Le Chatelier effect. Phil. Mag. **v44**(1953) 829-832.

Dover IR, Embury JD. The influence of microstructural features on the formability of aluminum alloys. Mater. Sci. Forum, **v9** (1986) 188-201.

Duan X, Jain M, Metzger D, Kang J, Wilkinson DS, Embury JD. Prediction of shear localization during large deformation of a continuous cast Al-Mg sheet. Mater. Sci. Eng. A **v394** (2005) 192-203.

W.T. Ennor, U.S. patent 2,301,027 (1942).

French IE, Weinrich PF. The shear mode of ductile fracture in materials with few inclusions. Met. Trans. A **7A** (1976) 1841-1845.

Ghosh AK, Hecker SS. Stretching limits in sheet metals: In-plane versus out-of-plane deformation. Met. Trans. **v5** (1974) 2161-2164.

Ghosh AK. The Influence of Strain Hardening and Strain Rate Sensitivity on Sheet Metal Forming. J. of Engineering Materials and Technology (Trans. ASME) **v99** (1977) 264-274.

J.Gimple. Effect of superimposed pressure on damage evolution and fracture behaviour of automotive aluminum alloys (2001) Masters thesis, McMaster University, Ontario, Canada.

S.Girard. Effect of thermomechanical processing on texture development in a twin-belt cast automotive aluminum alloy (2002) Master thesis, McMaster University, Ontario, Canada.

GOM mbH. ARAMIS v5.4.0 manual, Braunschweig, Germany (2005).

GOM mbH. ARGUS v4.7 manual, Braunschweig, Germany (2001).

Goodwin GM. Application of strain analysis to sheet metal forming in the press shop. SAE Technology Paper No.680093 (1968).

H. Halim. The Portevin-Le Chatelier effect and shear band formation in AA 5754 aluminum alloy (2006) Master thesis, McMaster University, Ontario, Canada.

Hamilton CH, Ghosh AK. ASM Handbook, Forming and Forging, **v14** (1988) 791-804.

Hecker SS. Simple techniques for determining forming limit curves. Sheet Met. Ind. **v52** (1975) 671-676.

Hill R. On discontinuous plastic states with special reference to localized necking in thin sheets. J. Mech. Phys. Solids, **v1** (1952) 19-30.

Hollomon JH. Tnsile Deformations. AIME Trans. **v162** (1945) 268-290.

Hosford WF, Caddell RM. Metal Forming: Mechanics and Metallurgy. New Jersey: Prentice-Hall, 1993.

Jain M, Allin J. An analysis of experimental variability of forming limit diagrams. Proceeding of the 39th SAMPE symposium (1994) 2564-2570.

M. Jain, D.S. Wilkinson and J.D. Embury. Modelling of Microstructure and Phenomenological Aspects of Formability of Automotive Aluminum Sheet Materials – A Review of Literature, McMaster University (2001) Private communication.

Janecek M, Slamova M, Hajek M. Structural transformations in continuously cast Al-Mg alloys. J. Alloys Compd. **v378** (2004) 316-321.

Kang J. Formability of strip cast automotive AA5754 sheet. Post Doctoral Fellow, McMaster University (2002) Private communication.

Kang J. Post Doctoral Fellow, McMaster University (2004) Private communication.

Kang J, Wilkinson DS, Embury JD, Jain M. Effect of type-B Portevin-Le Chatelier bands on the onset of necking in uniaxial tension of strip cast AA5754 sheets. Scripta Metal. **v53** (2005) 499-503.

Kang J. Effect of processing route on the spatial distribution of constituent particles and their role in the fracture process of AA5754 alloy sheet material. Post Doctoral Fellow, McMaster University (2006) Private communication.

Keeler SP, Bachofen WA. Plastic instability and fracture in sheets stretched over rigid punches. Transaction ASM, **v56** (1963) 25-48.

Keeler SP. Determination of forming limits in automotive stampings. Sheet Met. Ind. (1965).

Kocks UF, Jonas JJ, Mecking H. The development of strain rate gradients. Acta Metall. **v27** (1979) 419-432.

Korbel A, Embury JD, Hatherly M, Martin P, Erbsloh HW. Microstructural aspects of strain localization in Al-Mg alloys. Acta Metall. **V34** (1986) 1999-2009.

Korbel A, Martin P. Microstructural events of macroscopic strain localization in prestrained tensile specimens. Acta Metall. **v36** (1988) 2575-2586.

Kubin LP, Estrin Y. Comment on the strain rate sensitivity during serrated yielding. Scr. Metall. **v23** (1989) 815-823.

Kubin LP, Estrin Y. Evolution of dislocation densities and the critical conditions for the Portevin-Le Chatelier effect. Acta Metall. **v38** (1990) 697-708.

Lang W. Nomarshi Differential Interference Contrast microscopy- fundamentals and experimental designs. Carl Zeiss, Oberkochen, Germany (1977).

Lebyodkin M, Brechet Y, Estrin, Y, Kubin L. Statistical behaviour and strain localization patterns in the Portevin-Le Chatelier effect. Acta Mater. **v44** (1996) 4531-4541.

Li M, Lege DJ. Serrated flow and surface markings in aluminum alloys. J. Eng. Mater. Tech. **v120** (1998) 48-55.

Lloyd DJ. The deformation of commercial aluminum-magnesium alloys. Met. Trans. A **v11A** (1980) 1287-1294.

Lloyd DJ. Strain localization and shear banding in aluminum alloys. TMS-AIME Processing, Formability and Metallurgical Structure. A.K Sachdev and J.D. Embury (eds.) Orlando, Fl,USA (1987) 193-209.

Lloyd DJ, Court SA. Influence of grain size on tensile properties of Al-Mg alloys. Mater. Sci. Technol. **v19** (2003) 1349-1354.

Marciniak Z, Kuczynski K. Limit strains in the processes of stretch-forming sheet metal. Int. J. Mech. Sci. **v9** (1967) 609-620.

Marciniak Z, Kuczynski K, Pokora T. Influence of the plastic properties of a material on the forming limit diagram for sheet metal in tension. Int. J. Mech. Sci. **v15** (1973) 789-805.

Marciniak Z, Duncan JL, Hu SJ. Mechanics of sheet metal forming. New Delhi: Elsevier, 2002.

Matlock DK, Krauss G. Microstructure and ductility of sheet steels. TMS-AIME Processing, Formability and Metallurgical Structure. A.K Sachdev and J.D. Embury (eds.) Orlando, Fl,USA (1987) 33-48.

McCormick PG. The Portevin-Le Chatelier effect in Al-Mg-Si alloys. Acta Metall. **v19** (1971) 463-471.

McCormick PG. Negative stain rate sensitivity and the development of localized yielding. TMS-AIME Processing, Formability and Metallurgical Structure. A.K Sachdev and J.D. Embury (eds.) Orlando, Fl, USA (1987) 227-243.

Miller WS, Zhuang L, Bottema J, Wittebrood AJ, De Smet P, Haszler A, Vieregge A. Recent development in aluminum alloys for the automotive industry. Mater. Sci. Eng. **A280** (2000) 37-49.

Morris JW, Ledezma M, Shaffer SJ. Research towards improved formability in low-carbon sheet steel. TMS-AIME Processing, Formability and Metallurgical Structure. A.K Sachdev and J.D. Embury (eds.) Orlando, Fl, USA (1987) 49-69.

Moshksar MM, Mansorzadeh S. Determination of the forming limit diagram for Al 3105 sheet. J. Mater. Process. Technol. **v141** (2003) 138-142.

Pardoen T, Brechet Y. Influence of microstructure-drive strain localization on the ductile fracture of metallic alloys. Phil. Mag. **v84** (2004) 269-297.

Park DY, Niewczas. Anisotropic deformation of AA5754 in a temperature range from 4.2 to 295K. PhD candidate, McMaster University (2006) Private communication.

Pilkey AK, Fowleg JB, Worswick MJ, Burger G. Characterizing particle distribution in model aluminum alloy systems. Microstructural Sci. **v10** (1995)329-336.

Pink E, Grinberg A. Serrated flow in a ferritic stainless steel. Mater. Sci. Eng. **v51** (1981)1-8.

Robinson JM. Serrated flow in aluminum based alloys. Int. Mater. Rev. **v39** (1994) 217-227.

Robinson JM, Shaw MP. Microstructural and mechanical influences on dynamic strain aging phenomena. Int. Mater. Rev. **v39** (1994) 113-121

Romhanji E, Popovic M, Glisic D, Milenkovic V. Formability of high-strength Al-Mg6.8 type alloy sheet. J. Mat.. Sci. **v33** (1998) 1037-1042.

A.J Rysk. Formability of hot-rolled HSLA steels (1986) Master thesis, McMaster University, Ontario, Canada.

Sarkar J, Kutty TRG, Conlon KT, Wilkinson DS, Embury JD, Lloyd DJ. Tensile and bending properties of AA5754 aluminum alloys. Mat. Sci. Eng. A316 (2001) 52-59.

Sing WM, Rao KP. Role of strain-hardening laws in the prediction of forming limit curves. J. Mater. Process. Technol. **V63** (1997) 105-110.

Slamova M, Karlik M, Robaut F, Slama P, Veron M. Differences in microstructures and texture of Al-Mg sheets by twin-roll continuous casting and by direct-chill casting. Mater. Charact. **v49** (2003) 231-240.

K.Spencer. Evolution of Fracture in an automotive aluminum alloy under plane strain tension (2000) Masters thesis, University of Waterloo, Ontario, Canada.

Spencer K. The influence of iron content on the plane strain fracture behaviour of AA5754 Al-Mg sheet alloys. Mat. Sci. Eng. **A325** (2002) 394-404.

Sutton MA, Wolter WJ, Peters WH, Ranson WF, McNeill SR. Determination of displacements using an improved digital correlation method. Image and Vision Computing, **v4** (1986) 143-150.

Tadros AK, Mellor PB. An experimental study of the in-plane stretching of sheet metal. Int. J. Mech. Sci. **v20** (1977) 121-134.

Timothy SP. A modified technique to measure formability in plane strain tension. Forming Limit Diagrams: Concepts, Methods and Applications. R.H Wagoner, K.S Chan, S.P Keeler (eds.) 1989: 21-36.

Voce E. The relationship between stress and strain for homogeneous deformation. J. Inst. Met. **v74** (1948) 537-562.

Webernig WM, Krol J, Pink E. Orientation dependence of serrated flow in polycrystalline thin sheet samples. Mater. Sci. Eng. **v80** (1986) 15-18.

Worthington PJ, Brindley BJ. Serrated yielding in substitutional alloys. Philos. Mag. **v19** (1969) 1175-1178.

Appendix A

Forming Limit Evaluation

The evaluation of the forming limits was completed following the methodology described in Chapter 3 (section 3.6), which involved using the graphical interpolation method presented by Bragard et al. (1972). The onset of localization was determined using the major and minor strain distributions as line profiles, obtained from ARAMIS systems. From the strain profiles, a polynomial of the 4th order was used to fit the data. The values prior to and after localization can be seen in the figures, along with the interpolated major strain value corresponding to the forming limit.

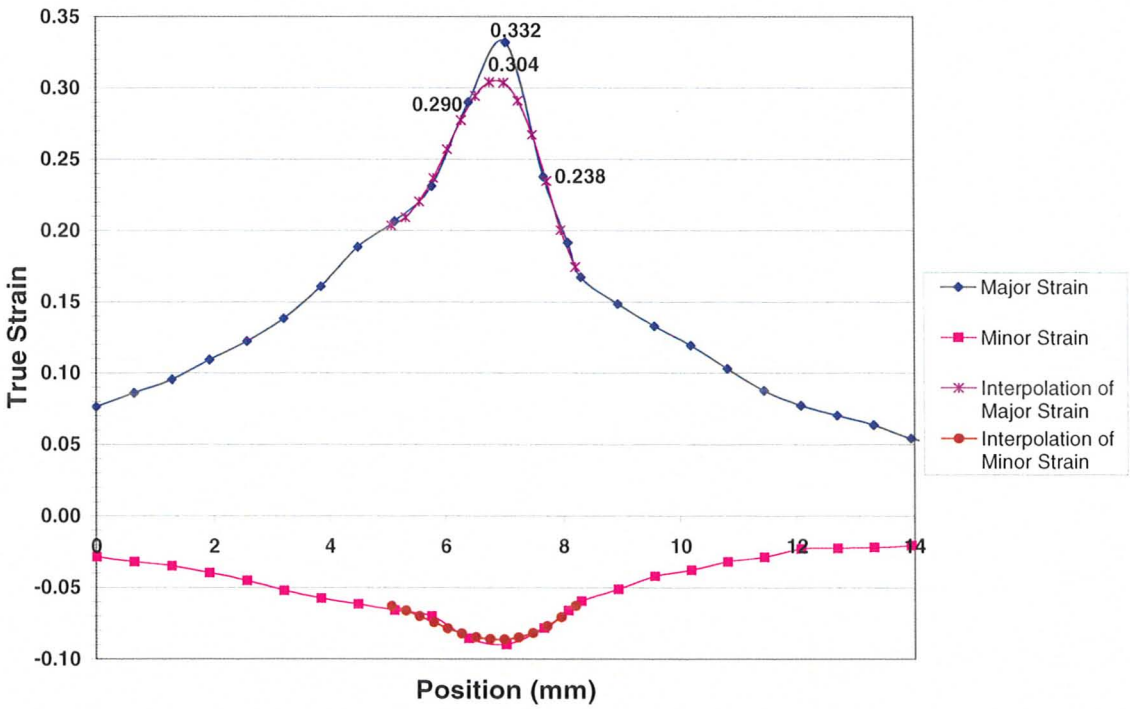

Figure A.1: True major and minor strain plot of section line showing 4th order polynomial interpolation for CC - 0.5 inch width specimen.

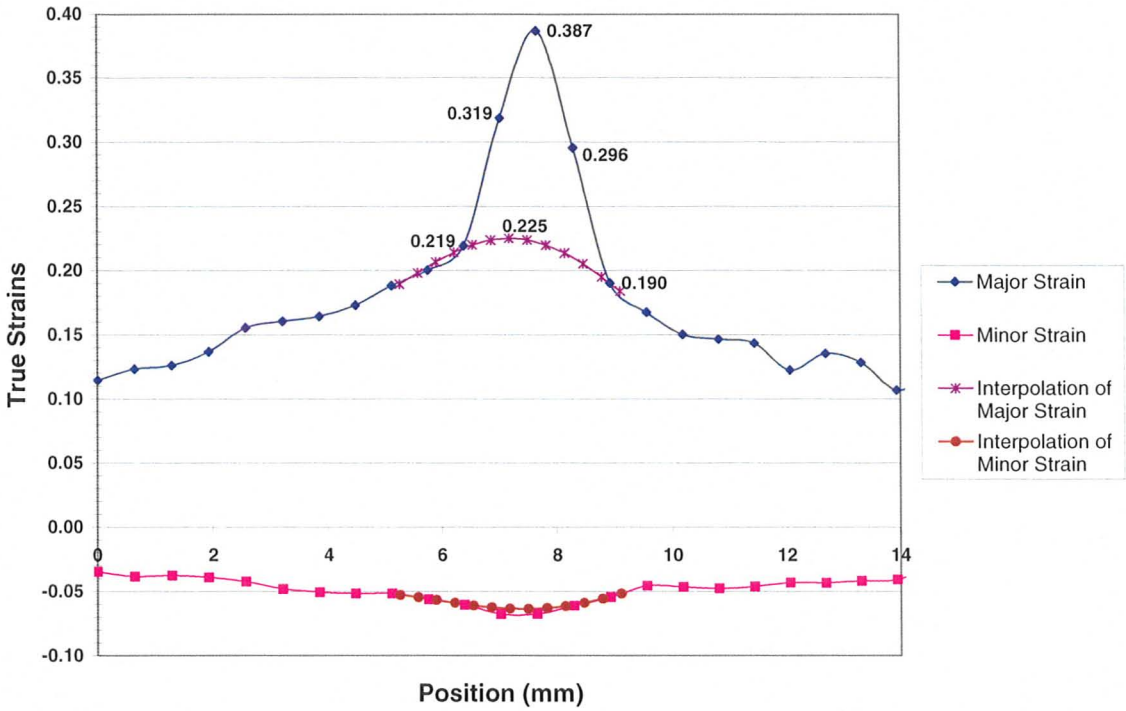

Figure A.2: True major and minor strain plot of section line showing 4th order polynomial interpolation for CC - 1 inch width specimen.

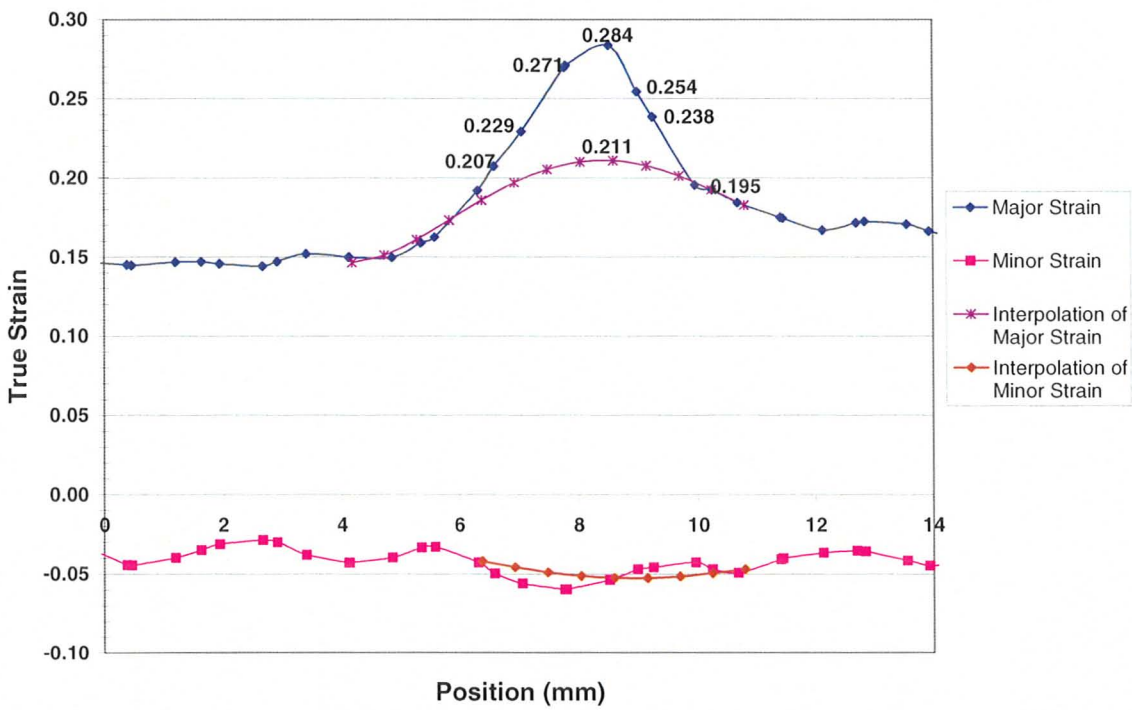

Figure A.3: True major and minor strain plot of section line showing 4th order polynomial interpolation for CC - 2 inch width specimen.

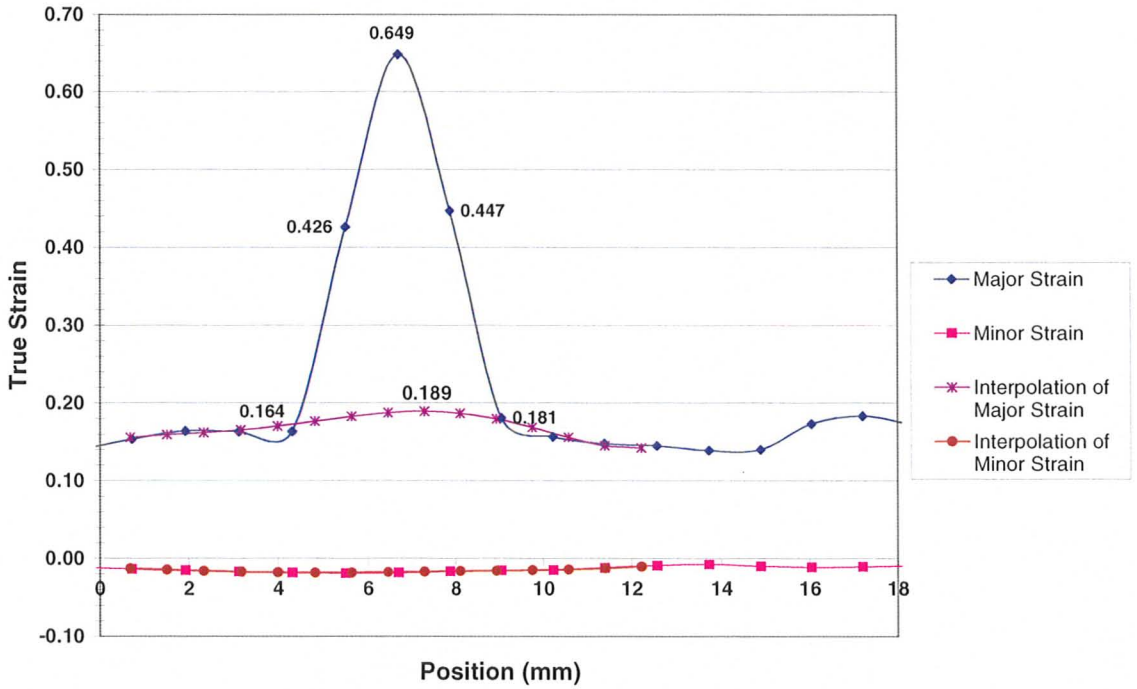

Figure A.4: True major and minor strain plot of section line showing 4th order polynomial interpolation for CC - 4 inch width specimen (1.4 inch diameter driver hole).

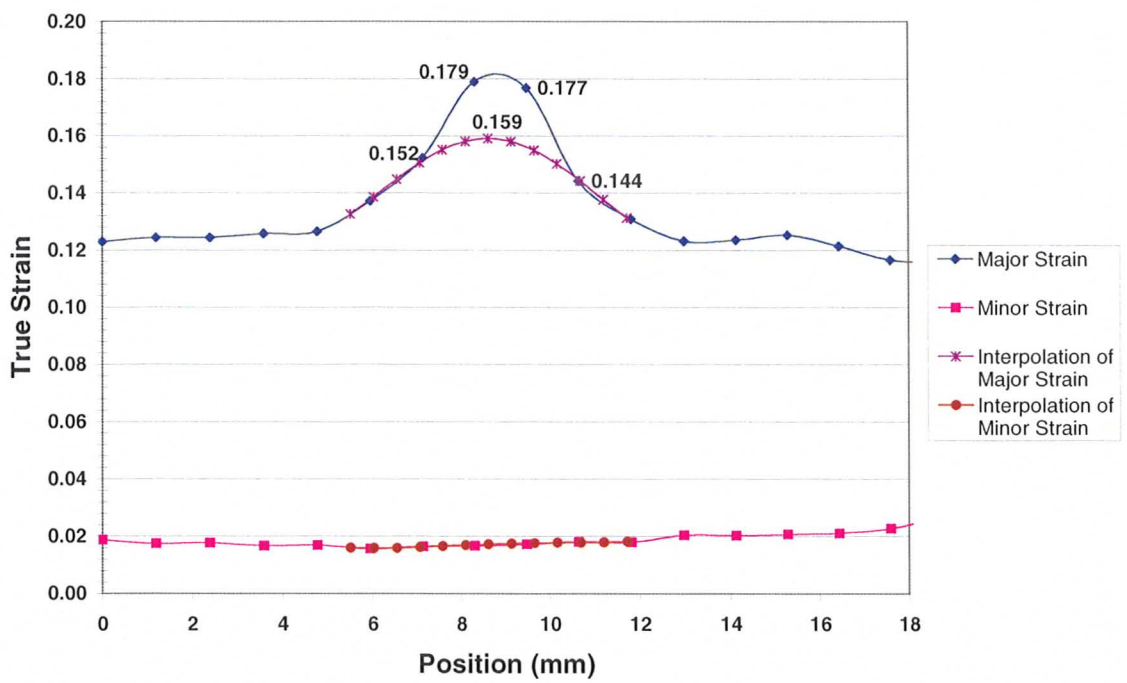

Figure A.5: True major and minor strain plot of section line showing 4th order polynomial interpolation for CC - 5 inch width specimen (1.4 inch diameter driver hole).

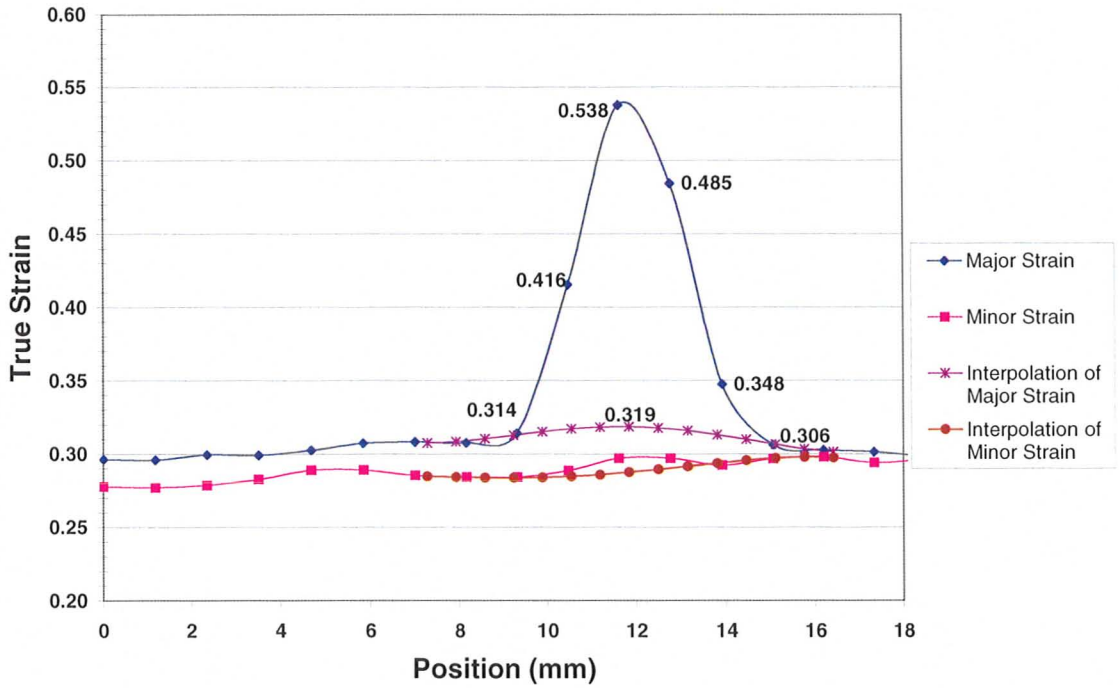

Figure A.6: True major and minor strain plot of section line showing 4th order polynomial interpolation for CC - 7 inch width specimen (1.2 inch diameter driver hole).

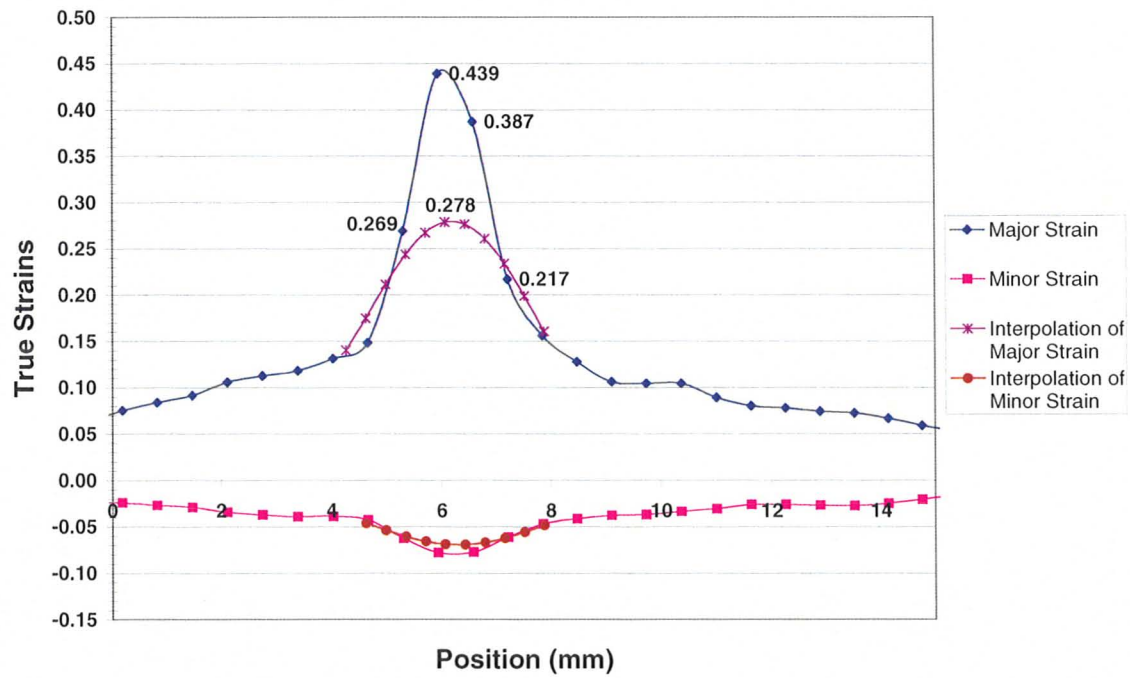

Figure A.7: True major and minor strain plot of section line showing 4th order polynomial interpolation for DC - 0.5 inch width specimen.

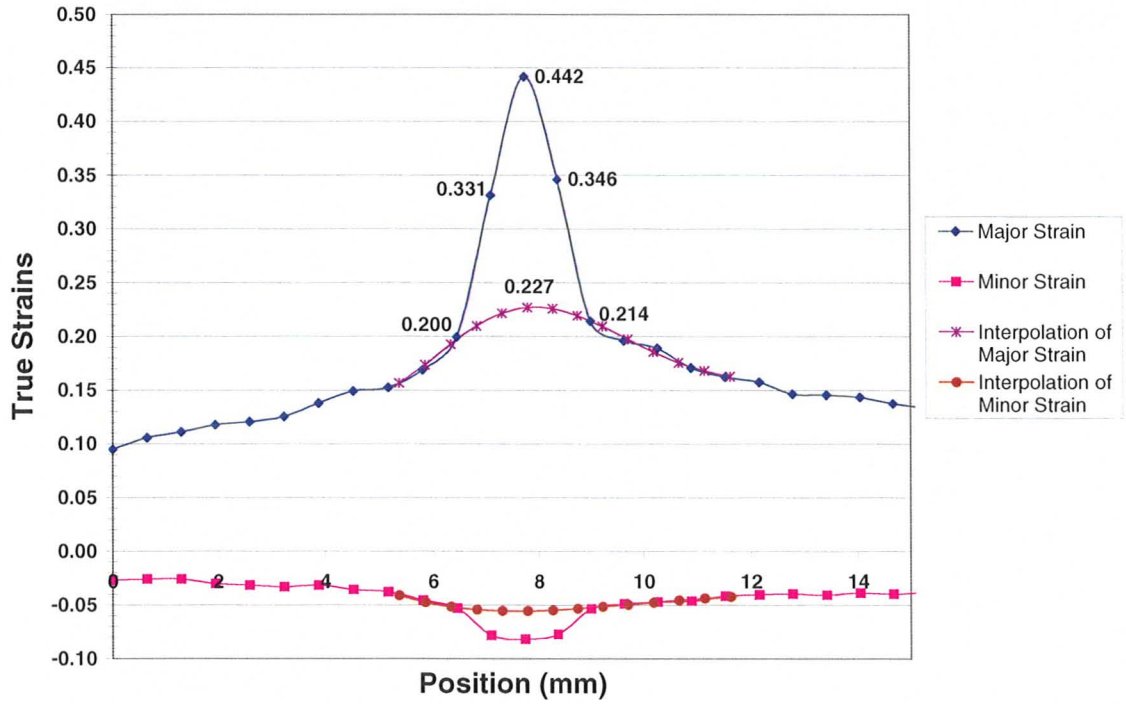

Figure A.8: True major and minor strain plot of section line showing 4th order polynomial interpolation for DC - 1 inch width specimen.

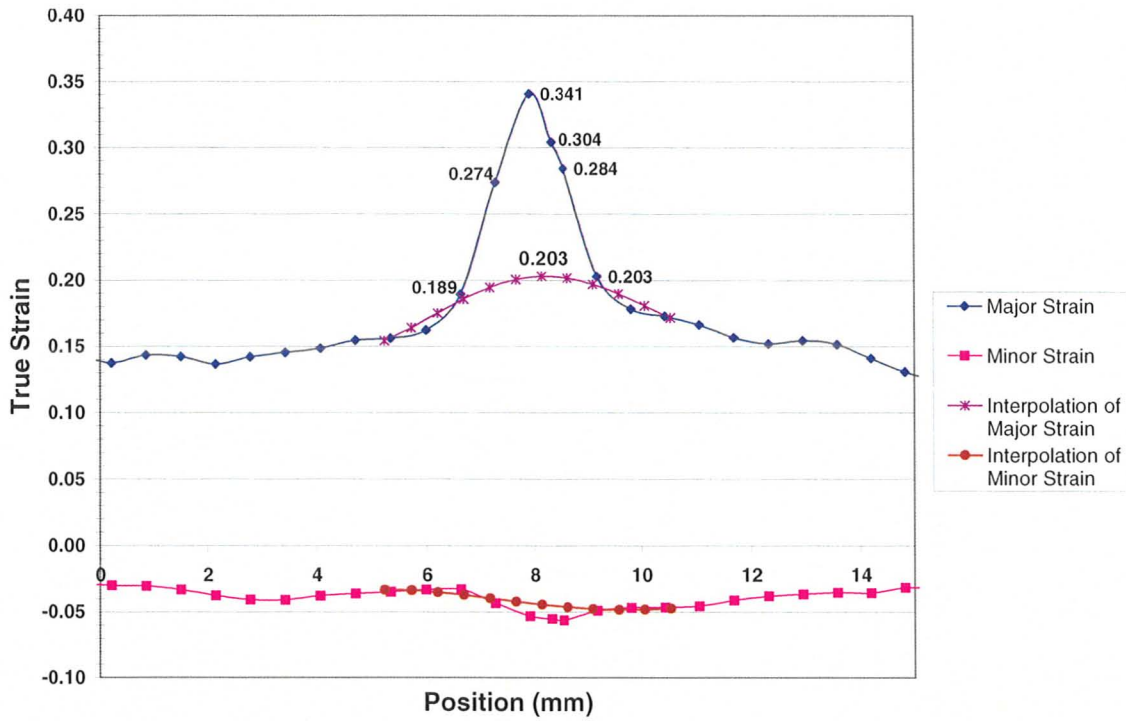

Figure A.9: True major and minor strain plot of section line showing 4th order polynomial interpolation for DC - 2 inch width specimen

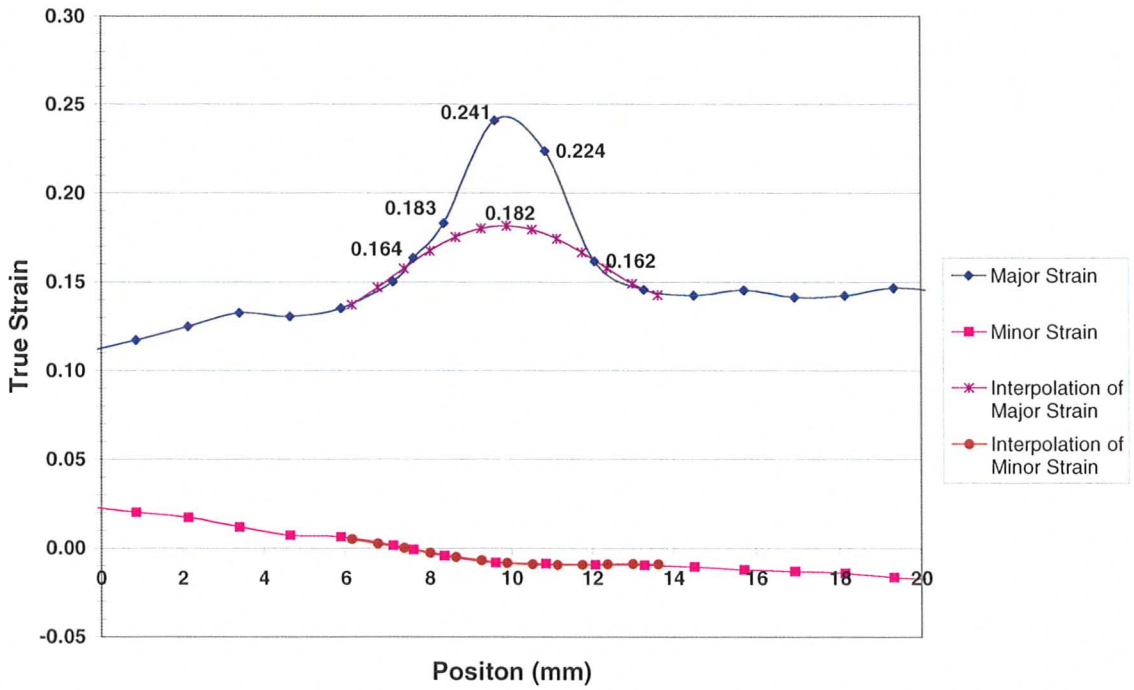

Figure A.10: True major and minor strain plot of section line showing 4th order polynomial interpolation for DC - 4 inch width specimen (1.5 inch diameter driver hole).

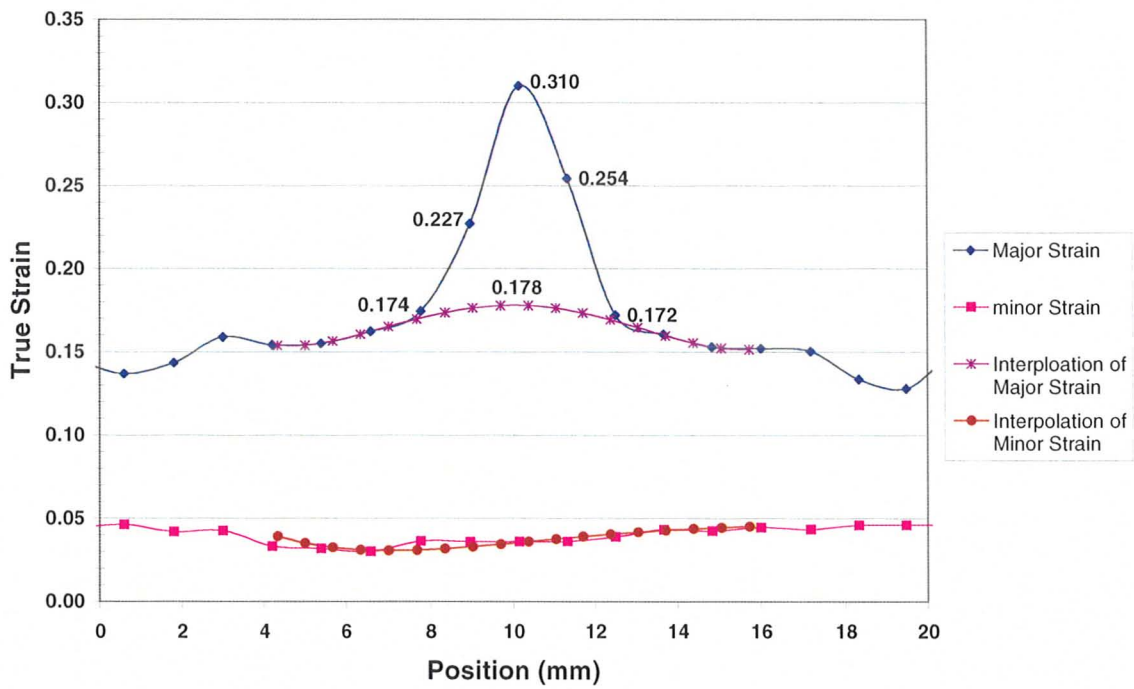

Figure A.11: True major and minor strain plot of section line showing 4th order polynomial interpolation for DC - 5 inch width specimen (1.4 inch diameter driver hole).

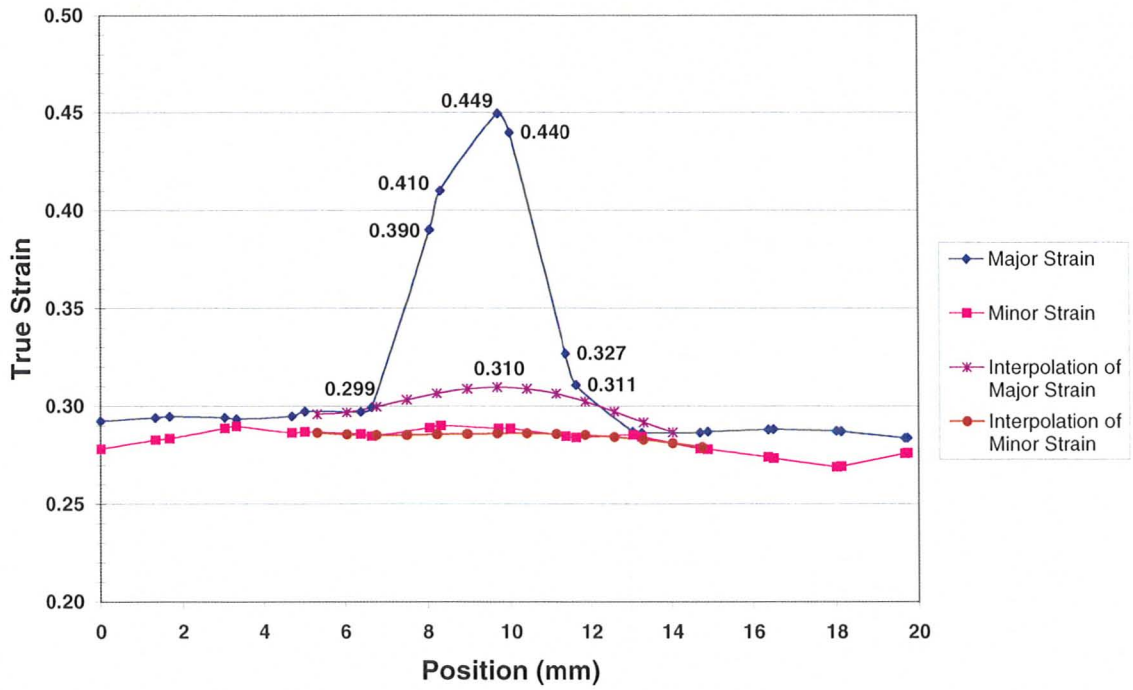

Figure A.12: True major and minor strain plot of section line showing 4th order polynomial interpolation for DC - 7 inch width specimen (1.3 inch diameter driver hole).

Appendix B

Surface Marking Observations

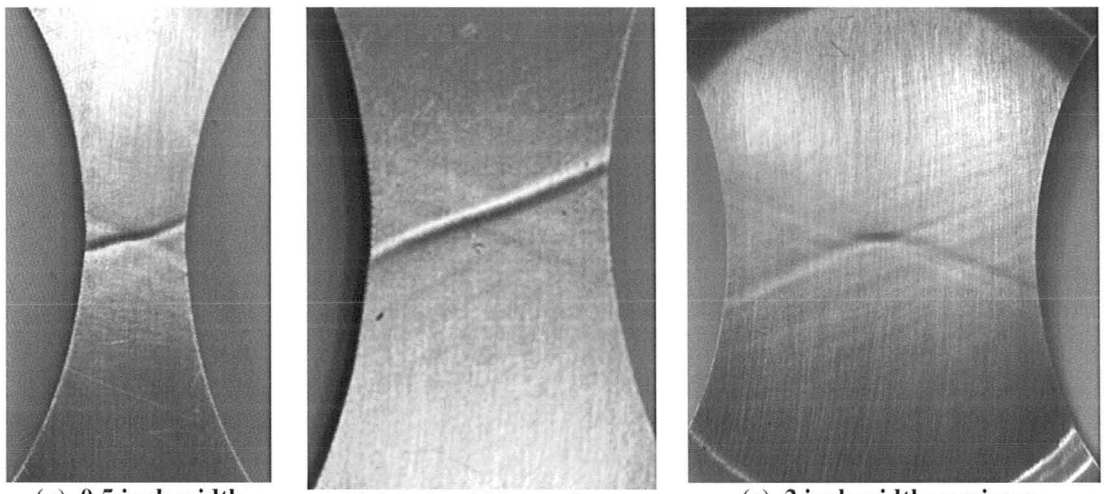

(a) 0.5 inch width specimen (b) 1 inch width specimen (c) 2 inch width specimen

Figure B.1: Strain localization in CC5754 specimens showing characteristic surface marking associated with the PLC effect. The bands are parallel and regularly spaced which classifies them as type B PLC bands.

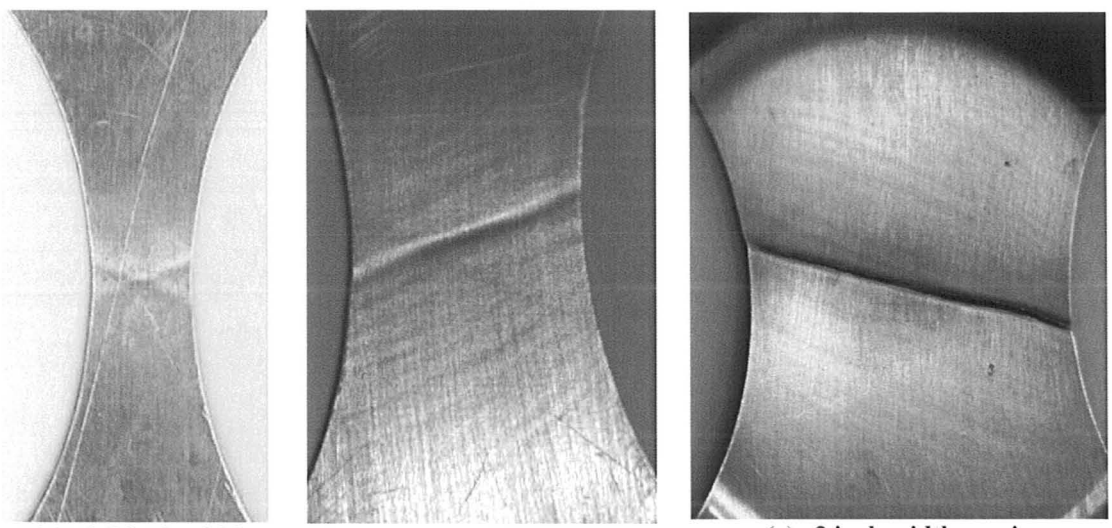

(a) 0.5 inch width specimen (b) 1 inch width specimen (c) 2 inch width specimen

Figure B. 2: Strain localization in DC5754 specimens showing characteristic surface marking associated with the PLC effect. The bands are parallel and regularly spaced which classifies them as type B PLC bands.

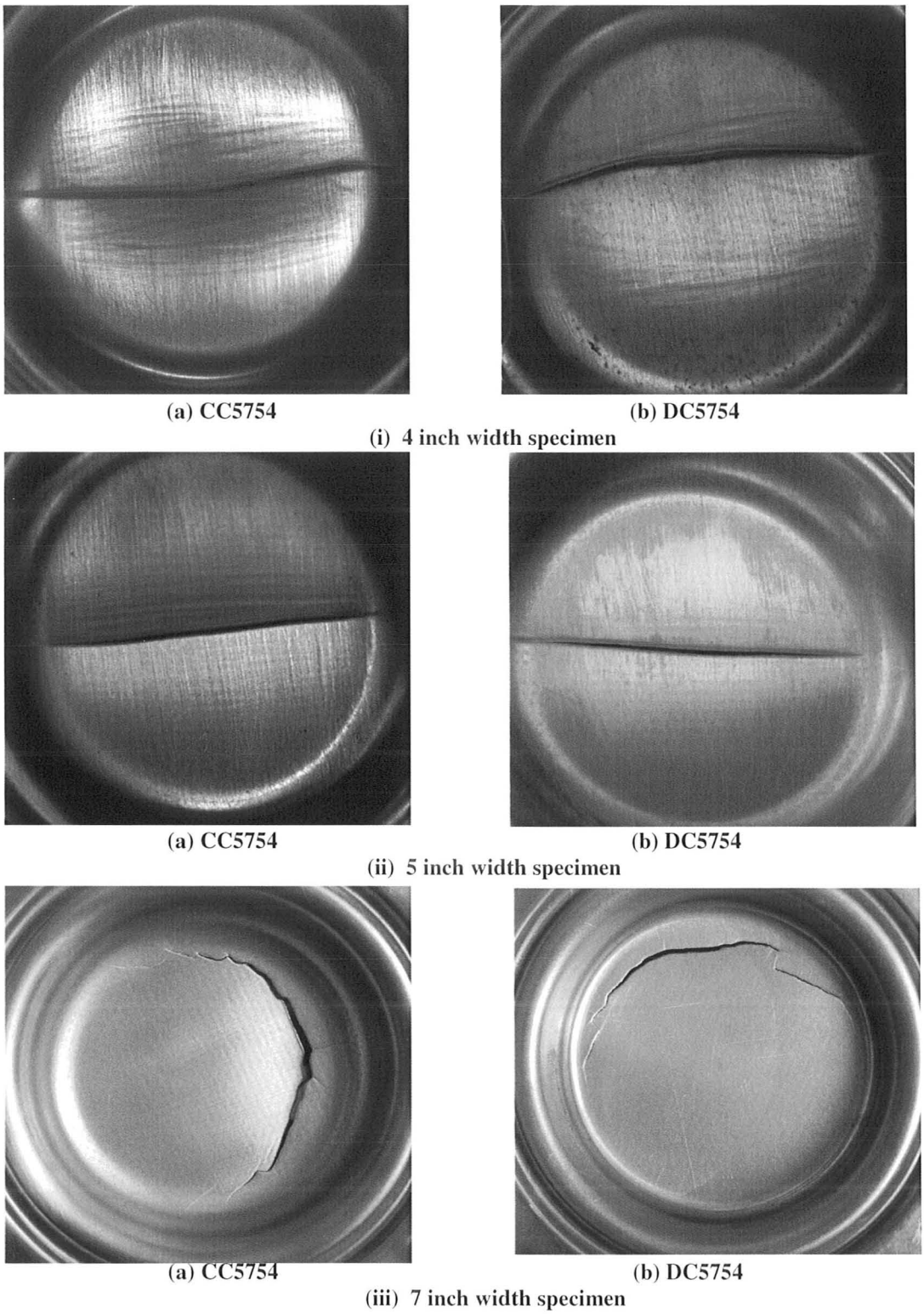

(a) CC5754 (b) DC5754

(i) 4 inch width specimen

(a) CC5754 (b) DC5754

(ii) 5 inch width specimen

(a) CC5754 (b) DC5754

(iii) 7 inch width specimen

Figure B.3: Characteristic surface marking associated with the PLC effect.